

**SUPERSONIC SEPARATORS:  
A GAS DEHYDRATION DEVICE**

**MOHAMMAD HAGHIGHI**





**SUPERSONIC SEPARATORS:  
A GAS DEHYDRATION DEVICE**

by

Mohammad Haghghi, B.Sc.

A thesis submitted to the  
School of Graduate Studies  
in partial fulfillment of the requirements  
for the degree of

**Master of Engineering**

**Faculty of Engineering and Applied Science**

**Memorial University of Newfoundland**

April 2010

St. John's

Newfoundland

## **ABSTRACT**

The ever growing demand for natural gas has led to the discovery and development of reservoirs in the most unreachable off-shore locations. Formation of hydrate is one of the most problematic issues involved in the production and transportation of natural gas. Gas dehydration is an effective and efficient method of preventing this difficulty. One of the main challenges in designing a dehydration unit for off-shore locations is its size. Supersonic separator is a device that combines the principles of Joule-Thompson expansion and cyclonic separation to efficiently remove the water content of natural gas produced from reservoir as a means of hydrate prevention. This device is small enough to suit the limitations of an off-shore location. This thesis is investigates the performance of supersonic separators in various operating conditions. A variety of design parameters are identified and analyzed through CFD techniques and a novel configuration is proposed for the supersonic separators. A lab test is set up for the validation of CFD results and extensive discussions are presented.

## **ACKNOWLEDGMENTS**

I sincerely thank my supervisor Dr. Majid Abedinzadegan Abdi for accepting me as a graduate student and for his guidance through all levels of my research. I also acknowledge the supervision of Dr. Shafiq Alam.

The financial support from the National Science and Engineering Research Council of Canada (NSERC) is also gratefully acknowledged. I wish to thank Dr. Stephen Butt, Associate Dean of Graduate Studies and Research, and Ms. Moya Crocker, Secretary to the Associate Dean of Graduate Studies and Research, for their superb administrative support.

The computational support from Atlantic Computational Excellence Network (ACEnet) and the technical expertise of MUN Engineering technical workshop is greatly appreciated.

I would also like to thank my wife, family and friends for their loving support.

# TABLE OF CONTENTS

<b>1. INTRODUCTION</b> .....	1
1.1. Objectives of Study .....	5
1.2. Scope of Study .....	5
1.3. Thesis Outline .....	6
<b>2. LITERATURE REVIEW</b> .....	7
<b>3. CFD AND THE GOVERNING EQUATIONS</b> .....	10
3.1. Governing Equations.....	10
<b>4. STUDY OF SUPERSONIC SEPARATORS</b> .....	14
4.1. Methodology .....	14
4.2. Pre-Processing.....	15
4.2.1. Geometry Creation.....	16
4.2.2. Mesh Generation.....	22
4.3. Processing.....	29
4.3.1. Geometry properties.....	30
4.3.2. Materials and their physical properties .....	31
4.3.3. Governing equations .....	31
4.3.4. Boundary conditions .....	32
4.4. Post-Processing .....	33
<b>5. RESULTS AND ANALYSIS</b> .....	34
5.1. Straight Nozzle with Swirling Flow.....	34
5.1.1. Meshing scheme.....	34

5.1.2.	Boundary Layer Thickness .....	35
5.1.3.	Sensitivity Analysis .....	40
5.2.	U-Shaped Nozzle.....	63
5.2.1.	Meshing Scheme.....	64
5.2.2.	Sensitivity Analysis .....	69
5.2.3.	Position of the Separation Channel.....	83
5.3.	Comparison of Straight and U-Shaped Nozzles.....	85
<b>6.</b>	<b>MODEL EVALUATION AND LABORATORY EXPERIMENTS.....</b>	<b>88</b>
6.1.	Test Set-Up.....	90
6.1.1.	Nozzle System .....	90
6.1.2.	Pressure Measurement .....	91
6.1.3.	Temperature Measurement .....	92
6.1.4.	Flow Measurement.....	92
6.1.5.	Air Supply.....	92
6.2.	Test Outline .....	98
6.3.	Results .....	99
<b>7.</b>	<b>CONCLUSIONS AND RECOMMENDATIONS .....</b>	<b>103</b>
	<b>REFERENCES.....</b>	<b>107</b>

## LIST OF FIGURES

Figure 4.1	Two dimensional geometry, used as an axis-symmetric body to simulate a typical nozzle.....	18
Figure 4.2	A typical three dimensional geometry used for CFD simulation in this research.....	18
Figure 4.3	A Typical three dimensional geometry: nozzle with extended U-shaped section.....	19
Figure 4.4	Profile for a variable radius curvature created in Microsoft Excel .....	21
Figure 4.5	A three dimensional geometry: nozzle with extended U-shaped section that follows a variable radius curvature profile.....	21
Figure 4.6	Typical triangular and rectangular face mesh elements used in CFD simulations. ....	23
Figure 4.7	Typical wedge-shaped volume mesh elements. ....	24
Figure 4.8	Tetrahedral volume mesh elements in the converging section of the nozzle followed by wedge elements in the throat.....	25
Figure 4.9	Boundary layer is modeled by ten rows of hexagonal elements that get thinner as they approach the wall.....	28
Figure 4.10	Boundary layers used near the wall and in the centre to account for wall boundary layer effects and high tangential velocity gradients near the axis of the nozzle. ....	29
Figure 5.1	Velocity magnitude profiles at the throat of the same nozzle configuration with 5 different scales. Horizontal axis represents a percentile radial position.....	38
Figure 5.2	Comparison of swirl velocity and axial velocity profiles used to compare corresponding boundary layer thicknesses.....	39
Figure 5.3	Axial velocity profile at the throat of a nozzle.....	39
Figure 5.4	Swirl velocity profile at the throat of a nozzle.....	40

Figure 5.5	Mass flow rate versus inlet pressure for an ideal gas. The flow is choked for all pressures. ....	44
Figure 5.6	The maximum axial velocity achieved in a typical nozzle with different inlet pressures. The outlet back pressure is 101kPa (1 atm) in all cases... 46	46
Figure 5.7	The position of the shockwave moves further away from the throat as the inlet pressure is increased.....	47
Figure 5.8	Axial velocity profiles along the axis of the nozzle for inlet pressures ranging from 135 kPa up to 345 kPa. Outlet back pressure is constant at 101 kPa (1 atm). ....	48
Figure 5.9	Mach number values along the axis of the nozzle. Inlet pressure varies between 135 kPa and 345 kPa and outlet back pressure is constant at 101 kPa (1 atm). ....	49
Figure 5.10	Area-weighted average tangential velocity (swirl intensity) plotted against axial position along the nozzle for various initial swirl velocity ratios ( $\zeta_0$ ). 54	54
Figure 5.11	Mass flow rate through the nozzle as a function of initial swirl velocity ratio. The nozzle is set to operate at a constant inlet pressure of 345 kPa. 55	55
Figure 5.12	The rate of change of mass flow rate with respect to swirl velocity ratio. 55	55
Figure 5.13	Variation of centrifugal acceleration along the nozzle. Area-weighted average values of centrifugal acceleration are plotted against axial position along the nozzle for various initial swirl velocity ratios ( $\zeta_0$ ). ....	56
Figure 5.14	Mass flow rate of the gas through the nozzle with respect to throat cross sectional area. The flow rate is linearly correlated to the throat area.....	58
Figure 5.15	Static pressure along the axis of a typical nozzle with the outlet back pressure ranging from 303 kPa (44 psia) down to 138 kPa (20 psia). The inlet pressure is 345 kPa (50 psia) at all times. ....	61
Figure 5.16	Mach number profiles along the axis of a typical nozzle with the outlet back pressure ranging from 303 kPa (44 psia) down to 138 kPa (20 psia). The inlet pressure is 345 kPa (50 psia) at all times. ....	62
Figure 5.17	The axial position of the shockwave against the outlet back pressure. Note that the inlet pressure is 345 kPa for all cases.....	63

Figure 5.18	Cross-sectional view of the proposed geometry. Three sections of the device are marked.....	66
Figure 5.19	The dimensions of the proposed geometry. ....	67
Figure 5.20	Six sections of the geometry used in the meshing scheme. ....	67
Figure 5.21	Wedge shaped mesh elements forming the inlet stabilizing section of the device (Section 1).....	68
Figure 5.22	Tetrahedral mesh elements in the converging section of the nozzle (Section 2). The element volumes shrink as they get closer to the throat. ....	68
Figure 5.23	A planar cut view of the mesh elements in the converging section of the nozzle – (Section 2).....	69
Figure 5.24	Mass flow rate through the U-shaped nozzle as a function of inlet pressure. ....	72
Figure 5.25	Mach number contours used in the determination of the position of the shockwave. ....	73
Figure 5.26	Variations of velocity magnitude along the U-shaped section. Angles show positions along the U-shaped section where zero degree denotes the beginning of the section and 180 its end. ....	74
Figure 5.27	Extrapolation of the diffuser and its intersection with the U shaped section of the device. ....	75
Figure 5.28	Results of CFD modeling indicating mass flow rate of a U-shaped nozzle with respect to the area of the throat. Note that the flow is choked at all times. ....	77
Figure 5.29	The decreasing radius profile developed for the U-shaped section of the nozzle. ....	78
Figure 5.30	Linear decrease of the curvature radius with respect to the angular position of the curvature.....	79
Figure 5.31	Occurrence of a shockwave inside the U-shaped section with constant cross-sectional area. ....	80

Figure 5.32	Centrifugal acceleration along the U-shaped section of the nozzle. Degrees represent the position along the U-shaped section where 0 degree is the beginning of the U and 180 is the end of it. ....	82
Figure 5.33	Contours of volume density of the particles that pinpoint the position of the separation side channel.....	84
Figure 5.34	Comparison of centrifugal acceleration for the two proposed concepts: swirling flow of gas in a straight nozzle and U-shaped nozzle.....	87
Figure 6.1	The bottom piece of the lab test nozzle system. The 4 thicker channels are designed to accommodate temperature probes. All other channels are for pressure measurements.....	89
Figure 6.2	Process flow diagram describing the schematic setup of the pilot test. ....	90
Figure 6.3	The Haas VF-3 machining centre was used to machine the nozzle configuration and measurement channels out of the aluminum blocks (picture from <a href="http://www.haascnc.com/prod/pi/VF-3_lg.jpg">http://www.haascnc.com/prod/pi/VF-3_lg.jpg</a> ). ....	93
Figure 6.4	A shot of the machined aluminum block showing the nozzle configuration and measurement channels.....	94
Figure 6.5	A shot of the machined aluminum block showing the measurement channels and NPT fitting threads. ....	95
Figure 6.6	A shot of the test apparatus showing the assembled nozzle and installed fittings and thermocouple probes. ....	96
Figure 6.7	Pressure measurement manifold. The elbow on the far left is to be connected to the pressure gauge.....	96
Figure 6.8	The equipment used for the experiment. ....	97
Figure 6.9	Comparison of the pressure measurements along the device with the CFD simulated pressure values. Inlet pressure is 172 kPa and the outlet back pressure is 138 kPa.....	101
Figure 6.10	Comparison of the pressure measurements along the device with the CFD simulated pressure values. Inlet pressure is 414 kPa and the outlet back pressure is 276 kPa.....	101
Figure 6.11	Mass flow rate measurements from the experiment compared to the CFD simulated results for different inlet pressures. ....	102

## LIST OF TABLES

Table 4.1	Summary of mesh elements used to represent the studied geometries. ....	27
Table 5.1	The boundary layer thicknesses of the scaled nozzle models.....	37
Table 5.2	The dimensions of the nozzle geometry used in the discussions.....	41
Table 5.3	Mass flow rate values for different gas inlet pressures.....	43
Table 5.4	Summary of the comparison between the two proposed configurations ....	86

# NOMENCLATURE

## Units:

K/s : Kelvin per second

Pa: Pascal

hr: hour

atm: atmosphere

psi: pounds per square inch

scfm: standard cubic feet per minute

Hp: horse power

## Symbols:

$g$ : natural gravitational acceleration ( $\sim 9.8 \text{ m/s}^2$ )

$x_{th}$ : axial position of the throat (distance from the inlet)

$L$ : total length of the nozzle

$D_{in}$ : inlet diameter

$D_{out}$ : outlet diameter

$D_{th}$ : throat diameter

$P_{in}$ : inlet pressure

$P_{out}$ : outlet back pressure

$P_{th}$ : pressure at the throat

$P_L$ : pressure loss ratio

$P_L$ : pressure recovery ratio

$T_{in}$ : temperature at the inlet

$T_{th}$ : temperature at the throat

$u$ : velocity of gas

$u_{throat}$ : velocity of gas at the throat

$c$ : speed of sound

$Ma$ : Mach number

$R$ : universal gas constant (8.314 kg/mol.K)

$M$ : molecular weight

$\dot{m}$ : mass flow rate

$A$ : cross-sectional area

$V_{tangential}$ : tangential component of the velocity vector

$V_{axial}$ : axial component of the velocity vector

$S$ : swirl intensity

$a_c$ : centrifugal acceleration

$r$ : distance from the centre of rotation

### **Greek Symbols:**

$\omega$ : angular velocity

$\psi$ : area-weighted average centrifugal acceleration

$\zeta$ : swirl velocity ratio

$\zeta_0$ : initial swirl velocity ratio

$\rho$ : density of the gas

$\rho_{th}$ : density of the gas at the throat

$\gamma$ : heat capacity ratio ( $C_p/C_v$ )

# 1. INTRODUCTION

Natural gas is one of the most important sources of energy in the world. Currently it accounts for more than 25% of the world's primary energy consumption. With the drive for cleaner fuels, the demand for natural gas is forecast to grow 1 to 3.5% per year for the next 20 years (IEO2007). The safe, efficient, and economic production, processing, and transportation of natural gas, especially from reservoirs in remote and offshore locations, remain a major challenge to supply the consumption markets. One of the main problems in the production and transportation of gas is the possibility of hydrate formation, an ice like crystalline structure formed when low molecular weight hydrocarbons are in contact with water. The production and transportation systems become troubled when the flowlines get obstructed with solidified hydrate.

Natural gas can carry certain amounts of water in the vapour form. Water is a contaminant in natural gas and its concentration increases with temperature or equally with reduced pressure. Physical appearance of gas hydrates is like packed snow. A mass of hydrate is very porous and light. The conditions at which hydrates start to solidify, and become a cause for trouble, depend on many factors including but not limited to gas temperature, pressure, composition, and the water content. Therefore it is very important to develop techniques to prevent hydrate formation.

The following methods have been conventionally used for hydrate prevention:

1. Identifying the temperature at which hydrates form and keeping the gas above this temperature.
2. Reducing pressure and therefore reducing the possibility of hydrate formation.
3. Adding hydrate inhibitors to the gas, which in turn will either reduce the temperature at which hydrates are likely to form or the rate at which they form. These include antifreeze agents such as methanol and glycols, and kinetic inhibitors.
4. Reducing the water content of the gas and therefore reducing the possibility of hydrate formation. This process is called gas dehydration.

While the first three methods seem to be either costly or proposing their own risks (i.e. loss of valuable pressure, or use of chemicals), gas dehydration is one of the more efficient choices. The following techniques have been practiced for gas dehydration process: (Karimi, 2006)

- i. Refrigeration through the Joule-Thomson expansion or other means of cooling, and then separation of liquefied water content of the gas by means of any conventional gas/liquid separator.
- ii. Solid desiccant dehydration or dry-bed dehydration. Gas is flowed through a bed of solid reagent where the water is removed. Adsorbents also known as desiccants such as silica gel, molecular sieve, activated alumina and activated carbon materials are materials with high capacity for absorbing water.

- iii. Liquid desiccant dehydration. A liquid absorber will make close contact with the wet gas by means of a gas/liquid contact device (e.g., trayed or packed towers). A good absorber like glycols will absorb the water content of the gas and ultimately dry the gas.

A new technology based on the adiabatic cooling of swirling gas flow in a supersonic nozzle has been recently proposed and developed for conditioning of natural gas. The supersonic separator has similar thermodynamics to a turbo expander, combining expansion, cyclonic gas/liquid separation and recompression in a compact, tubular device. A turbo expander transforms pressure to shaft power, whereas in supersonic separator, it is transformed to kinetic energy. The supersonic devices can also be used to remove condensable vapours such as water or natural gas liquids (NGL) from a gas stream in order to lower the (water or hydrocarbon) dew point of the gas or strip the gas of heavy hydrocarbons which can generate additional revenue. The three main physical processes involved in the operations of supersonic separators are (Prast et al., 2006):

- A near isentropic expansion resulting in a low temperature and pressure due to the high (supersonic) velocity,
- Non-equilibrium condensation of vapours resulting in a fine mist of sub-micron sized droplets, and
- Separation by inertia of droplets heavier than the surrounding gas due to a strong swirling flow.

During the fast isentropic expansion in the nozzle, a gas containing condensable vapours accelerates to the supersonic velocity, and the temperature of the mixture drops with a very high cooling rate ( $10^4$ - $10^6$  K/s). A super-cooled non-equilibrium state is attained, in which no condensation has yet taken place. This metastable state does not last long. At some point in the supersonic part of the nozzle, nuclei of vapour molecules will spontaneously form. The nucleation rate becomes very high, and a large number of very small droplets, typically the size of a few nanometres, are almost instantaneously formed. Because of the very high concentration of small droplets ( $>10^{15}$  m<sup>-3</sup>), foreign particles acting as nucleation sites play no role in this condensation process; it is therefore considered a homogeneous condensation process (Prast et al., 2006). As the vapour mixture is still super-cooled (or supersaturated) these small nuclei will grow to form droplets. The gas then depletes and returns to the equilibrium or saturated state. The two-phase mixture continues its supersonic swirling flow and under the influence of the strong inertial force ( $10^5$ - $10^6$ g), the droplets will collide with the wall and merge. A thin film of water will form around the swirling gas which then will be separated by means of a vortex finder as in cyclones. The gas is now dry, and will slow down in the diverging part of the nozzle, regaining almost 70% of its original pressure. (Prast et al., 2006)

The supersonic nozzle has great advantages over other methods of dehydration in that it:

- significantly reduces size and weight of gas processing modules
- does not use rotating equipment or has any moving parts
- has the capability to perform in subsea modules

- can be tuned to remove only water, or water and heavy hydrocarbons or other components
- does not require chemicals
- has no emissions to the environment
- enables unmanned operations thereby improving personnel safety
- results in both capital and operating cost savings in the order of 25% of the total project cost

#### 1.1. OBJECTIVES OF STUDY

The purpose of this thesis is to investigate and analyze the design characteristics and operating conditions of supersonic separators. The ultimate objective is to identify venues to improve performance, explore potential design features and establish operational criteria. Possible alternate configurations to the original swirling flow of gas in a supersonic nozzle are also to be investigated and compared to the original design in terms of separation efficiency.

#### 1.2. SCOPE OF STUDY

Based on the literature reviews, three different groups have studied supersonic separators. Two of these groups have already implemented commercial supersonic separators in gas treatment plants. Despite these efforts, limited data is still available regarding the performance and design characteristics of these separators. This research is intended to

fill the knowledge gap and provide extensive analytical data on the performance of supersonic separators.

### 1.3. THESIS OUTLINE

This thesis is divided into six chapters. Chapter 1 is an introduction to the concept of supersonic separators and their function and potential applications in today's oil and gas industry. Chapter 2 provides an overview of all previous work on the proposed concept. In Chapter 3, further introduction to the supersonic separators is provided and the methodologies used in conducting this research are explained. Chapter 4 is dedicated to presenting the results of the study and corresponding discussions. In Chapter 5, the experimental tests performed to evaluate the computer based simulations are explained and the results are presented and discussed. Finally, Chapter 6 summarizes the thesis and presents conclusions and recommendations for future work.

## 2. LITERATURE REVIEW

The concept of supersonic separators was introduced to the oil and gas industry in 1990s. These separators were immediately identified as reliable devices with no rotating parts that required no chemicals and were capable of unmanned operation. It has been the purpose of a few studies since then to optimize the performance of supersonic separators and to expand their functionality from a dehydration device to a more sophisticated hydrocarbon dew-pointing and NGL recovery device. The following is a quick review of the achievements of these studies.

The first group known to conduct studies on supersonic separators was an engineering group from the Netherlands that is now affiliated with Twister BV. Their study of supersonic separators is tracked back to 1997 and their first full scale test unit became operational in 1998 (Brouwer et al., 2004). The first commercial gas conditioning technology using the supersonic separator in the offshore applications was started up in December 2003 (Brouwer et al., 2004). Their proposed design consisted of a supersonic nozzle that incorporated a small blade (supersonic wing) in the supersonic region to create the swirling motion of the gas and hence benefit from the centrifugal separation of the heavier particles (Brouwer et al., 2004). This design was later improved to include a swirl generator (ring wing) upstream of the nozzle and in the subsonic region (Schinkelshoek et al., 2006). Another group known for their extensive work on the supersonic separators is a group of Russian specialists who named their separator 3-S.

This group joined Translang Technologies Ltd., Calgary. 3-S separators performances have been studied and tested since 1996 (Alfyorov et al., 2005). An experimental test plant was constructed in Russia. Later another pilot plant for greater natural gas flow rate was built in Calgary. None of these facilities was capable of very high pressures. The first industrial 3-S separator became operational in Western Siberia (Alfyorov et al., 2005). The design of the 3-S separator was similar to the improved *Twister* design, incorporating a swirl generator upstream of the nozzle. A third Chinese group has also performed studies on supersonic separators. They built a pilot scale test which used wet gas as process fluid (Hengwei et al., 2005) which was capable of attaining a dewpoint depression of about 20°C. Their design used a cyclonic swirl generator in the supersonic region. Another study was performed by a group in Newfoundland, Canada on which the current study is based. They performed CFD based predictions of the flow characteristics inside a converging-diverging nozzle and showed that this method is a valid tool for this type of study by comparing their results with similar published experimental data (Jassim, 2008). They moreover developed a software that linked to a process simulator (HYSYS), was capable of predicting the performance of a supersonic separator under certain operating conditions with much less computational resources than a CFD package (Karimi, 2009).

A supersonic dehydration unit may be consisted of several parts, the most important of which is a converging – diverging supersonic nozzle. It is in this nozzle where the condensation or as it may be in some cases, solidification occurs as well as the separation itself. Since the gas mixture is flowing at supersonic velocities, residence time is

extremely low in this type of separators and hydrate has no time to deposit along the device. The unit is considerably smaller than conventional dehydration units and therefore suitable for offshore applications (Brouwer et al., 2004). Moreover, the nozzle has no moving parts and is simple to operate which makes it a very good candidate for unmanned operations (Brouwer et al., 2004 and Schinkelshoek, 2006) for subsea application. It is also important to note that the gas temperature is reduced based on gas expansion principles and requires no external refrigerant. This brings another major advantage over conventional dehydration units in that intensive water dew points, down to  $-60\text{ }^{\circ}\text{C}$ , can be achieved without any use of external cooling (Karimi, 2009). The selectivity of separation is another asset when water is removed without the removal of hydrocarbons. This is beneficial in that presence of heavier hydrocarbons ( $\text{C}_2^+$ ) increases the gas gravity and reduces the compressibility factor, which results in increased pipeline mass flow capacity (Mohitpour et al., 2003).

Malyshkina (Malyshkina, 2008) developed mathematical simulations for velocity components, pressure and other parameters as functions of radius for flow within the supersonic separator using the two dimensional Euler model. Qingfen, Depang, and other colleagues (Qingfen et al., 2009) investigated the performance of supersonic separators incorporating a method of particle enlargement to reduce the length of the device. They used air-ethanol as their medium and water droplets as nucleation centers.

### **3. CFD AND THE GOVERNING EQUATIONS**

As computational fluid dynamics (CFD) is used as the main tool in the conduction of this study, it is necessary to briefly explain the method and the equations involved in the process. CFD is a widely adopted method of studying and more importantly predicting the flow characteristics of fluid systems. It uses mathematical equations that describe the system, usually in the form of partial differential equations, and utilizes a computer to solve them simultaneously to predict the flow field characteristics of a given system. It is therefore a combination of fluid mechanics, mathematics, and computer sciences. The equations that define the system are derived from conservations laws, thermodynamic laws, gas equations of state, and so on. These equations are usually rearranged such that the computational cost of their simultaneous solution is minimized while the integrity of the overall solution remains robust. The remainder of this chapter is dedicated to presenting the most important of these equations as they are used by Fluent.

#### **3.1. GOVERNING EQUATIONS**

There are many sets of equations that govern the transport phenomena in any given system. The most important of these equations are suitable expressions of the three conservation laws; namely mass, momentum, and energy conservation laws. If the system being studied includes two or more species, separate conservation and/or reaction equations for each species may be solved as well. Additional transport equations are

employed when the flow is turbulent. The governing equations used to describe the systems in this study are as follows.

### Conservation of Mass

The equation for conservation of mass, or the continuity equation, may be written as:

$$\frac{\partial \rho}{\partial t} + \nabla \cdot (\rho \bar{v}) = S_m \quad 3.1$$

For two dimensional axis-symmetric geometries, this equation can be reduced to:

$$\frac{\partial \rho}{\partial t} + \frac{\partial}{\partial x}(\rho v_x) + \frac{\partial}{\partial r}(\rho v_r) + \frac{\rho v_r}{r} = S_m \quad 3.2$$

$S_m$  denotes the source term which is zero for all cases in this study.  $x$  and  $r$  are axial and radial coordinates respectively and  $v_x$  and  $v_r$  are the axial and radial components of the velocity vector.

### Conservation of Momentum

Conservation of momentum may be described by:

$$\frac{\partial}{\partial t}(\rho \bar{v}) + \nabla \cdot (\rho \bar{v} \bar{v}) = -\nabla p + \nabla \cdot (\bar{\tau}) + \rho \bar{g} + \bar{F} \quad 3.3$$

Where  $p$  is the static pressure,  $g$  is the gravitational acceleration,  $F$  is the external body forces.  $\bar{\tau}$  is the stress tensor described as follows:

$$\bar{\tau} = \mu \left[ (\nabla \bar{v} + \nabla \bar{v}^T) - \frac{2}{3} \nabla \cdot \bar{v} I \right] \quad 3.4$$

For two dimensional axis-symmetric geometries, the axial, radial, and swirl velocity momentum conservation equations are derived as follows:

$$\begin{aligned} \frac{\partial}{\partial t}(\rho v_x) + \frac{1}{r} \frac{\partial}{\partial x}(r \rho v_x v_x) + \frac{1}{r} \frac{\partial}{\partial r}(r \rho v_r v_x) = & -\frac{\partial p}{\partial x} + \frac{1}{r} \frac{\partial}{\partial x} \left[ r \mu \left( 2 \frac{\partial v_x}{\partial x} - \frac{2}{3} (\nabla \cdot \bar{v}) \right) \right] \\ & + \frac{1}{r} \frac{\partial}{\partial r} \left[ r \mu \left( \frac{\partial v_x}{\partial r} + \frac{\partial v_r}{\partial x} \right) \right] + F_x \end{aligned} \quad 3.5$$

$$\begin{aligned} \frac{\partial}{\partial t}(\rho v_r) + \frac{1}{r} \frac{\partial}{\partial x}(r \rho v_x v_r) + \frac{1}{r} \frac{\partial}{\partial r}(r \rho v_r v_r) = & -\frac{\partial p}{\partial r} + \frac{1}{r} \frac{\partial}{\partial r} \left[ r \mu \left( 2 \frac{\partial v_r}{\partial r} - \frac{2}{3} (\nabla \cdot \bar{v}) \right) \right] \\ & + \frac{1}{r} \frac{\partial}{\partial x} \left[ r \mu \left( \frac{\partial v_r}{\partial x} + \frac{\partial v_x}{\partial r} \right) \right] - 2 \mu \frac{v_r}{r^2} + \frac{2}{3} \frac{\mu}{r} (\nabla \cdot \bar{v}) + \rho \frac{v_x^2}{r} + F_r \end{aligned} \quad 3.6$$

$$\begin{aligned} \frac{\partial}{\partial t}(\rho \omega) + \frac{1}{r} \frac{\partial}{\partial x}(r \rho v_x \omega) + \frac{1}{r} \frac{\partial}{\partial r}(r \rho v_r \omega) = & \frac{1}{r} \frac{\partial}{\partial x} \left[ r \mu \frac{\partial \omega}{\partial x} \right] \\ & + \frac{1}{r^2} \frac{\partial}{\partial r} \left[ r^3 \mu \frac{\partial}{\partial r} \left( \frac{\omega}{r} \right) \right] - \rho \frac{v_r \omega}{r} \end{aligned} \quad 3.7$$

where:

$$\nabla \cdot \bar{v} = \frac{\partial v_x}{\partial x} + \frac{\partial v_r}{\partial r} + \frac{v_r}{r} \quad 3.8$$

and  $\omega$  is the swirl velocity component.

In the special case of an inviscid flow where the viscosity of the fluid is considered negligible,  $\bar{\tau} = 0$  and hence the momentum conservation equations reduce to:

$$\frac{\partial}{\partial t}(\rho \bar{v}) + \nabla \cdot (\rho \bar{v} \bar{v}) = -\nabla p + \rho \bar{g} + \bar{F} \quad 3.9$$

### Conservation of Energy

The energy equation is solved as the following form:

$$\frac{\partial}{\partial t}(\rho E) + \nabla \cdot (\bar{v}(\rho E + p)) = \nabla \cdot \left( k_{eff} \nabla T - \sum h_j \bar{J}_j + (\bar{\tau}_{eff} \cdot \bar{v}) \right) + S_h \quad 3.10$$

where  $k_{eff}$  is the effective conductivity defined as the sum of normal conductivity and turbulent thermal conductivity defined by the turbulence model being used.  $\bar{J}_j$  is the diffusion flux of species  $j$  and  $S_h$  includes the heat of chemical reaction or other heat sources defined in the system. Moreover:

$$E = h - \frac{p}{\rho} + \frac{v^2}{2}$$

where  $h$  is the sensible enthalpy defined as the mass fraction averaged enthalpy of all species.

## 4. STUDY OF SUPERSONIC SEPARATORS

The purpose of this thesis is to study and analyze the performance of supersonic separators with different designs and in diverse operating conditions in search of an optimum design for specific operating conditions in terms of separation efficiency and pressure recovery. In order to accomplish this task, several different separators have been designed and their performances have been studied using a commercial CFD package. A new design with a U-shaped throat was proposed in this thesis and its performance was benchmarked against existing swirl type nozzles. In the following chapters the methodology, procedures, and steps taken to complete this study will be discussed.

### 4.1. METHODOLOGY

The methodology of this study is mainly based on the use of numerical solutions performed with the Fluent CFD software package and verification of the modeling using experimental method. The proposed separator concepts were modeled using the CFD package and their performance was examined under different operating conditions. The results were then compiled and analyzed in terms of separation rate and efficiency, mass flow rate, centrifugal force, pressure loss, and pressure recovery ratio. The most efficient design and operating conditions were then determined by analyzing these results. The final step in the study was the verification of the CFD simulated results with experimental data. Due to the novel nature of the proposed nozzle, experimental data was not available for comparison. An experimental test set-up was therefore designed and built to perform

tests and the results were compared to those obtained from the CFD simulations of the same design for evaluation purposes. The details of the experimental set-up and evaluation results are presented in Chapter 6 of this thesis. The details of the CFD modeling and simulations are presented in the remaining sections of this chapter.

The procedures involved in the modeling and simulation of a certain concept may be categorized into three steps:

1. Pre-processing: including creation of the geometry and mesh generation procedures for CFD modeling.
2. Processing: introducing the geometry in the numerical solver and defining material properties, boundary conditions, and solution criteria and algorithms.
3. Post-processing: methods of data collection and the types of data gathered from the numerical solver, comparison methods, and data analysis.

The following is a detailed explanation of these steps.

#### 4.2. PRE-PROCESSING

This step involves the procedures undertaken to create the nozzle geometry and to mesh the geometry efficiently. These are performed by the GAMBIT software, version 2.4 which is the mesh and geometry generation software specially developed for the processing software used in this study, namely Fluent 6.2.3. Both these software packages are developed by ANSYS.

#### 4.2.1. Geometry Creation

The creation of geometry in GAMBIT may be performed through many different approaches. The method used in this research is as follows:

The nozzle's converging and diverging profiles are first established in a Microsoft Excel spreadsheet by determining the four design parameters: inlet and outlet diameters, throat diameter, axial position of the throat, and total length of the nozzle. The profiles created based on these parameters were regressed to the following third order polynomials:

For converging section:

$$y = A \left( \frac{x}{x_{th}} \right)^3 + B \left( \frac{x}{x_{th}} \right)^2 + \frac{D_{in}}{2} \quad 4.1$$

$$A = D_{in} - D_{out}, \quad B = -\frac{3A}{2}$$

and for diverging section:

$$y = A' \left( \frac{L-x}{x_{th}} \right)^3 + B' \left( \frac{L-x}{x_{th}} \right)^2 + \frac{D_{out}}{2} \quad 4.2$$

$$A' = (D_{out} - D_{th}) \left( \frac{x_{th}}{L-x_{th}} \right)^3, \quad B' = -\frac{3A'}{2} \left( \frac{L-x_{th}}{x_{th}} \right)$$

Where:

$D_{in}$ : Inlet diameter of the converging section.

$D_{out}$ : Outlet diameter of the diverging section. (It is assumed here that  $D_{in} = D_{out}$ )

$D_{th}$ : Nozzle throat diameter.

$x_{th}$ : Nozzle throat axial position.

$L$ : Nozzle overall length.

The spreadsheet is used to generate a finite number of Cartesian coordinates corresponding to points that fall along the proposed profile for the nozzle wall, based on Equations 4.1 and 4.2. These coordinates are then imported into GAMBIT as vertices, using import ICEM Input function (GAMBIT 2.4 User's Guide, May 2007 – Page 4-33), and are used as a guideline to create the desired geometry. Two types of geometry are used in this study: 1) a two dimensional axial cross-section of half of the nozzle (see Figure 4.1), which is used as an axis-symmetric body for initial solutions; and 2) a complete three dimensional model (Figures 4.2 and 4.3) which is used for more accurate solutions.

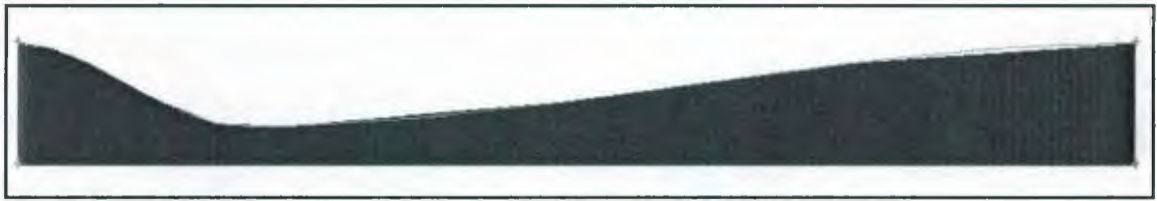


Figure 4.1 Two dimensional geometry, used as an axis-symmetric body to simulate a typical nozzle



Figure 4.2 A typical three dimensional geometry used for CFD simulation in this research.



Figure 4.3 A Typical three dimensional geometry: nozzle with extended U-shaped section.

In the creation of U-shaped nozzles with variable radius curvature shown in Figures 4.4 and 4.5, another spreadsheet was used to generate the coordinates of a set of vertices that would be utilized to create the curvature profile. Axis-symmetric modeling was clearly not an option here. Had a rectangular cross section been assumed for the nozzle, a two dimensional model would have represented the geometry in the numerical solver. The

circular cross section of the proposed nozzle enforced the application of a three dimensional model for this geometry.

The nozzles used in this study have the following design parameters. Note that the dimensions are presented without a unit here as this is how they are created in GAMBIT.

Proper units are assigned to the geometry in the processing software (Fluent).

$$D_{in} = D_{out} = 2$$

$D_{th}$ : ranging from 0.2 to 0.7

$x_{th}$ : ranging from 20 to 50

$L$ : ranging from 100 to 300

$R$  (the curvature radius of the U-shaped section): ranging from 0.5 to 50

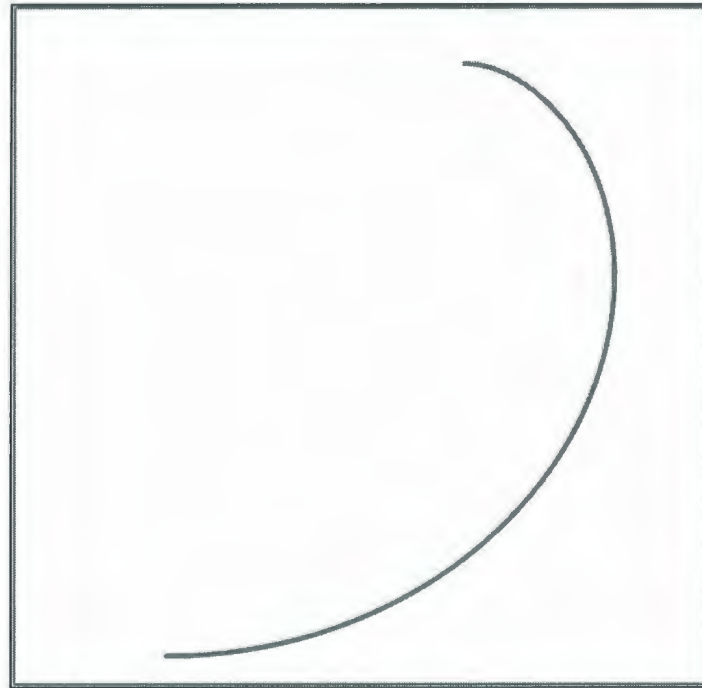


Figure 4.4 Profile for a variable radius curvature created in Microsoft Excel

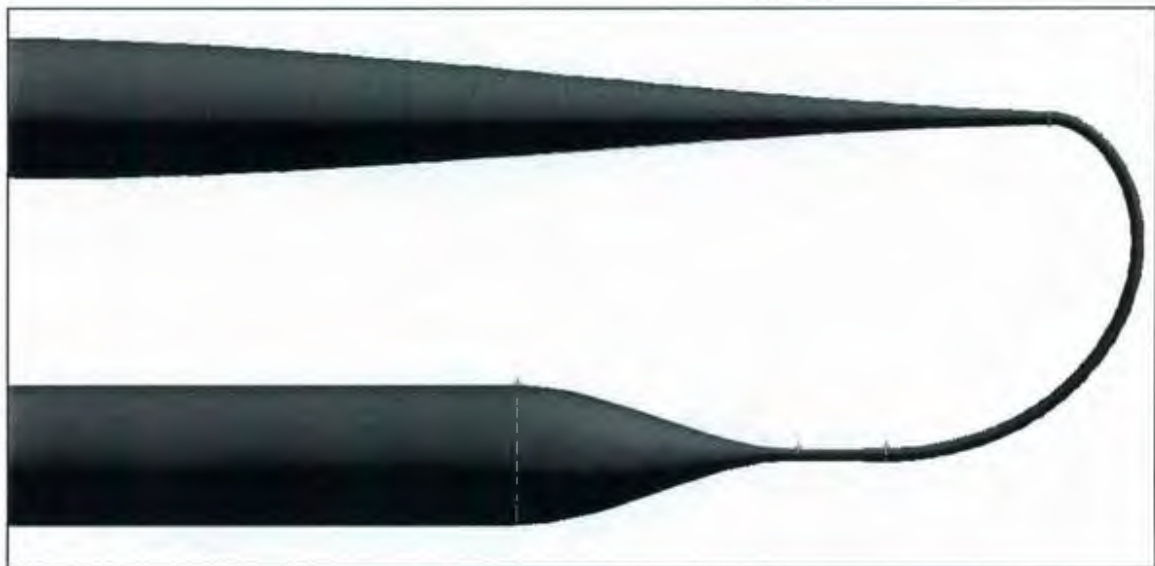


Figure 4.5 A three dimensional geometry: nozzle with extended U-shaped section that follows a variable radius curvature profile.

#### 4.2.2. Mesh Generation

It is well understood that the quality of the mesh is a key factor in the accuracy and stability of a finite element analysis. Various characteristic properties of the geometry itself, types of fluids involved, and the amount of available memory and processing capability are some of the parameters that contribute to the final selection of a specific mesh design.

GAMBIT allows two types of mesh elements for a surface, namely triangular and rectangular elements, as can be seen in Figure 4.6. The volume mesh elements can in turn take four shapes, namely tetrahedral, wedge, pyramidal, and hexagonal. Triangular elements were used to mesh the circular cross section of the nozzles as they create less skewed elements compared to rectangular elements. The volume elements were therefore wedge-shaped where possible (see Figure 4.7) and tetrahedral where axial mapping was not possible. Specifically, axial mapping is not possible or is simply not efficient in the converging section of the nozzle where there is considerable gradient in the cross sectional area (see Figure 4.8).

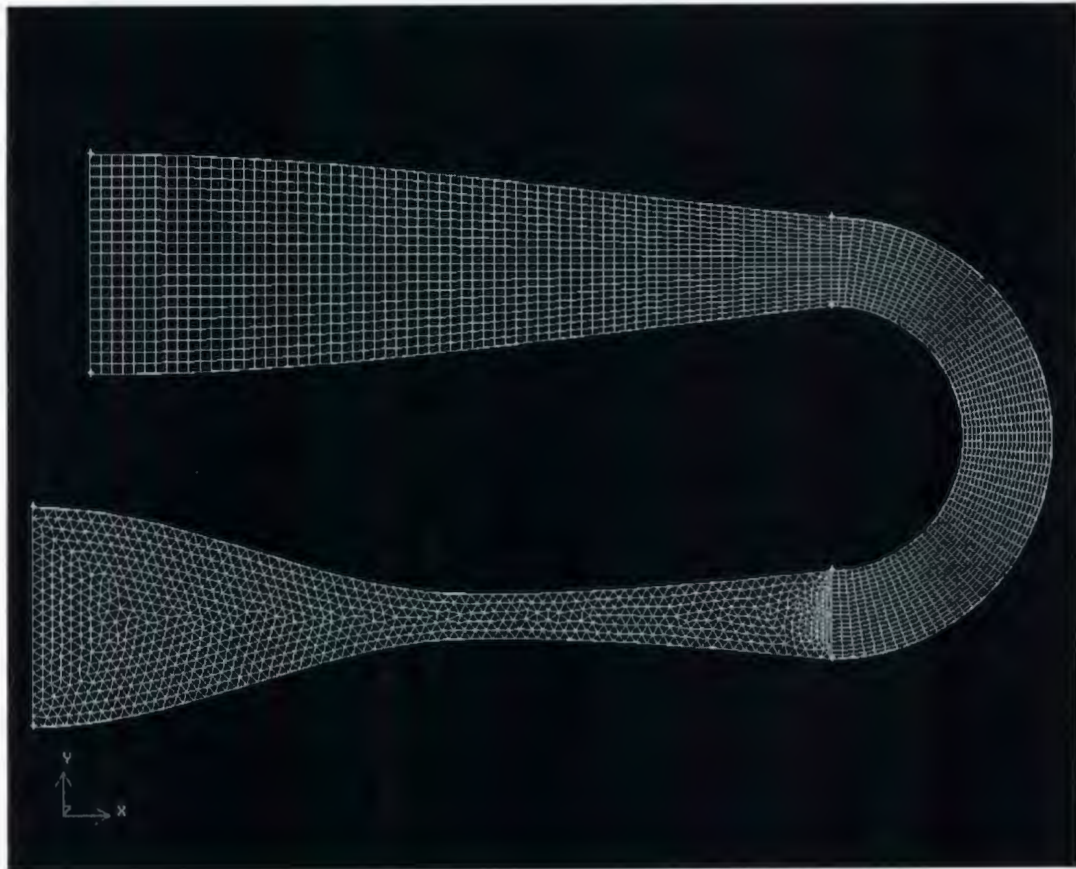


Figure 4.6 Typical triangular and rectangular face mesh elements used in CFD simulations.

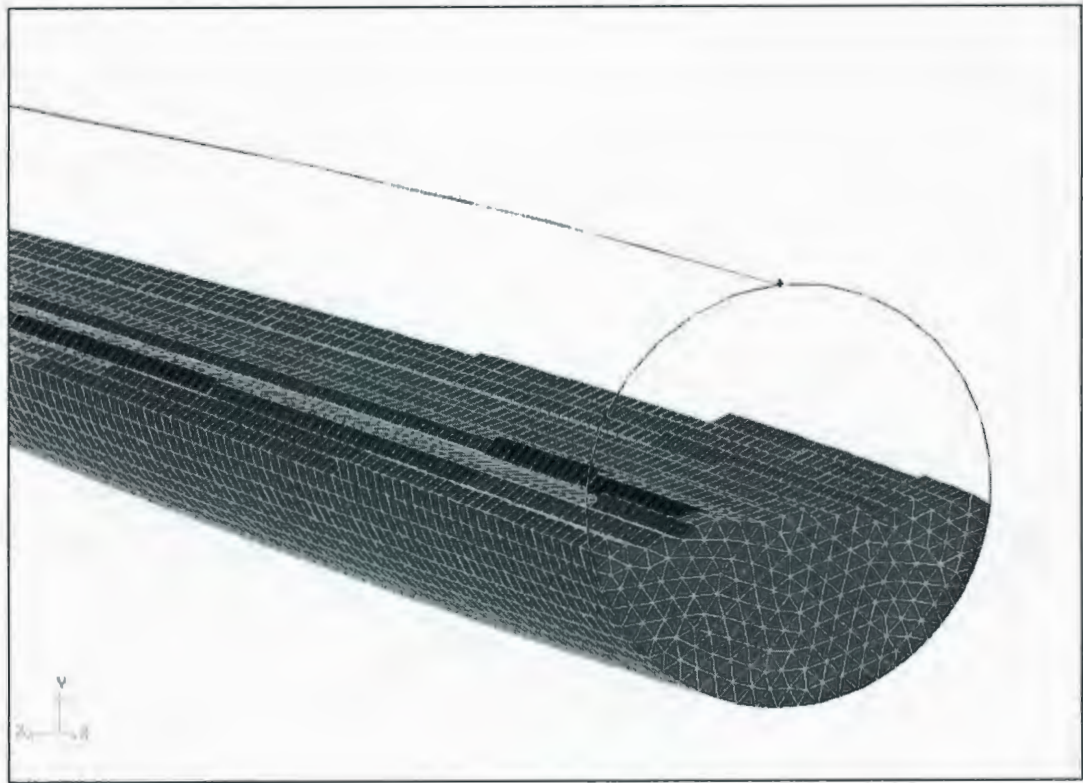


Figure 4.7 Typical wedge-shaped volume mesh elements.

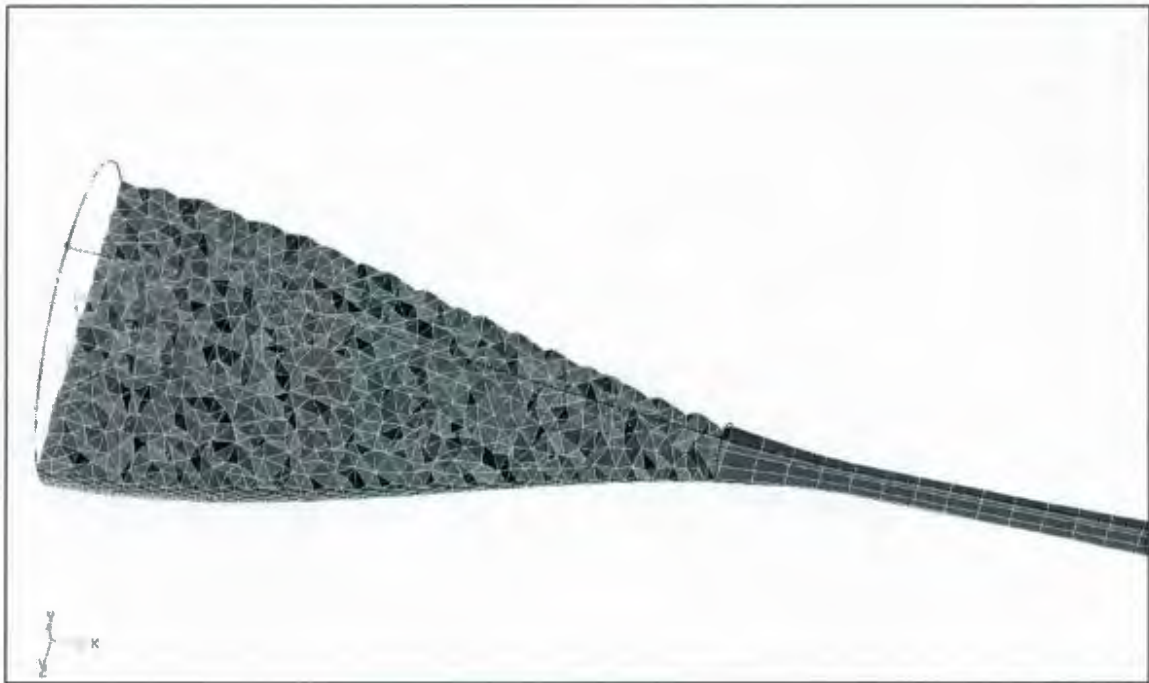


Figure 4.8 Tetrahedral volume mesh elements in the converging section of the nozzle followed by wedge elements in the throat.

In meshing a surface or a volume, as the size of the mesh elements decrease, the model becomes more accurate, but the amount of memory and CPU resources required to solve the model increase. Creating a fine enough mesh where a reliable accuracy does not require too much computational resource is therefore a challenge. In order to find the optimal mesh size required to perform accurate simulations with the resources at hand, a series of meshing schemes with decreasing element size were generated for a single geometry. The solutions that the CFD simulator produced for each scheme and the required CPU and memory resources were then analyzed find the optimal meshing scheme. The analysis was based on the relative improvements and level of accuracy each scheme provided when solved under the same conditions. Parameters of interest were

mainly flow field properties such as pressure and velocity profiles as well as the position of the shock wave. It should be noted here that a special dynamic mesh adaptation was employed to capture real gas shock wave properties the details of which will be presented in later chapters.

Mesh generation for boundary layers is another issue that requires delicate attention. It is important that the boundary layer is represented with a meshing that is fine enough to account for the sharp gradients that appear in that region. When the media being investigated is a low viscosity fluid flowing with supersonic velocity, this layer becomes very thin. GAMBIT provides valuable tools for this purpose (GAMBIT 2.4 Modeling Guide, Vol. 2, Chapter 3.1). Figures 4.9 and 4.10 show how these features were used in this study. Figure 4.9 shows the use of boundary layers in the wall boundary region for a three dimensional model. In Figure 4.10 the use of boundary layers is shown in both wall and axial regions of a two dimensional axis-symmetric model. Table 4.1 is a summary of the mesh element types used to represent the different parts of the geometries studied.

Table 4.1 Summary of mesh elements used to represent the studied geometries.

Mesh element dimension	Mesh element type	Location used
2D (Surface)	Triangular	<ul style="list-style-type: none"> <li>• Nozzle circular cross section</li> <li>• Nozzle wall at converging sections with small <math>r_{throat}/r_{inlet}</math></li> </ul>
	Rectangular	Nozzle wall boundaries
3D (Volume)	Tetrahedral	Nozzle body at converging sections with small $r_{throat}/r_{inlet}$
	Wedge	Nozzle main body
	Hexagonal	Boundary layers

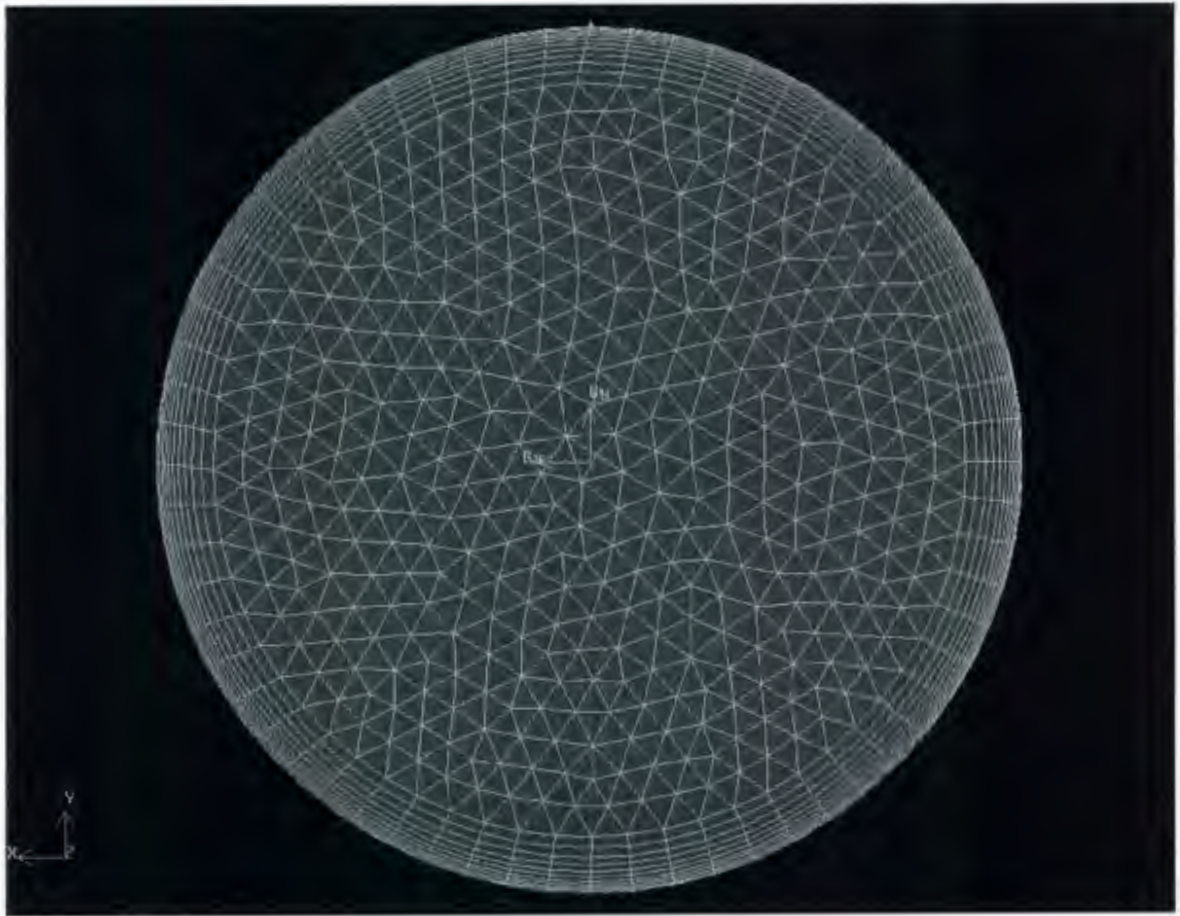


Figure 4.9 Boundary layer is modeled by ten rows of hexagonal elements that get thinner as they approach the wall.

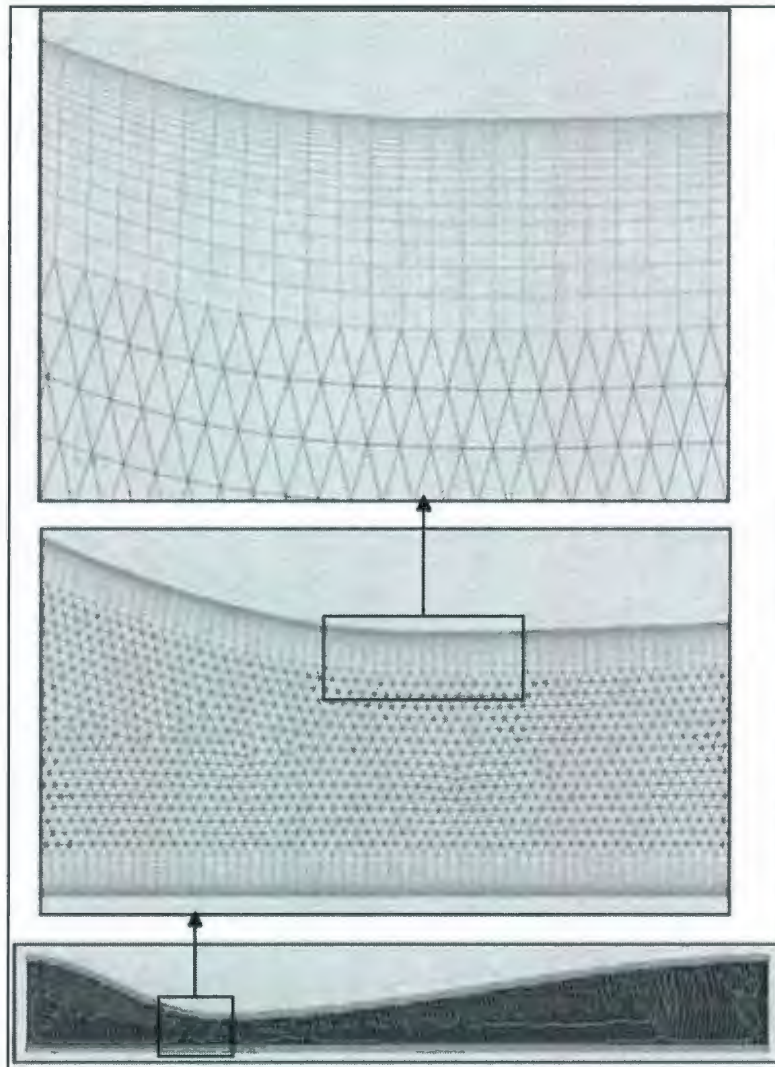


Figure 4.10 Boundary layers used near the wall and in the centre to account for wall boundary layer effects and high tangential velocity gradients near the axis of the nozzle.

#### 4.3. PROCESSING

As previously noted, the software used for defining a system and solving it for a certain set of boundary conditions in this CFD package is Fluent 6.3.26. Defining a system involves identifying the equations that describe that system, such as mass and momentum

conservation equations, as well as physical properties of the fluids at different conditions. Solving these equations simultaneously and closing them with the appropriate boundary conditions is usually referred to as the processing stage. There are two groups of parameters that need to be adjusted in order to solve a system:

- a) Parameters that define the system itself. This includes the units and dimensions used in the geometry, types and properties of the materials involved in the process, and boundary conditions that close the system.
- b) Parameters that determine the solution algorithm and convergence criteria.

The remainder of this section is dedicated to explaining how these parameters were defined in this study.

#### 4.3.1. Geometry properties

The geometry that was created and meshed using GAMBIT, the pre-processing software, GAMBIT is imported into Fluent, the processing software. As it was previously mentioned, the geometry created by GAMBIT has no units assigned to its dimensions, but since GAMBIT is designed specifically for Fluent, everything else such as types of boundaries and walls are already assigned. The only step left in defining the geometry is therefore assigning a unit to the geometry. Metric units were mostly used throughout the study, but English units were also used in some cases for evaluation purposes

#### 4.3.2. Materials and their physical properties

The fluid that is to be modeled is natural gas, which consists mainly of methane. Therefore methane was used as the process fluid in most of the simulations. More realistic simulations considering the actual gas composition are unique for any specific gas reservoir and beyond the scope of this study. As the tests were performed using compressed air, air was also used in some simulations as the process fluid. The physical properties of the gases were defined using the ideal gas law for the majority of the simulations. The National Institute of Standards and Technology (NIST) real gas models are available in Fluent for 39 pure fluids including methane. Thermodynamic and Transport Properties of Refrigerants and Refrigerant Mixtures Database version 7.0 (REFPROP v7.0) was used to predict real gas properties in some simulations to compare with ideal gas results.

#### 4.3.3. Governing equations

The equations that govern the system are not directly set in Fluent. The general characteristics of the system and fluids are instead used to determine these equations. For instance, type of flow can be chosen to be inviscid, laminar, or turbulent, which will consequently decide which terms of the Navier-Stokes equations are used to model the system. The systems are initially modeled using an inviscid flow of ideal gas. More detailed models are used for final results which incorporate k-epsilon turbulence models and where necessary real gas models to create more accurate results. k- $\epsilon$  model was chosen as it is the most widely accepted model to represent such flows in the industry and

it is the recommended choice of turbulence model considering the high velocity and swirl of the flow as instructed by the Fluent user guide.

#### 4.3.4. Boundary conditions

Boundary conditions are used to define the known limits of the system. In the systems studied here, three regions have to be defined:

- 1) Nozzle inlet
- 2) Nozzle outlet
- 3) Nozzle walls

The inlet, in most of the systems, is defined as a *Pressure inlet*, which uses the pressure and temperature of the gas at the inlet as a constant and adjusts other parameters such as velocity and flow rate accordingly. *Mass flow inlet* was also used in some simulations to evaluate the effects of flow rate variations. This condition assumes the mass flow rate and temperature as a constant and adjusts the other parameters such as pressure and velocity correspondingly.

The outlet is always modeled as a *Pressure outlet* where the pressure and temperature of the gas are defined at the outlet. The walls are always modeled as a smooth and insulated surface where no flow of energy takes place. This is consistent with the theoretical assumption of an adiabatic expansion of the gas.

#### 4.4. POST-PROCESSING

This section explains the techniques and properties that were used to analyze and compare the solutions obtained from the CFD simulations for different proposed concepts.

The properties used in the determination of the optimum mesh element size include: position of the shock wave, shape of the shockwave, and velocity and pressure profiles in the device. Analysis was performed on the results acquired from different meshing schemes and sizes in terms of the relative improvements obtained in accuracy of the mentioned properties and in relation to the extended requirement for memory and CPU resources.

The properties that were used to evaluate the performance of a design include: maximum velocity achieved in the device, centrifugal acceleration, position of the shockwave, pressure loss, mass flow rate, residence time, and separation length.

All the above mentioned properties were reported in form of tables, graphs, contours, or vector plots as suited by the nature of the property and analysis methods.

## 5. RESULTS AND ANALYSIS

The results gathered from the simulations performed by CFD package are presented in this chapter. These results are categorized into three sections:

1. Straight nozzle: analyzing the dynamics of the swirling flow of gas in supersonic nozzles
2. U-shaped nozzle: investigating the flow characteristics of a novel concept incorporating a U-shaped section in the diffuser of supersonic nozzles.
3. Comparison of U-shaped and straight nozzles

Detailed discussions are presented Sections 4.1 to 4.3.

### 5.1. STRAIGHT NOZZLE WITH SWIRLING FLOW

The following sections discuss the results of the CFD simulations for the swirling flow of gas through straight nozzles with various design characteristics and operating conditions.

#### 5.1.1. Meshing scheme

As it was mentioned in Section 3.2.2., a trial and error scheme was used in order to determine the optimum size for the mesh elements in a proposed geometry. In light of the analysis of the results acquired from this study, the following guidelines were implemented in the meshing of the straight nozzle models:

- The elements should not be greater than ten percent of the diameter of the geometry they form. This recommendation is based on the analysis of models with larger various mesh sizes. It was determined from this analysis that larger meshes generate high levels of inaccuracy. Smaller mesh sizes although increase the accuracy, but their benefit is outweighed by the added amount of computational resource requirements.
- A very fine mesh quality is required in the near wall regions as well as near the axis to account for the thin boundary layer associated with the high velocity (supersonic) flow of a low viscosity fluid (natural gas, or air in some cases). Further discussion regarding the thickness of the boundary layers is presented in Section 4.1.2.
- It is highly recommended that a meshing scheme such as the one used for boundary layers be used along the axis of the nozzle to account for extreme tangential velocity gradients in that region. This is of utmost importance when the geometry is being modeled as an axis-symmetric two dimensional surface.

#### 5.1.2. Boundary Layer Thickness

Boundary layer is a thin film of fluid in the immediate vicinity of a solid surface. As the no slip condition implies, the fluid adjacent to the surface will not move (has a velocity of zero) whereas the fluid bulk is streaming at a certain velocity. Boundary layer is a transition sector in which velocity gradient is very high. It is because of this high gradient

that boundary layers require a finer mesh than the rest of the fluid bulk in a CFD analysis. The thickness of the boundary layer is a function of the fluid viscosity, bulk velocity of the fluid, geometry of the flow channel, and turbulence characteristics of the flow. It should be noted that knowing the correct thickness of the boundary layer is very important in designing a meshing scheme for a CFD analysis. If the assumed thickness of the boundary layer is larger than that of the real one, the simulated flow will not provide an accurate prediction of the flow because it will incorrectly predict a larger boundary layer. On the other hand, if the assumed boundary layer is thinner than the real one, the simulation will provide accurate results; but it will require unnecessary extra computational resources to do so. It is therefore important to know the correct thickness of the boundary layer when designing a meshing scheme. In order to achieve this goal, a sample meshing scheme was created using the methods described above. This scheme used 10% of the radius of the device at each section for boundary layer. This geometry was then scaled down by fractions ranging from 1 down to 0.00001. Ten different sizes of the same concept with the same meshing scheme were obtained. All these models were subjected to similar boundary and operating conditions. The results were then analyzed to determine to correct value of the boundary layer thickness. Figure 5.1 shows a graph of velocity magnitude as a function of normalized radial position for a few of these models. It can be seen that the boundary layer is thinner than the one element adjacent to the wall surface for models with a radius larger than 0.002 m. Models smaller than 0.002 m in diameter on the other hand show the boundary layer more clearly and it can be assumed that they correspond to the correct boundary layer thicknesses. The thickness of the

boundary layer can be calculated from this graph by multiplying the normalized percentage of the starting position of the boundary layer by the total radius of the corresponding radius. The boundary layer thicknesses of these models are presented in Table 5.1.

Table 5.1 The boundary layer thicknesses of the scaled nozzle models.

Radius (m)	Boundary Layer Normalized Thickness (% Total Radius)	Boundary Layer Thickness (m)
20	< 0.5	< 0.1
2	< 0.5	< 0.01
0.2	< 0.5	< 0.001
0.02	1	$2 \times 10^{-4}$
0.002	3	$6 \times 10^{-5}$
0.001	3	$3 \times 10^{-5}$
0.0005	4	$2 \times 10^{-5}$
0.0002	5	$1 \times 10^{-5}$

Boundary layers are specific to flow fields. This means that the larger the bulk velocity of the fluid is, the thinner the boundary layer becomes. It is predicted that the boundary layer associated with the swirl velocity is larger since the bulk swirl velocity is smaller than the axial one. Figure 5.2 shows a graph of normalized velocities as a function of radial position in a model with a radius of 1 mm and an initial swirl ratio of 1.00. It is

observed that the boundary layer associated with the axial velocity has a thickness of  $1.65 \times 10^{-5}$  (m) where as the boundary layer associated with the swirl velocity has a thickness of  $4.74 \times 10^{-5}$  (m). The graphs of the velocity profiles are separately presented in Figures 5.3 and 5.4 for comparison.

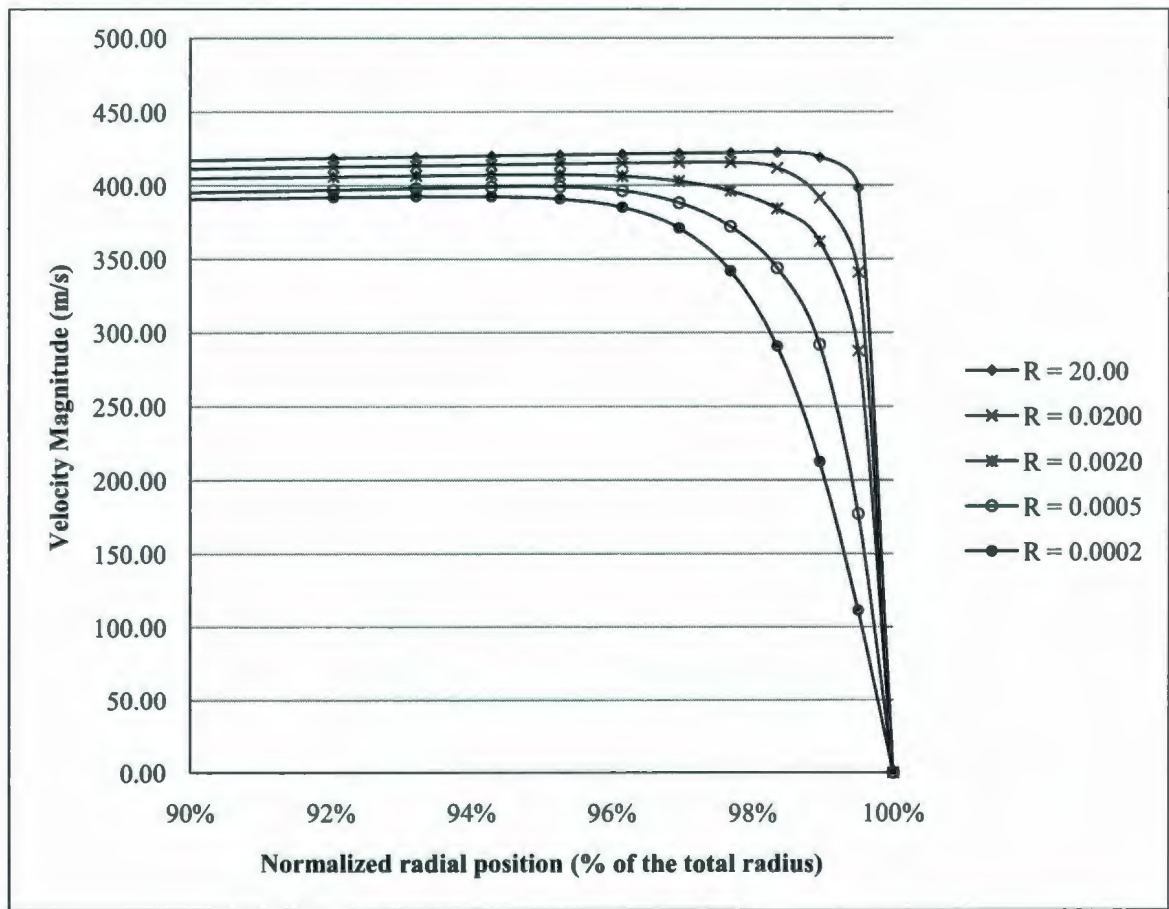


Figure 5.1 Velocity magnitude profiles at the throat of the same nozzle configuration with 5 different scales. Horizontal axis represents a percentile radial position.

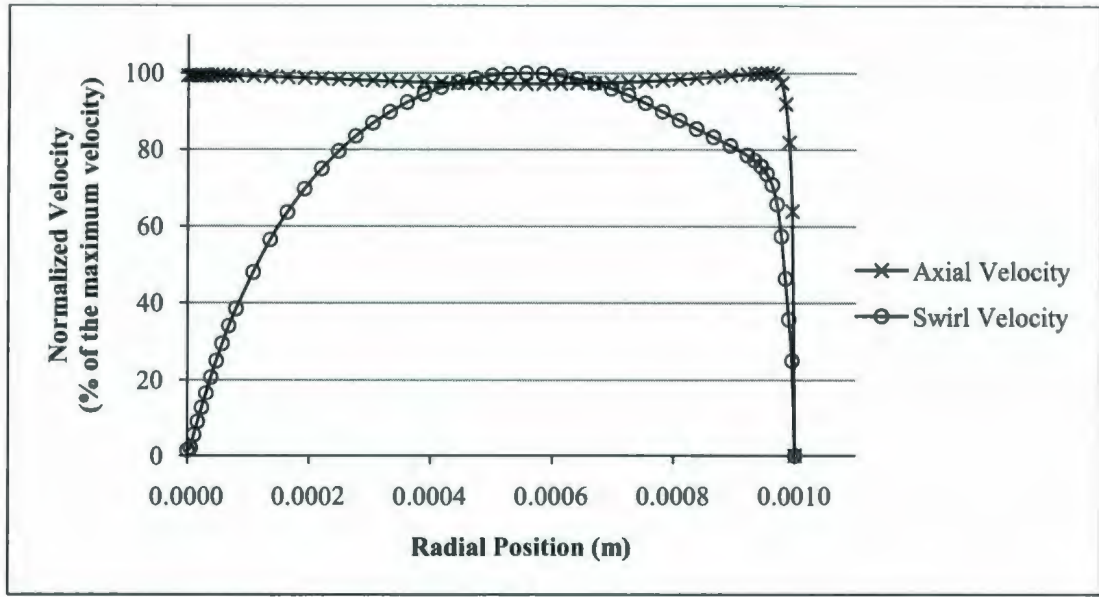


Figure 5.2 Comparison of swirl velocity and axial velocity profiles used to compare corresponding boundary layer thicknesses.

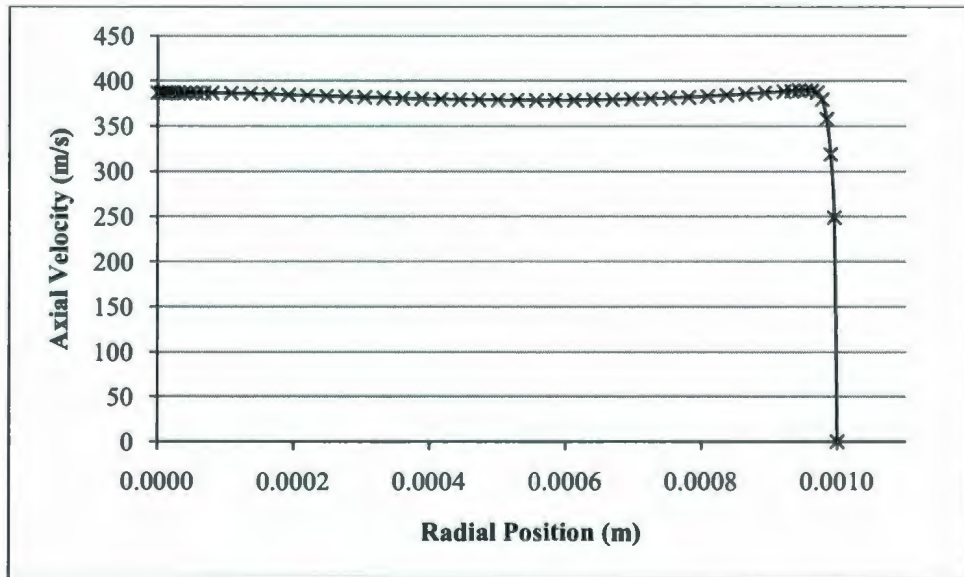


Figure 5.3 Axial velocity profile at the throat of a nozzle.

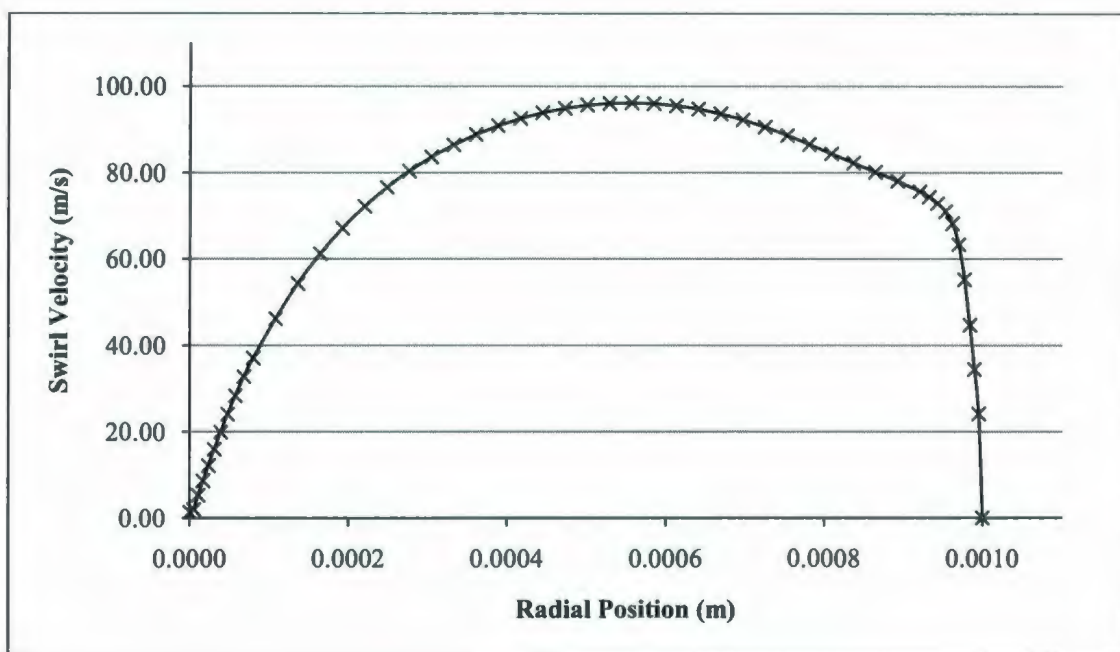


Figure 5.4 Swirl velocity profile at the throat of a nozzle.

### 5.1.3. Sensitivity Analysis

The effects of different variables on the performance of a supersonic separator with straight nozzle and swirling flow are discussed in this section. The direct effects of each variable are presented in separate subsections and overall conclusions are offered at the end of this section. The geometry of the nozzle systems discussed in this section was defined in Section 3.2.1 and by Equations 4.1 and 4.2. It should be noted that different nozzle sizes were studied in various aspects, which are not directly presented in this thesis. Most of the data provided here correspond to the geometry shown in Figure 4.1 the dimensions of which are presented in Table 5.2:

Table 5.2 The dimensions of the nozzle geometry used in the discussions

Inlet diameter:	0.0254 (1 in)
Outlet diameter:	0.0254 (1 in)
Throat diameter:	0.01016 m (0.4 in)
Axial position of the throat:	0.0254 m (1 in)
Total length of the nozzle and diffuser:	0.254 m (10 in)
Area of the inlet:	$5.07 \times 10^{-4} \text{ m}^2$
Area on the throat	$8.11 \times 10^{-5} \text{ m}^2$

#### 5.1.3.1. Inlet Pressure

The pressure of the gas at the inlet of the nozzle is one of the most important factors in the performance of the supersonic separator. This is due to the fact that most of the properties of the flow of the gas through the nozzle are determined by this pressure, among which are the properties such as mass flow rate, maximum velocity, and position of the shockwave. It should be noted that the inlet pressure is not the only variable that determines these properties. Other factors such as outlet back pressure and throat diameter are also important and will be discussed in later sections.

The mass flow rate of a gas through a supersonic nozzle is a direct function of the inlet flow pressure. It is this flow rate that determines the overall separation capacity of the device. The flow rate of a compressible fluid through a Laval nozzle reaches its maximum when the flow becomes sonic at the throat. This maximum is a function of the pressure and temperature of the fluid at the throat, which are in turn functions of pressure and temperature at the inlet. For an ideal gas the relationship could be defined as follows:

$$u_{throat} = c = \sqrt{\frac{\gamma RT_{th}}{M}} \quad (5.1)$$

$$\rho_{th} = \frac{P_{th}M}{RT_{th}} \quad (5.2)$$

$$\dot{m} = \rho u A \quad (5.3)$$

$$T_{th} = T_{in} \left( \frac{2}{\gamma + 1} \right) \quad (5.4)$$

$$P_{th} = P_{in} \left( \frac{2}{\gamma + 1} \right)^{\left( \frac{\gamma}{\gamma - 1} \right)} \quad (5.5)$$

Mass flow rate therefore is:

$$\dot{m} = A \left( \frac{2}{\gamma + 1} \right)^{\left( \frac{\gamma + 1}{2(\gamma - 1)} \right)} P_{in} \sqrt{\frac{\gamma M}{RT_{in}}} \quad (5.6)$$

The results gathered from the simulations also show that mass flow rate is linearly proportional to the pressure of the gas at the inlet. These results are presented in Table 5.3 and Figure 5.5. It should be noted that these results are prepared only for comparison with the theoretical analogy using ideal gas assumption. Real gas properties were used for more detailed simulations.

Table 5.3 Mass flow rate values for different gas inlet pressures.

Inlet Pressure (kPa)	Mass Flow Rate (kg/hr)
206.8	4.04
227.5	4.45
241.3	4.71
255.1	4.97
275.8	5.39
289.6	5.66
317.2	6.20
324.1	6.33
330.9	6.47
337.8	6.60
344.7	6.74

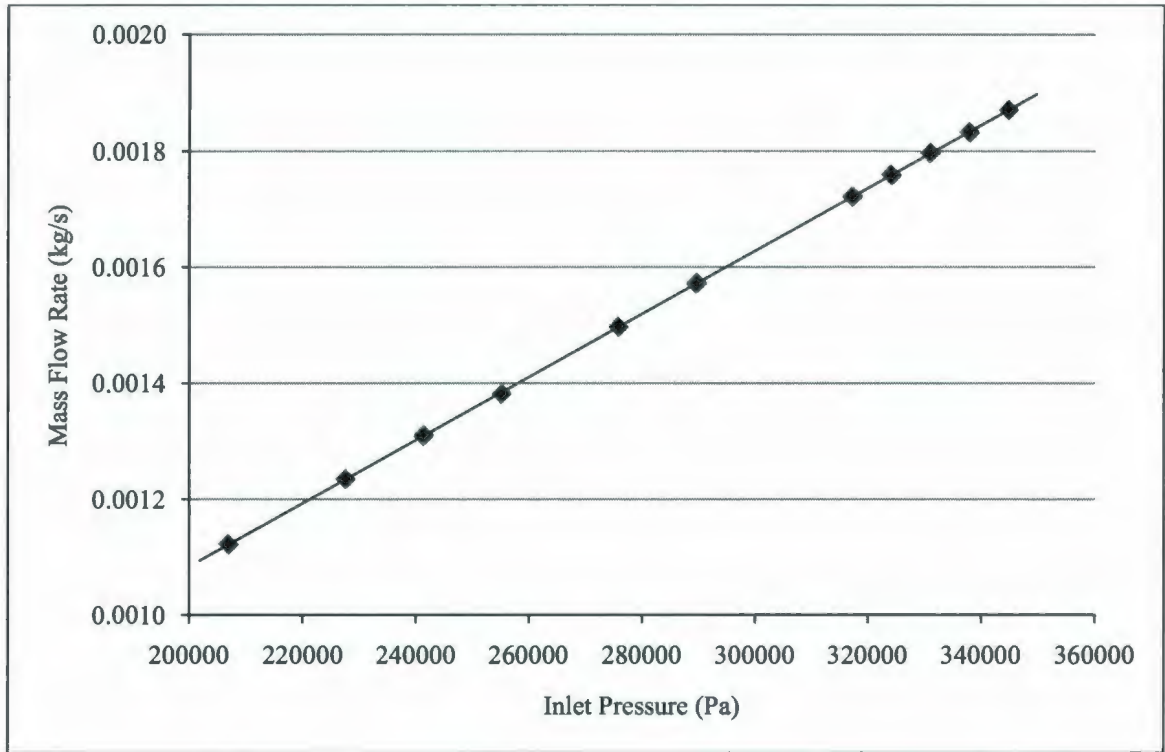


Figure 5.5 Mass flow rate versus inlet pressure for an ideal gas. The flow is choked for all pressures.

Maximum velocity of the gas and position of the shockwave are both direct functions of the pressure difference between the two sides of the nozzle, or *pressure driving force* as it will be referred to in this thesis. As the role of the outlet back pressure is discussed in a separate section, the effects of the pressure driving force will be discussed here only as a function of inlet pressure, hence assuming the outlet pressure to be constant.

It is known that the following equation describes the relationship between cross-sectional area of the nozzle and the velocity of the ideal gas flowing through it (Kundu 2008).

$$(1 - Ma^2) \frac{du}{u} = -\frac{dA}{A} \quad 5.7$$

It is clear that while the flow is supersonic, that is when  $Ma > 1$ , the velocity increases as the gas flows further into the diverging section of the nozzle. The extreme that this velocity will increase to, depends on the pressure driving force that exists throughout the nozzle. Therefore it can be concluded that the maximum velocity of the gas increases and the position of the shockwave moves further away from the throat as the inlet pressure is increased. This behaviour is also observed in the results of our CFD simulations. Figures 5.6 to 5.9 show the results of CFD simulations supporting these predictions. Figure 5.6 is a presentation of the maximum velocities achieved by the gas through the nozzle as a function of inlet pressure. It can be seen that as the inlet pressure is increased and the outlet back pressure is kept unchanged at 101 kPa (1 atm), the maximum velocity achieved by the gas increases. Figure 5.7 shows how the position of the shockwave is changed as the inlet pressure is increased. It is observed that the shockwave appears further away from the throat and closer to the exit as the inlet pressure is increased, hence providing a longer separation section which may lead to better separation ratio. Figures 5.8 and 5.9 show the velocity profiles and Mach number profiles along the axis of the nozzle as the inlet pressure is increased and confirm the previous observations.

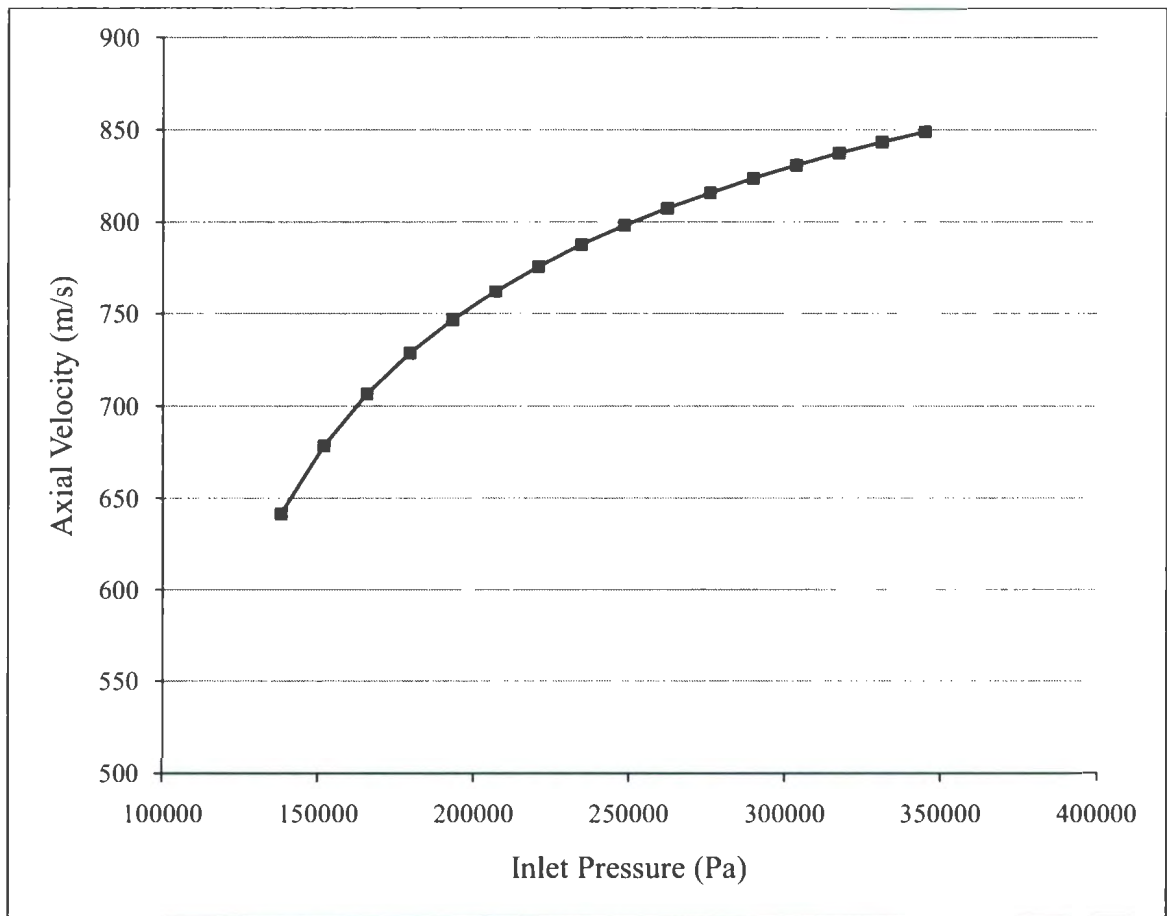


Figure 5.6 The maximum axial velocity achieved in a typical nozzle with different inlet pressures. The outlet back pressure is 101kPa (1 atm) in all cases.

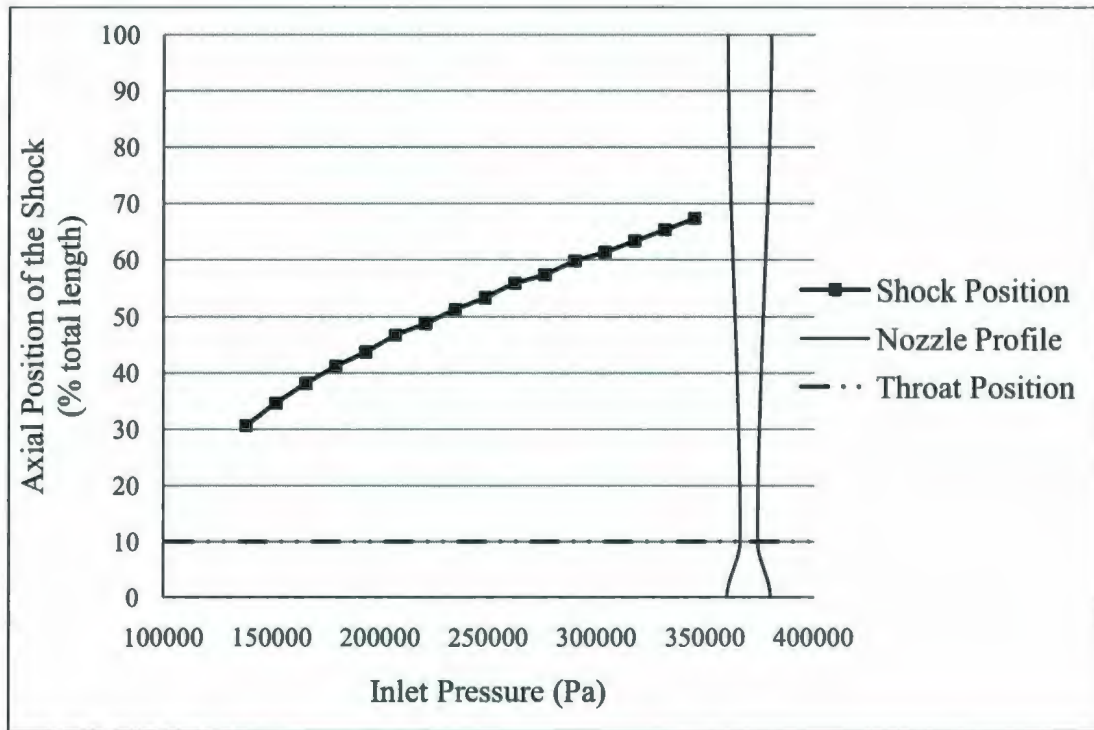


Figure 5.7 The position of the shockwave moves further away from the throat as the inlet pressure is increased.

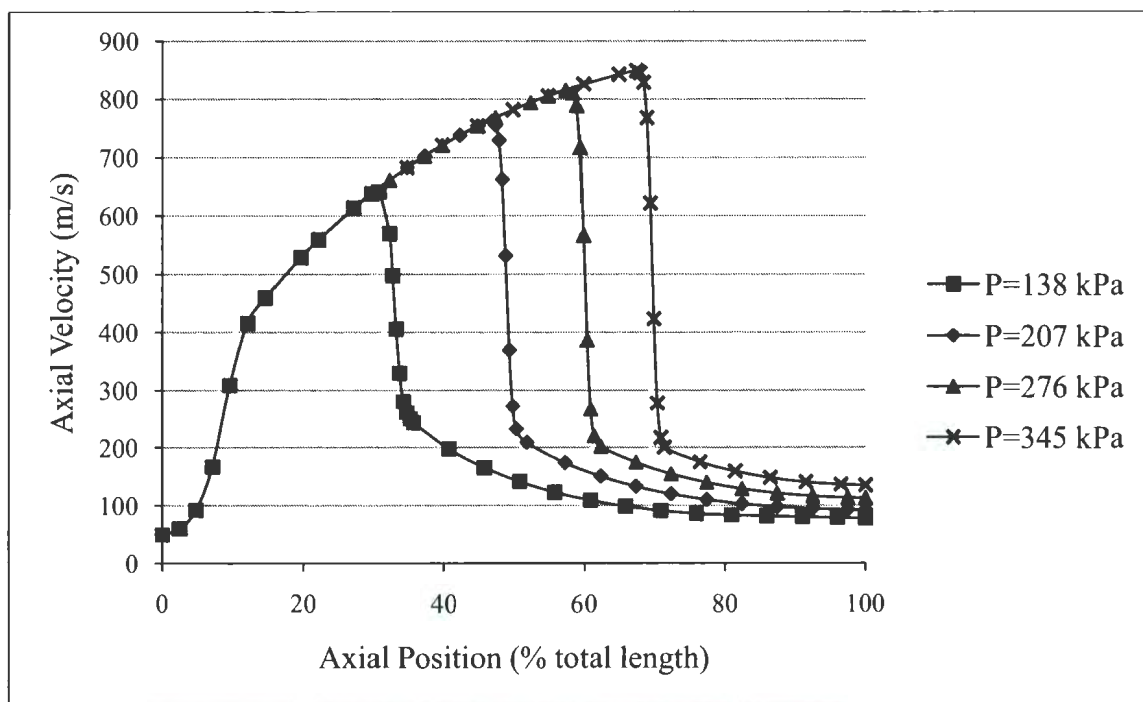


Figure 5.8 Axial velocity profiles along the axis of the nozzle for inlet pressures ranging from 135 kPa up to 345 kPa. Outlet back pressure is constant at 101 kPa (1 atm).

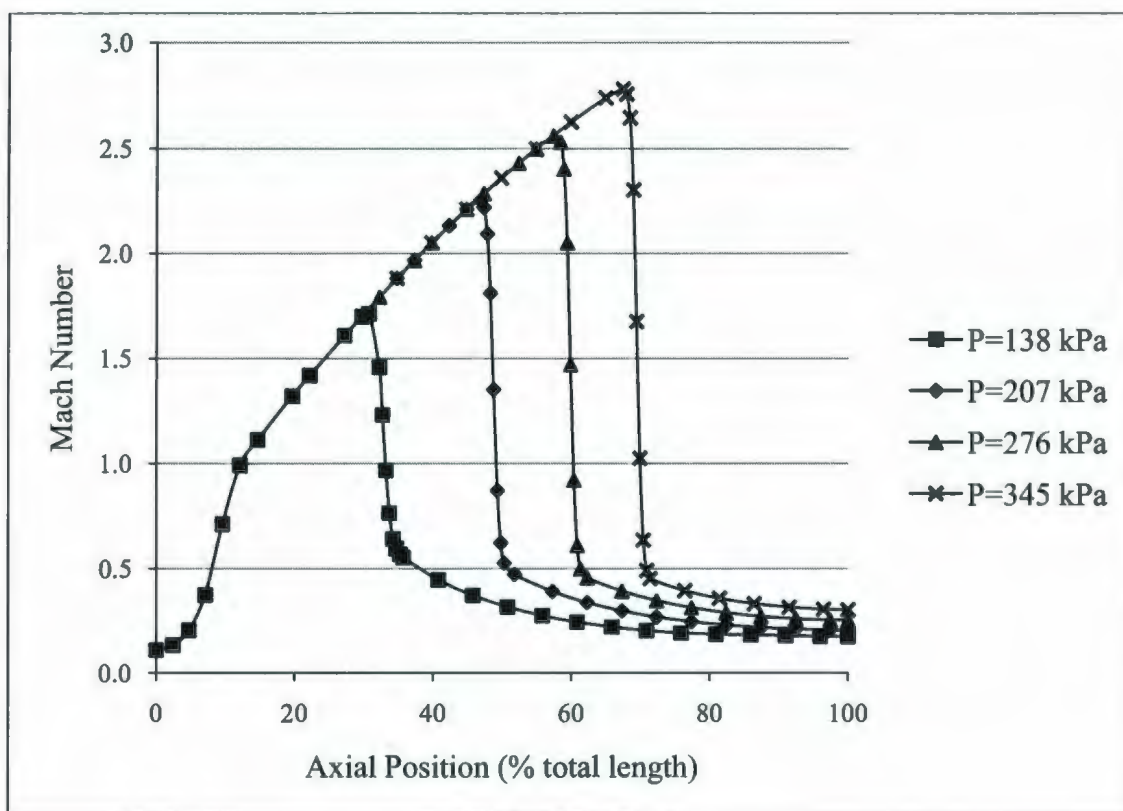


Figure 5.9 Mach number values along the axis of the nozzle. Inlet pressure varies between 135 kPa and 345 kPa and outlet back pressure is constant at 101 kPa (1 atm).

### 5.1.3.2. Inlet Swirl Intensity

It was explained in the previous sections that the desired separation of phases in swirl-type supersonic separators is achieved by the centrifugal acceleration acting on the particles as a result of the swirling motion of the fluid mixture through the nozzle. Inherently, the intensity of this swirling motion is an imperative factor in the performance of the separator. It can be further explained that it is the intensity of the swirl at the inlet

flow that ultimately governs the fluid's swirl profile since there are no other means to adjust this intensity along the nozzle. The effects of the inlet swirl intensity are discussed in the remainder of this section.

The first challenge in analyzing the effects of the flow swirl intensity on the performance of the separator is the measurement of the swirl intensity itself. There are several methods to incorporate this intensity in different variables. A few of these variables used in this study are briefly explained below (Fluent 6.3 User's Guide, Chapter 9.5).

**Swirl velocity ratio:** This is a dimensionless number that can be used to express the relative value of swirl velocity to the linear (axial) velocity. This variable is represented by the Greek letter  $\zeta$  (zeta) in this study and is defines as:

$$\zeta = \frac{V_{\text{tangential}}}{V_{\text{axial}}} \quad (5.8)$$

$V_{\text{tangential}}$  and  $V_{\text{axial}}$  are the tangential and axial components of the velocity vector respectively.

**Swirl intensity:** Swirl intensity is taken to be the area-weighted average of tangential velocity at any particular cross section of the nozzle. The mathematical definition of this term is:

$$S = \frac{\int V_{\text{tangential}} dA}{A} \quad (5.9)$$

$S$  is the swirl intensity and  $A$  is the area of the cross section  $S$  is being measured over.

**Centrifugal acceleration:** Centrifugal acceleration is the result of the radially outward force an object experiences as it travels in a circular path. This force is proportional to the angular velocity and to the radial distance from the centre of rotation:

$$a_c = \omega^2 r = \frac{V_{\text{tangential}}^2}{r} \quad (5.10)$$

$$V_{\text{tangential}} = \omega \times r \quad (5.11)$$

$$a_c = \frac{V_{\text{tangential}}^2}{r} \quad (5.12)$$

Where  $a_c$  is the centrifugal acceleration,  $\omega$  is the angular velocity, and  $r$  is the radius or the distance from the centre of rotation. In another point of view, if the centrifugal acceleration is correlated with tangential velocity (Equation 5.11) instead of angular velocity, it can be seen that the acceleration is proportional to the inverse of the radius (see Equation 5.12). This is the approach utilized in this study.

**Area-Weighted Average Centrifugal Acceleration:** The above explained centrifugal acceleration is indeed a fairly reliable form of assessing the separation process. Data collection for this variable can be somewhat difficult. This is due to the existence of two boundary layers for a swirling fluid. The first boundary layer is the one that appears in the interface of any fluid with a solid surface which in this case, is the wall boundaries.

The second and more sophisticated boundary layer emerges in the axis of rotation of a swirling fluid which leads to a mathematical discontinuity of the tangential velocity profile at the location of the axis. It is because of these complexities that an area-weighted average of the centrifugal acceleration is used instead of its local value where it is possible. The Greek letter  $\psi$  (Psi) is taken to represent the area-weighted average centrifugal acceleration and is defined as:

$$\psi = \frac{\int a_c dA}{A} \quad (5.13)$$

**Discussion regarding the inlet swirl intensity:**

It is evident that the higher the tangential velocity is, the higher centrifugal acceleration will be (see Equation 5.12), which ultimately results in a higher rate of separation. However, there is also a converse effect; increasing the swirl intensity will also increase the energy loss along the nozzle. The negative impact of increased swirl intensity can be expressed in two ways: a) if the separator is set to work on a specific flow rate, the pressure loss along the device will increase, and b) if the separator is set to operate on a fixed inlet pressure, the flow rate will drop. These theories are supported by the results of the CFD simulations shown in Figure 5.11.

Figure 5.10 shows the values of swirl intensity along the nozzle for different initial swirl velocity ratios. It can be seen that increasing the initial swirl velocity ratio has significant effects on the swirl intensity profile up to the value of  $\zeta_0 = 2.50$ , where  $\zeta_0$  is defined by

Equation 5.8. Above this value, although the swirl intensity profile does increase with  $\zeta_0$ , the effect is not as significant and may outgrow its benefits. Figure 5.11 shows a plot of mass flow rate capacity of the nozzle for a constant inlet pressure of 345 kPa as a function of initial swirl ratio. It can be seen that the flow rate decreases with increasing initial swirl velocity ratio. Moreover, this decrease reaches a maximum rate around  $\zeta_0 = 1.25$  which can be seen more clearly in Figure 5.12. These values may be taken as guidelines for design purposes. Figure 5.13 shows the area-weighted average centrifugal acceleration along the nozzle. It is noticeable that the centrifugal acceleration becomes negligible in the last twenty percent of the length of the nozzle (the nozzle profile is schematically shown for visual aid). It is recommended that the system is designed in a way that the required separation is achieved before this point and the remainder of the nozzle is left for pressure recovery and stabilization of the flow. The position along the nozzle where a vortex finder is to be placed to separate the flow of denser particles from the main flow depends on this design feature (the axial position where the minimum required separation is achieved) as well as the position of the shockwave. Evidently, the vortex finder should be placed somewhere before the shock takes place or the occurrence of the shock will disperse the centrifugally separated particles into the gas flow.

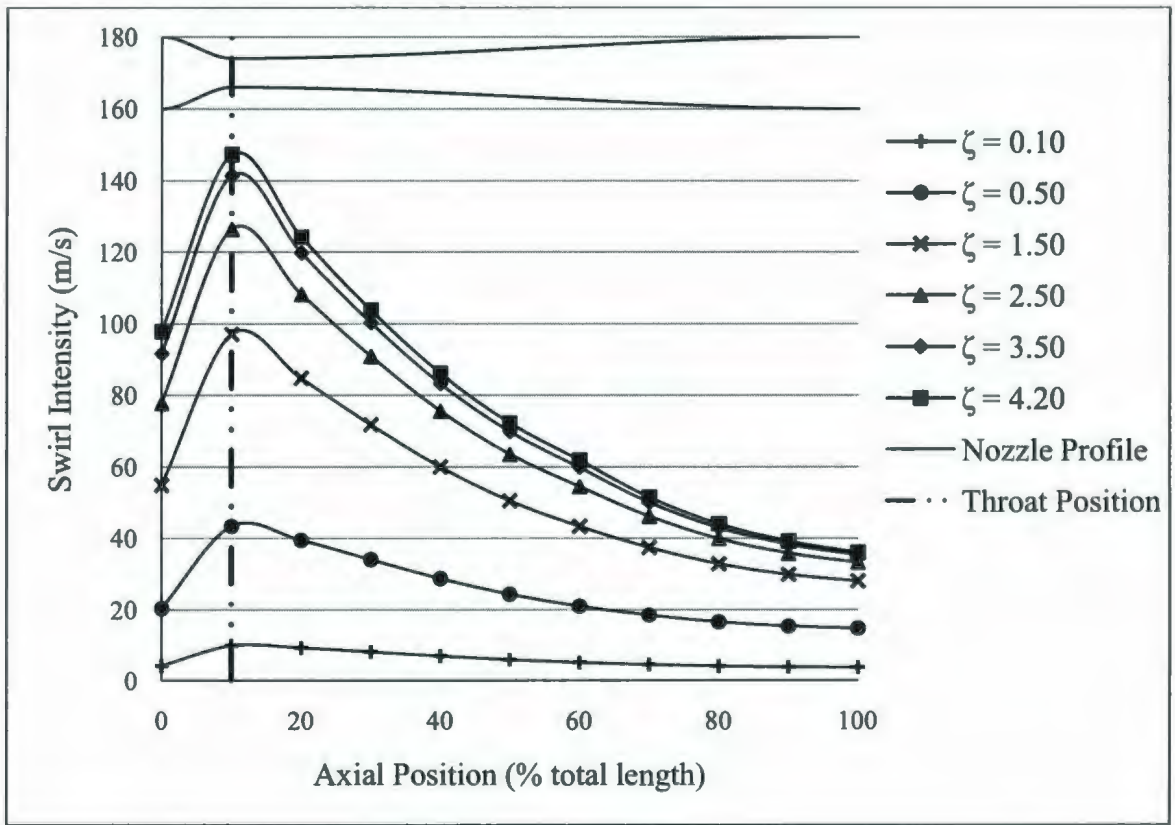


Figure 5.10 Area-weighted average tangential velocity (swirl intensity) plotted against axial position along the nozzle for various initial swirl velocity ratios ( $\zeta_0$ ).

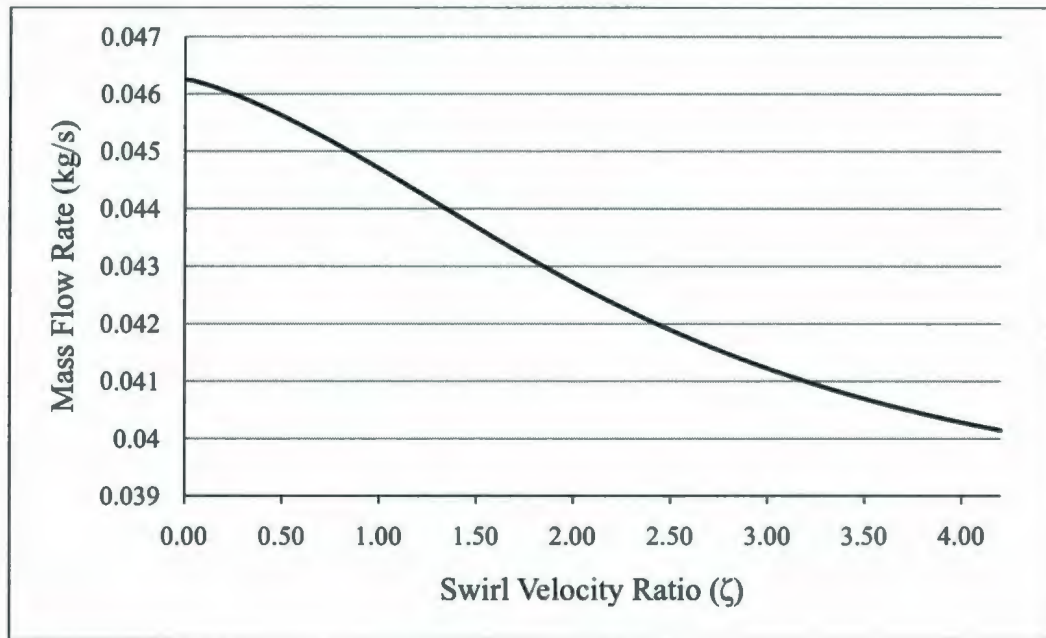


Figure 5.11 Mass flow rate through the nozzle as a function of initial swirl velocity ratio. The nozzle is set to operate at a constant inlet pressure of 345 kPa.

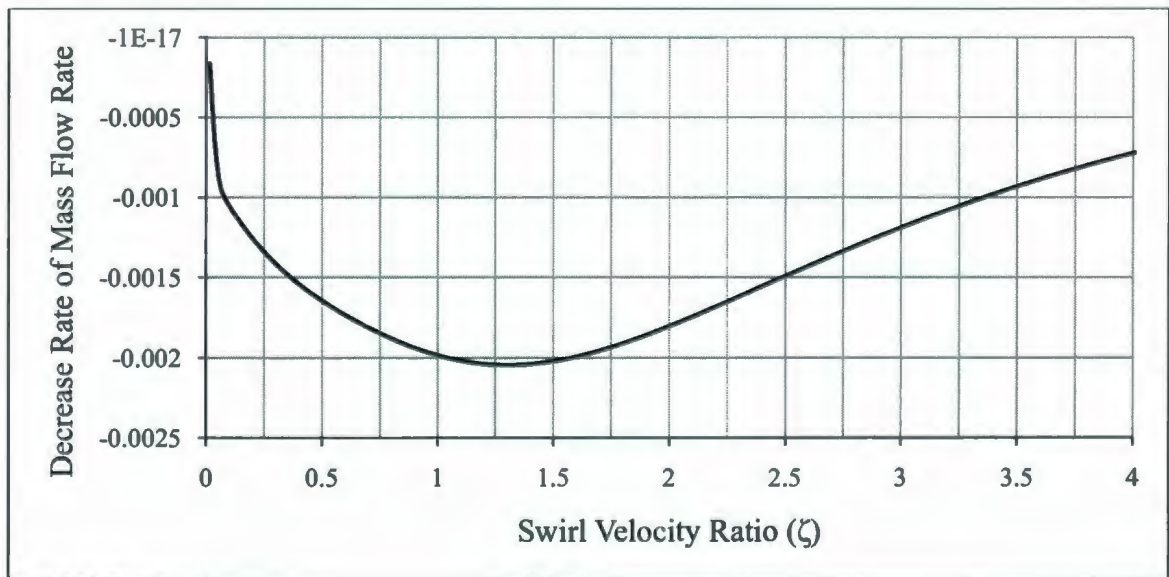


Figure 5.12 The rate of change of mass flow rate with respect to swirl velocity ratio.

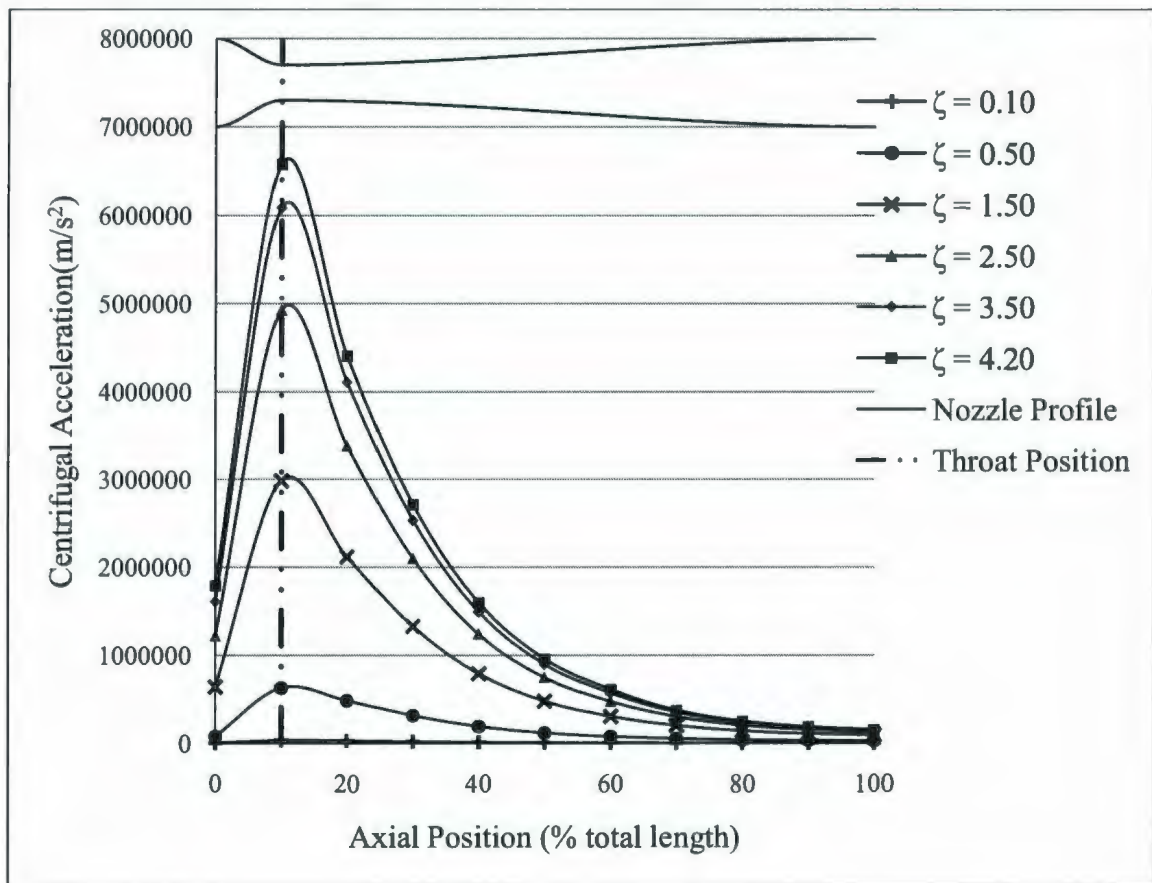


Figure 5.13 Variation of centrifugal acceleration along the nozzle. Area-weighted average values of centrifugal acceleration are plotted against axial position along the nozzle for various initial swirl velocity ratios ( $\zeta_0$ ).

### 5.1.3.3. Throat Diameter

Throat diameter is a factor in determining a key property in a supersonic nozzle, namely the gas flow rate through the nozzle. As it was mentioned previously, the mass flow rate of the ideal gas can be related to the throat diameter by the following equation:

$$\dot{m} = A \left( \frac{2}{\gamma + 1} \right)^{\frac{\gamma + 1}{2(\gamma - 1)}} P_{in} \sqrt{\frac{\gamma M}{RT_{in}}} \quad (4.6)$$

It can be seen that mass flow rate is directly proportional to the cross sectional area of the nozzle's throat. This is a conclusion that was also obtained by the CFD simulations results. Figure 5.14 shows the results of the CFD simulations for 16 different nozzle designs that are different with each other only in throat diameter. The linear relationship between flow rate and throat area is shown by a trend-line extrapolated to show the axis intercept at 0 kg/s for a cross section area of 0 m<sup>2</sup>. The equation of the trend-line is also shown on the graph which confirms the negligible value of the y-intercept. Moreover, the slope of the trend-line maybe compared with the theoretical value obtained from Equation 5.6. Using the following data that correspond to the simulation conditions, the theoretical value of the trend-line is found to be 643.5 and in agreement with the CFD produced results with less than 0.03% error.

For air as process fluid:

$$\gamma_{\text{air}} = 1.4$$

$$M = 28.96 \times 10^{-3} \text{ kg/mol}$$

$$R = 8.314 \text{ kg/mol.K}$$

And with operating conditions of:

$$T_{\text{in}} = 300\text{K}$$

$$P_{\text{in}} = 275790\text{Pa (40 psi)}$$

$$\dot{m} \left( \frac{\text{kg}}{\text{s}} \right) = A_{\text{th}} \left( \frac{2}{\gamma + 1} \right)^{\frac{\gamma + 1}{2(\gamma - 1)}} P_{\text{in}} \sqrt{\frac{\gamma M}{RT_{\text{in}}}} = 643.54 \times A_{\text{th}} \left( \text{m}^2 \right)$$

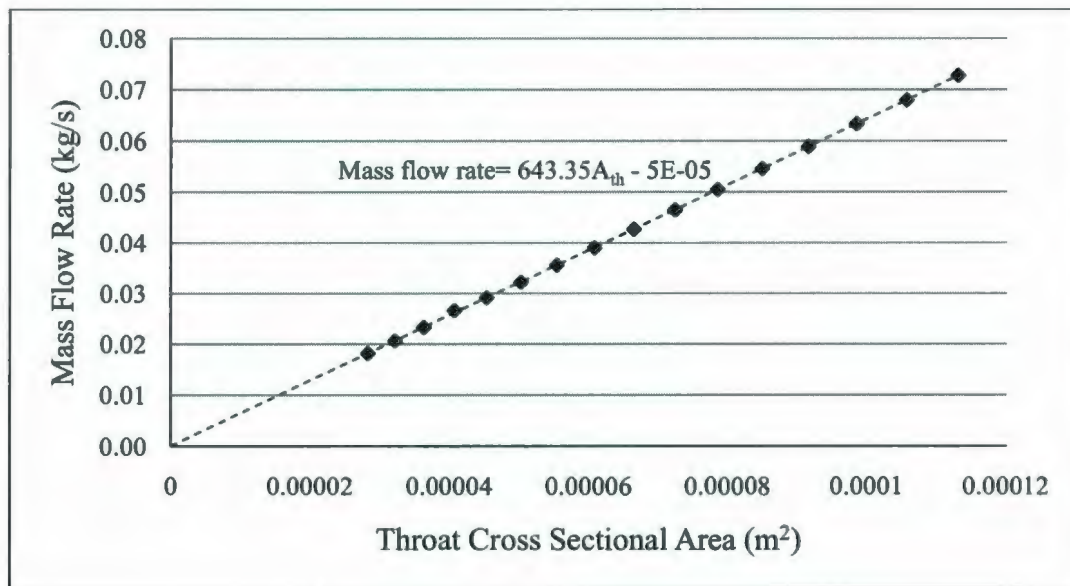


Figure 5.14 Mass flow rate of the gas through the nozzle with respect to throat cross sectional area. The flow rate is linearly correlated to the throat area.

#### 5.1.3.4. Outlet Back Pressure

The effects of outlet back pressure on the pressure driving force can be described as the reverse of those of the inlet pressure. In other words, raising the outlet pressure reduces the pressure driving force in the exact same way that decreasing the inlet pressure does. It can be shown that increasing the outlet back pressure at a constant inlet pressure reduces the maximum velocity of the gas in the nozzle and moves the shockwave closer to the throat. Figure 5.15 shows the static pressure profiles along the axis of a typical nozzle with different operating conditions. The inlet pressure is kept constant at 345 kPa (50 psia) where the outlet back pressure is changing from 303 kPa (44 psia) down to 138 kPa (20 psia). Static pressure is a term used in Fluent to represent pressure and to avoid confusion with total pressure which takes into account the effects of velocity head as well. The two are virtually the same unless the fluid is flowing transonically which is the case in this study. Figure 5.16 shows the Mach number profiles for the same nozzle and at the same operating conditions and Figure 5.17 is a graph of the position of the shockwave with respect to the changing outlet back pressure. It can be seen through all three figures that theoretical conclusions of maximum velocity and position of the shockwave are confirmed by the CFD simulations results.

The outlet back pressure is used more effectively in the form of pressure loss or pressure recovery ratios. The following are the definitions of these variables as used in this study:

Pressure Loss Ratio:

$$P_L = \frac{P_{out} - P_{in}}{P_{in}} \times 100\% \quad 5.14$$

Pressure Recovery Ratio:

$$P_r = \frac{P_{out}}{P_{in}} \times 100\% \quad 5.15$$

These parameters are used in conjunction with centrifugal acceleration inside the nozzle to determine the separation efficiency of the separators.

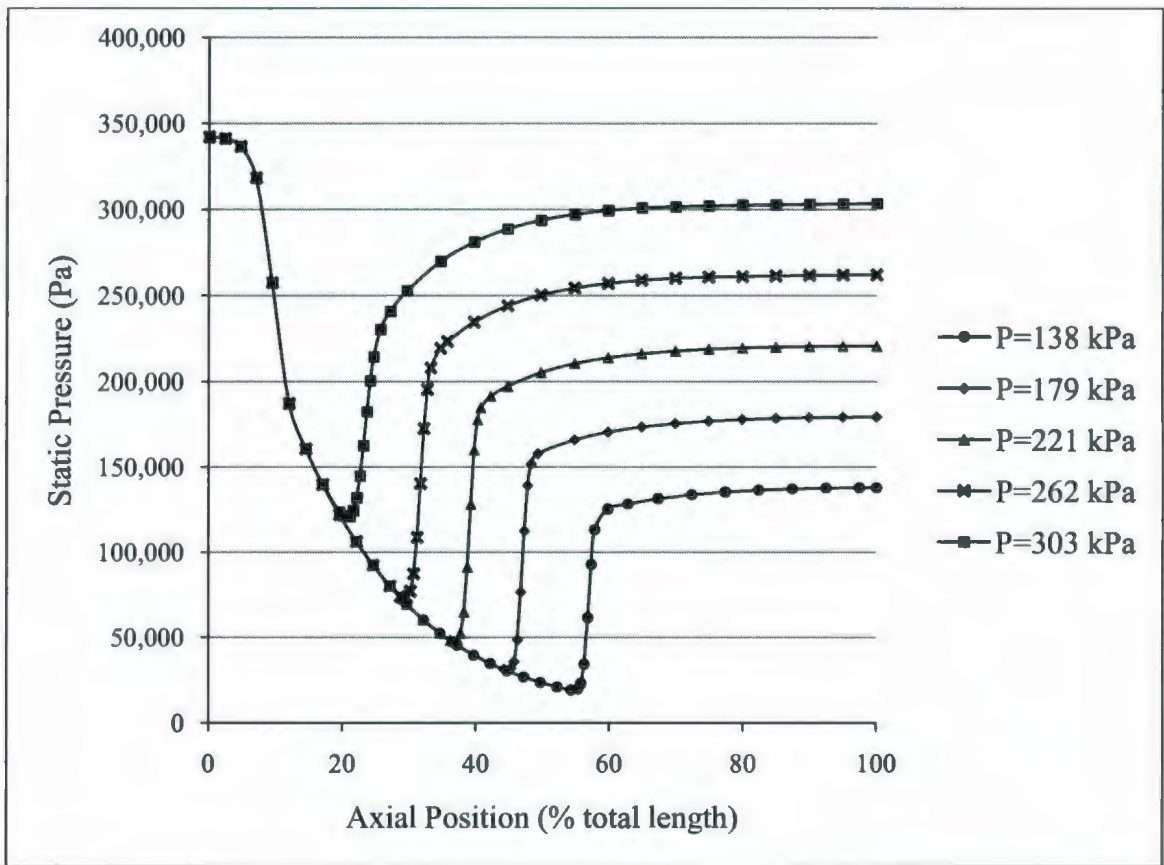


Figure 5.15 Static pressure along the axis of a typical nozzle with the outlet back pressure ranging from 303 kPa (44 psia) down to 138 kPa (20 psia). The inlet pressure is 345 kPa (50 psia) at all times.

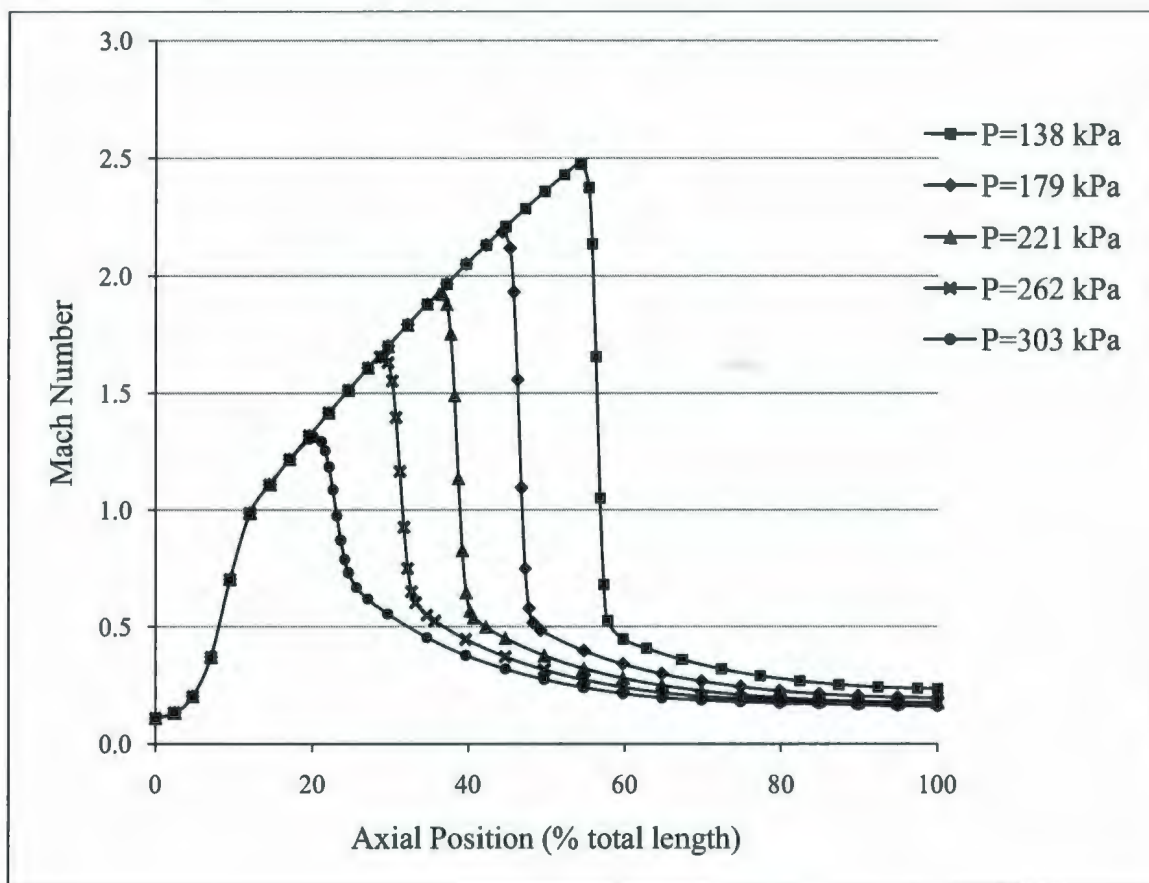


Figure 5.16 Mach number profiles along the axis of a typical nozzle with the outlet back pressure ranging from 303 kPa (44 psia) down to 138 kPa (20 psia). The inlet pressure is 345 kPa (50 psia) at all times.

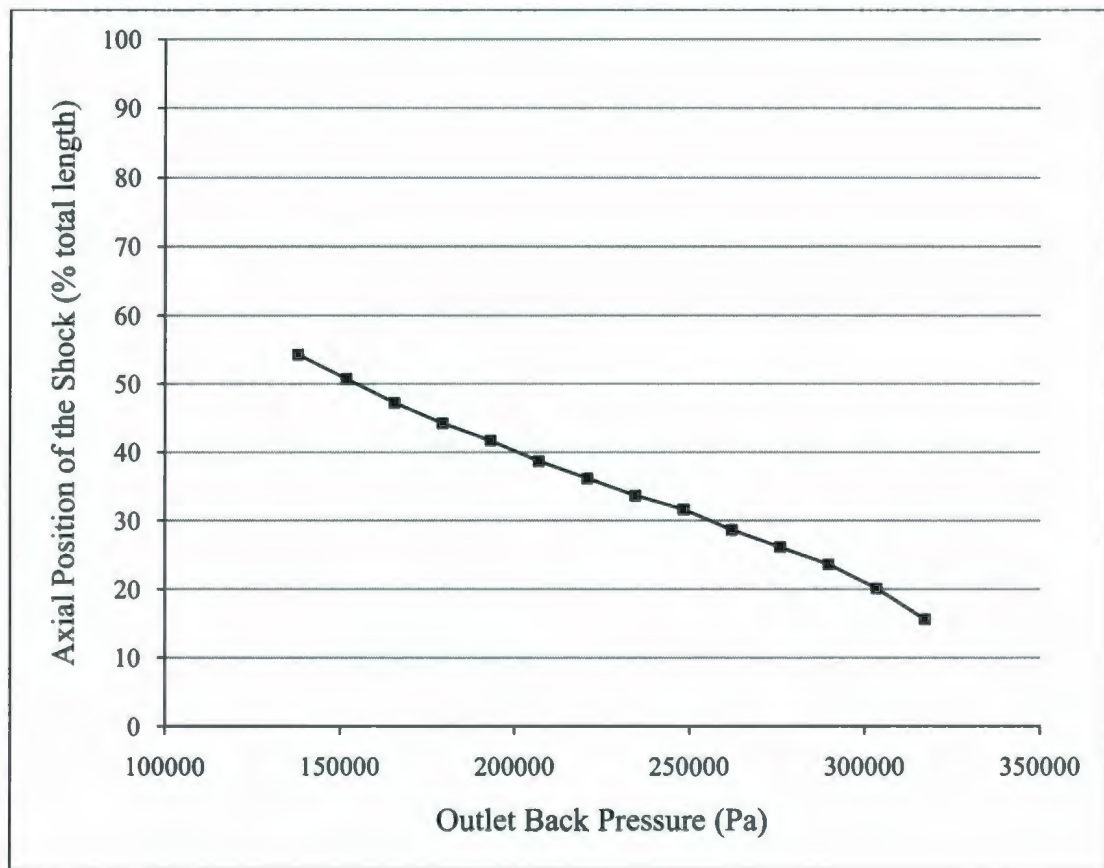


Figure 5.17 The axial position of the shockwave against the outlet back pressure. Note that the inlet pressure is 345 kPa for all cases.

## 5.2. U-SHAPED NOZZLE

The U-shaped nozzle is a novel alternative configuration to the supersonic separators proposed in this thesis. It is designed to take advantage of the centrifugal acceleration exerted on the flow mixture as it passes through a circular (U-shaped) path with supersonic velocity. The following is the results of the simulations and consequent discussions.

### 5.2.1. Meshing Scheme

The meshing scheme and strategy play important roles in the stability and accuracy of the numerical solution. The alternative concepts proposed in this section of the study are similar in geometrical properties to those of the original designs (straight nozzle) in that they also follow a converging-diverging course. However, they differ from the original designs in two key features that can potentially affect the meshing scheme. The first difference is the existence of the U-shaped section which requires specific diligence to the quality of the mesh. Secondly, the fact that the gas is no longer flowing in a swirling motion brings the advantage of being able to neglect the effects of boundary layers. Specific details of the meshing scheme may vary slightly from one concept to the other, but the overall design is the same and will be described in the following section.

The geometry used in this design is the concept that was also used in the test experiment. As outlined in Figure 5.18, the concept consisted of three sections:

1. The convergent subsonic section that experiences a slight divergence after the throat to accommodate the conditions promoting supersonic flow of the gas.
2. The U-shaped extended throat through which the centrifugal force exerted on the particles is expected to provide the intended separation between phases (gas-liquid, gas-solid, or gas-solid-liquid).
3. The divergent section that provides the cross-sectional growth required for pressure recovery.

The specifics of the proposed geometry are shown in Figure 5.19. The meshing scheme used to represent the proposed U-shaped nozzle is a combination of wedge shaped elements and tetrahedral elements. The geometry was divided into six sections as shown in Figure 5.20. All sections were meshed using wedge shaped elements except Section 2 which was meshed using tetrahedral elements due to the high gradient of cross-sectional area. Section 1 is only a simple pipe and its purpose is to stabilize the flow of gas before it enters the nozzle system. The meshing of this section therefore does not require a very fine quality. The mesh elements in this section are wedges with a length of  $5.08 \times 10^{-3}$  m (0.2 inch) and equilateral triangle bases with edges of  $2.54 \times 10^{-3}$  m (0.1 inch) (see Figure 5.21). Section 2 is the converging section of the nozzle and is meshed with a shrinking tetrahedral scheme (Figures 5.22 and 5.23). This method ensures the stability of the geometry through the numerical analysis and links the coarse mesh of Section 1 and the fine mesh of Section 3. Section 3 is the slight divergence downstream of the throat that accommodates the supersonic flow of the gas and hence requires a very fine mesh quality to ensure the accuracy of the results. The meshing scheme is again a wedge type element that grows laterally as the cross section increases. The meshes are arranged so that there are 60 elements on the cross sectional perimeter at each point. This means that the wedge bases have lateral sizes of  $1.016 \times 10^{-4}$  m (0.004 inch) in the beginning (right after the throat) and  $1.27 \times 10^{-4}$  m (0.005 inch) in the end (right before the U-shaped section). A length of  $2.54 \times 10^{-4}$  m (0.01 inch) is kept constant throughout this section. Section 4 is the U-shaped section. Wedge elements advance into this section with the same base sizes and lengths of  $5.08 \times 10^{-4}$  m (0.02 inch). The wedges grow in Section 5 until they reach a base

size of  $2.54 \times 10^{-3}$  m (0.1 inch) and length of  $5.08 \times 10^{-3}$  m (0.2 inch) at the end of this section to merge in with Section 6 that is the equivalent of Section 1. The mesh elements remain the same throughout this section. It is important to note that since the fluids being studied are gaseous and of high velocities, the effects of boundary layers may be neglected and hence no extra care is directed towards that area.

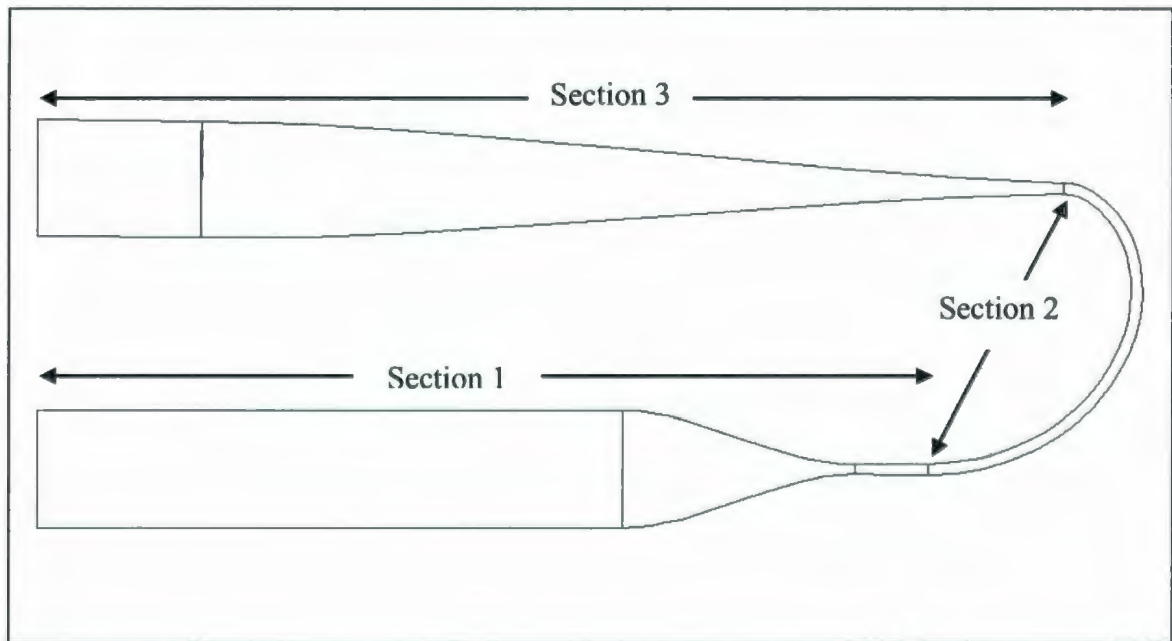


Figure 5.18 Cross-sectional view of the proposed geometry. Three sections of the device are marked.

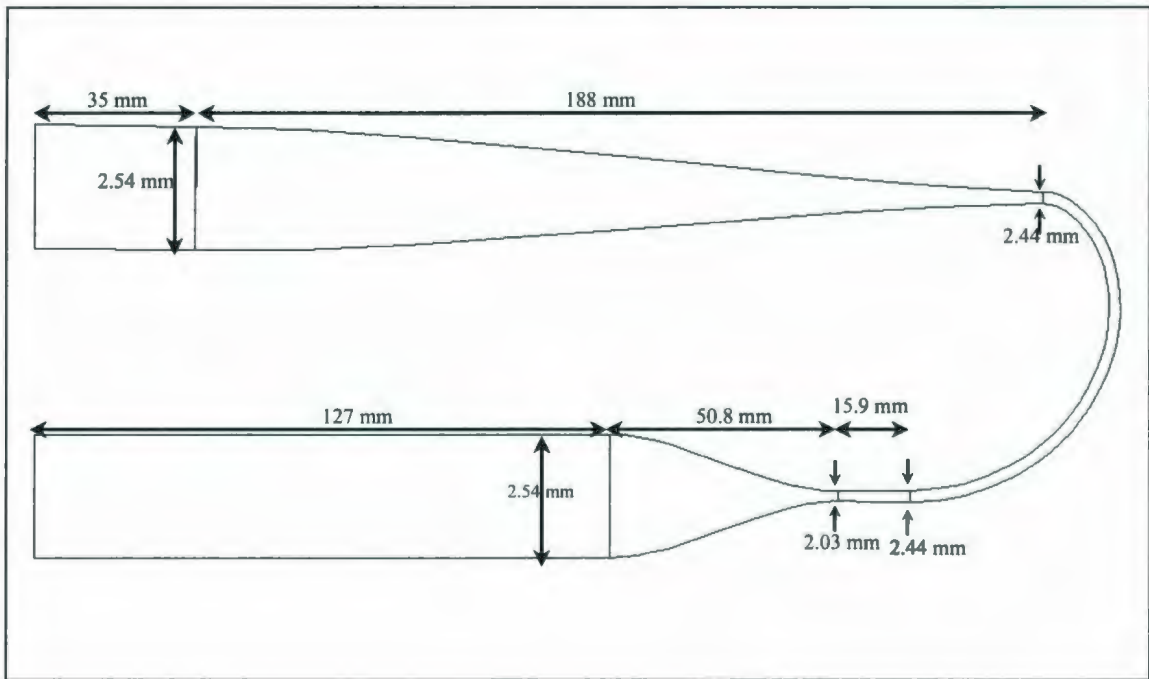


Figure 5.19 The dimensions of the proposed geometry.

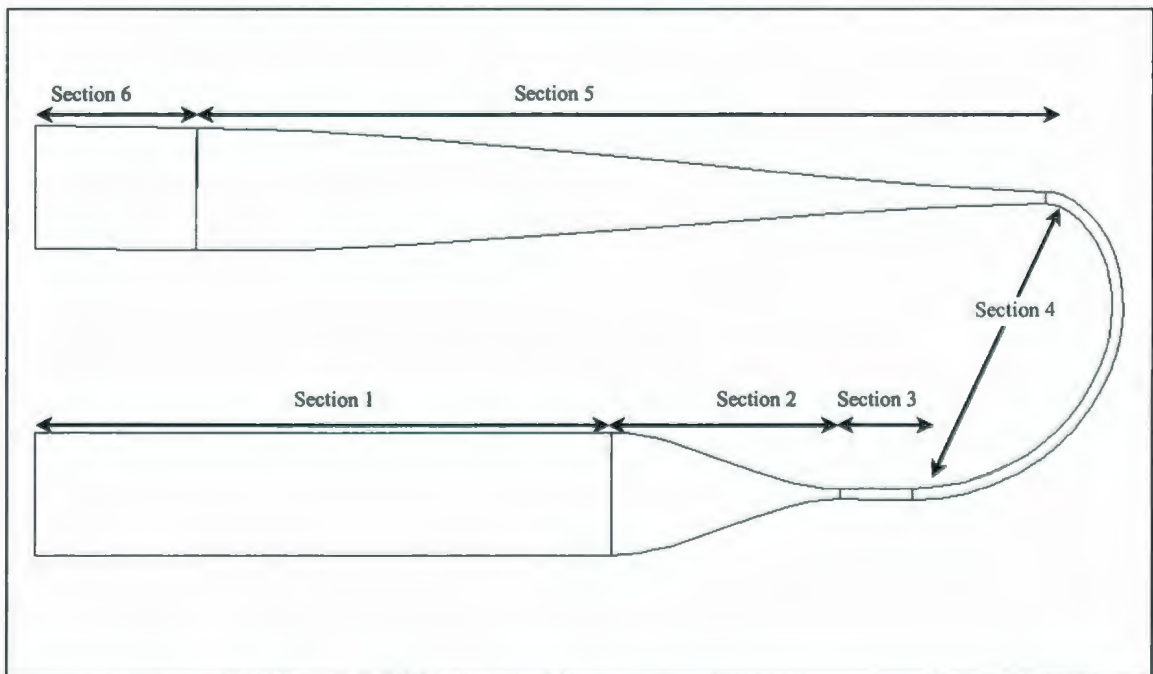


Figure 5.20 Six sections of the geometry used in the meshing scheme.

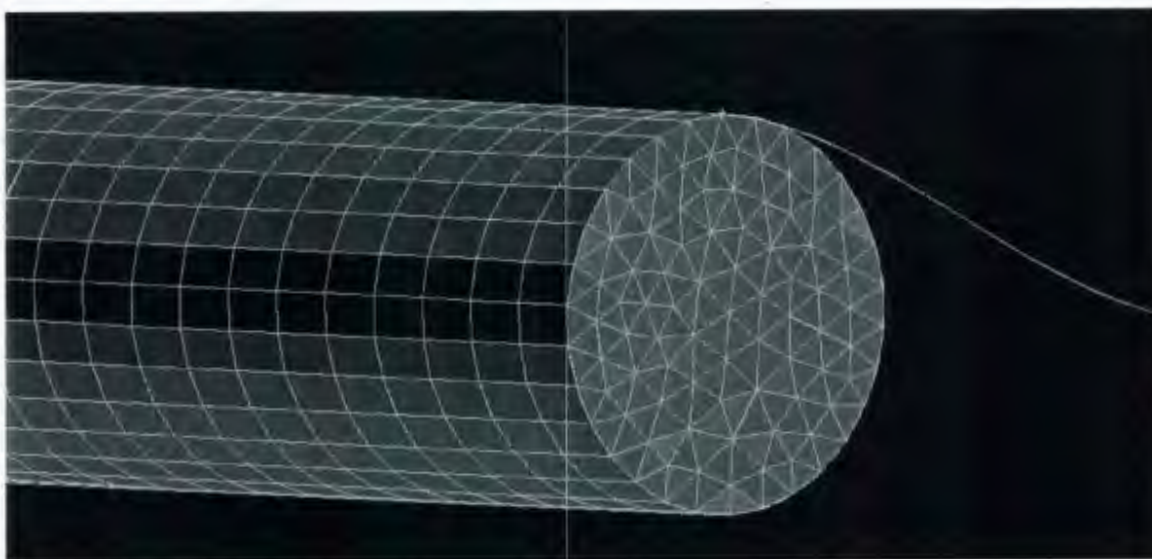


Figure 5.21 Wedge shaped mesh elements forming the inlet stabilizing section of the device (Section 1).

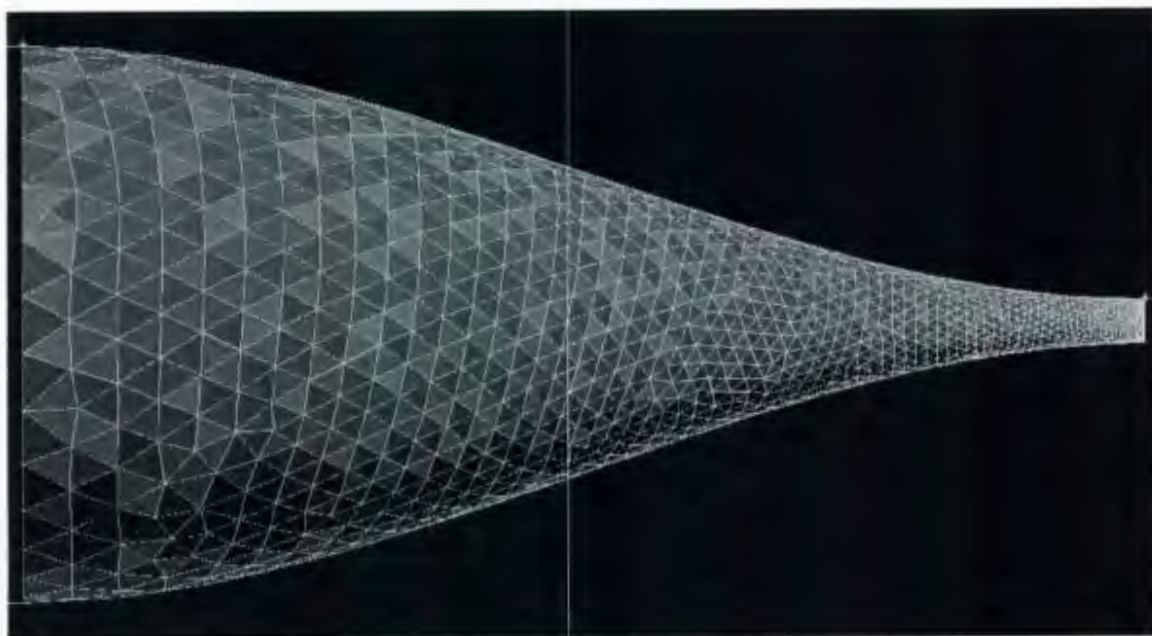


Figure 5.22 Tetrahedral mesh elements in the converging section of the nozzle (Section 2). The element volumes shrink as they get closer to the throat.

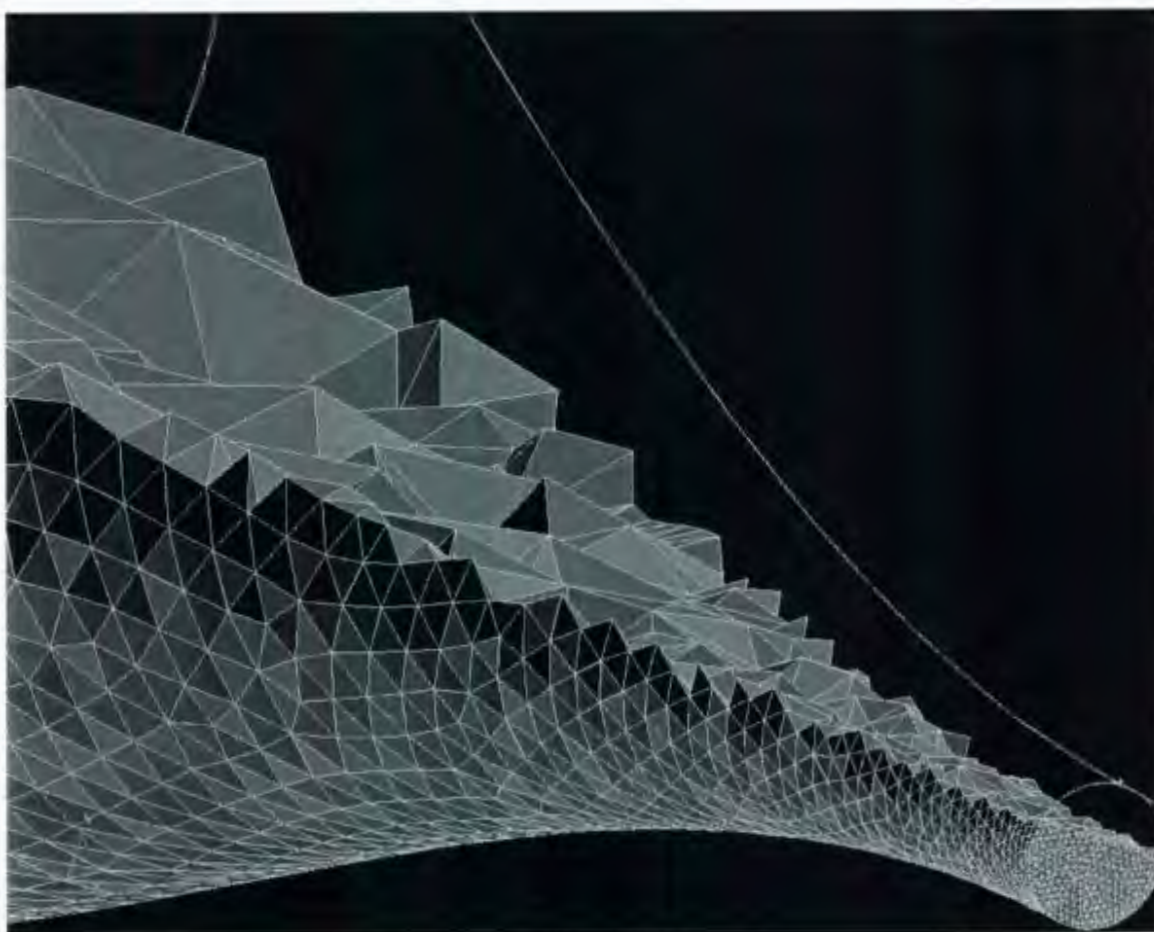


Figure 5.23 A planar cut view of the mesh elements in the converging section of the nozzle – (Section 2).

### 5.2.2. Sensitivity Analysis

The following is the discussions regarding various design parameters and their effects on flow characteristics in supersonic nozzles.

### 5.2.2.1. Inlet Pressure

Inlet pressure, as in the case of straight nozzles, is an important property that affects many of the flow characteristics including maximum velocity, position of the shockwave, and mass flow rate. It was concluded in Section 4.1.2.1 that the mass flow rate is directly proportional to the inlet pressure. Similar theories suggest the same relationship in the case of a nozzle with extended U-shaped section (see Equations 5.1 to 5.6). The results of the numerical solutions also confirm this analogy. Figure 5.24 shows the correlation between mass flow rate and inlet pressure for the geometry shown in Figure 5.19. The linear behaviour is emphasized by the extended trend-line passing through point (0,0). It must be noted that this linearity is only expected when the difference between the inlet and outlet pressures is high enough for the flow to be choked (see Section 4.1.2.1) and the zero intercept is only an extrapolation.

The relationship between inlet pressure and position of the shockwave is also similar to that of the straight nozzles. The irregular shape of the curvature profile for the U-shaped section makes it difficult to generate accurate reports of the position of the shockwave. The contour graphs of flow properties have been used instead to capture the relative position of the shockwave. Figure 5.25 shows the Mach number contours on the symmetrical cross-sectional surface of the geometry in Figure 5.19 for an inlet pressure of 345 kPa (50 psia) and outlet pressure of 101 kPa (14.7 psia). Similar contours were generated for different inlet pressures to establish the conclusion that increased inlet pressure moves the shockwave further away from the throat.

The maximum velocity of the gas through the nozzle is another important property that is greatly affected by the inlet pressure. Although the relationship between the two is still similar to that of the straight nozzle case, the importance of the maximum velocity itself is much more substantial in the case of a U-shaped nozzle. In the case of straight nozzles, the maximum velocity would have affected only the residence time for the separator. Whereas in this case, it is directly responsible for the centrifugal acceleration that creates the desired separation (see Equation 5.12). Figure 5.26 shows the values of velocity magnitude along the U section of the nozzle. Area-weighted average of the velocity magnitude is used to create this graph. It can be seen that although the cross sectional area of this section is constant, the velocity of the gas decreases continuously due to the loss of energy in its circular path. This behavior is observed until about 170 degrees (See Figure 5.27 for description of the angle) where the velocity starts to increase again. The reason for this change of behavior is not completely understood, but it appears that the flow follows a virtual extension of the diffuser from this point on. This may be understood more clearly by looking at Figure 5.27. An extrapolation of the diffuser is plotted in this figure with dotted lines and it can be seen that it intersects with the U section at about 170 degree position.

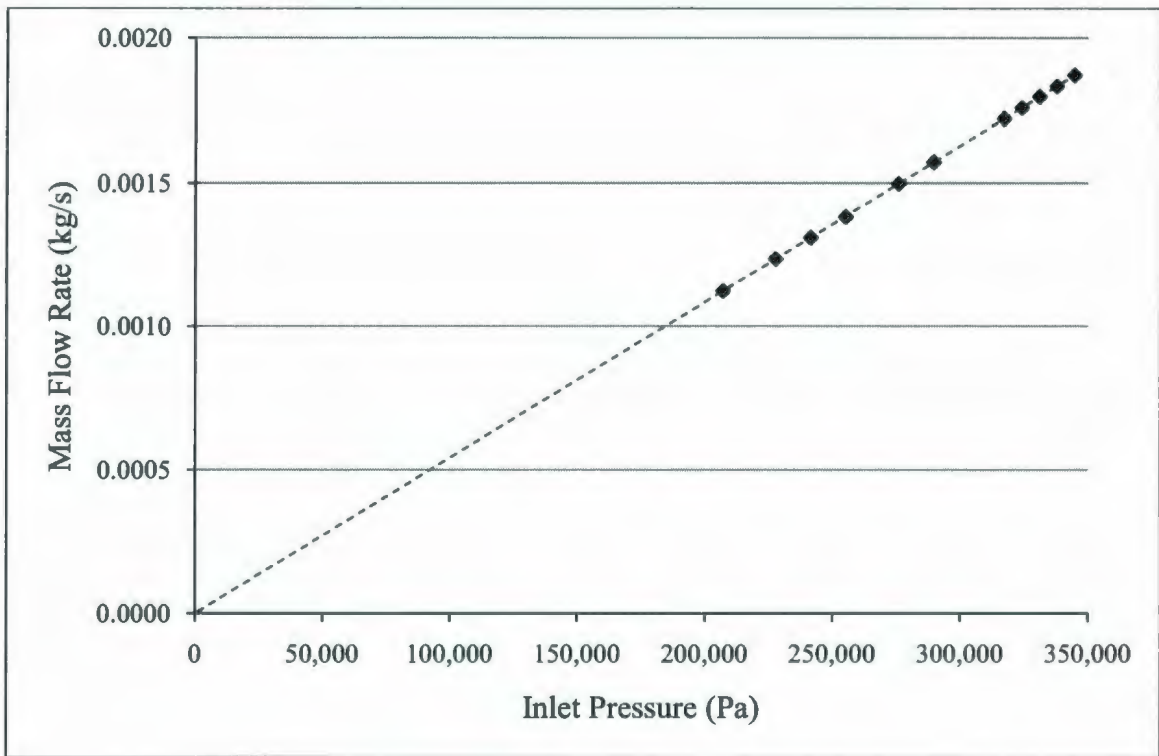


Figure 5.24 Mass flow rate through the U-shaped nozzle as a function of inlet pressure.

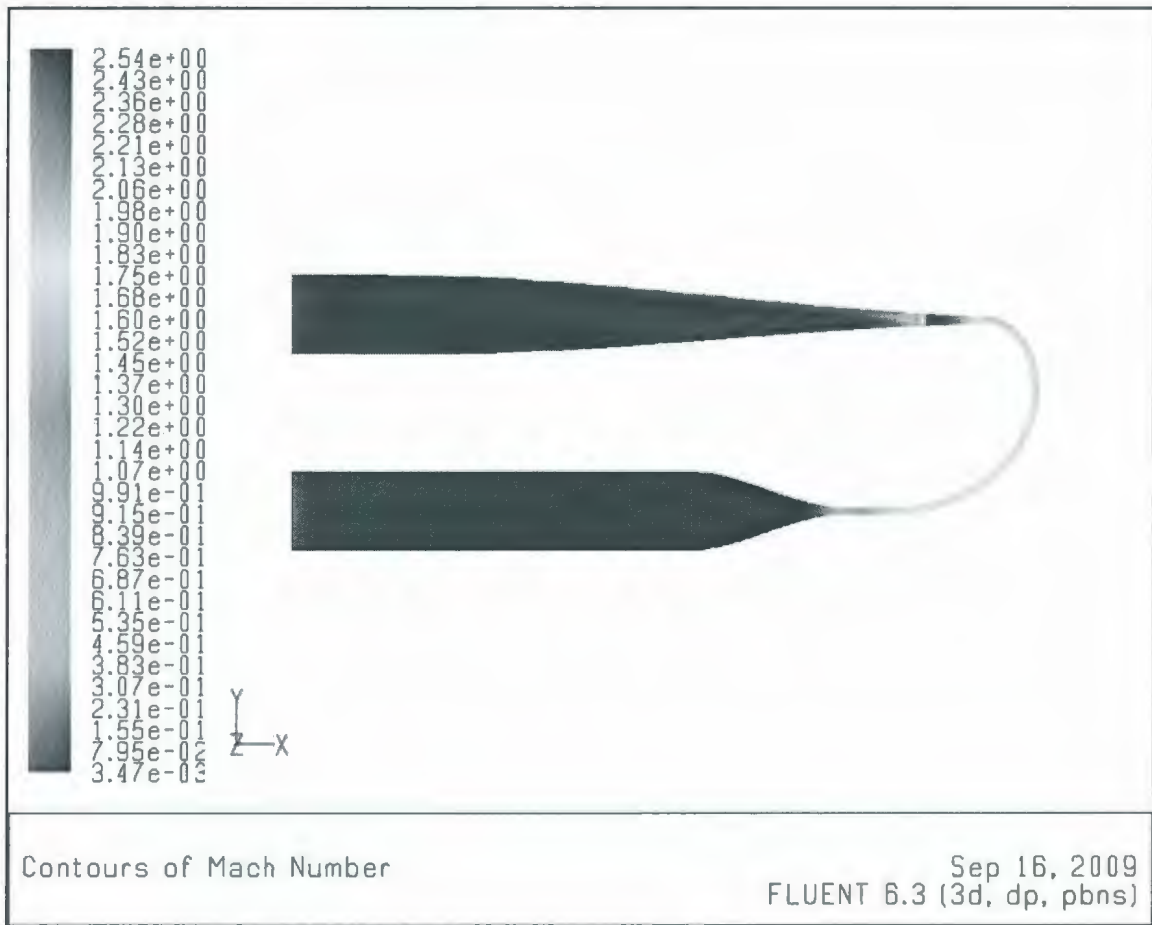


Figure 5.25 Mach number contours used in the determination of the position of the shockwave.

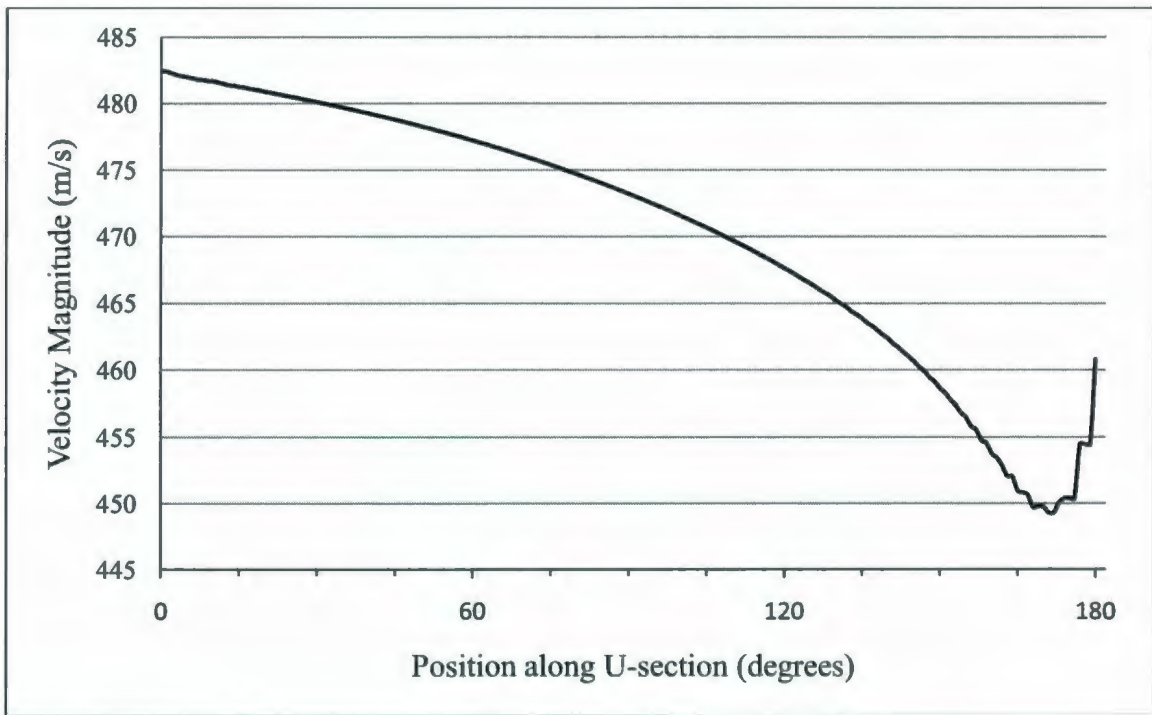


Figure 5.26 Variations of velocity magnitude along the U-shaped section. Angles show positions along the U-shaped section where zero degree denotes the beginning of the section and 180 its end.

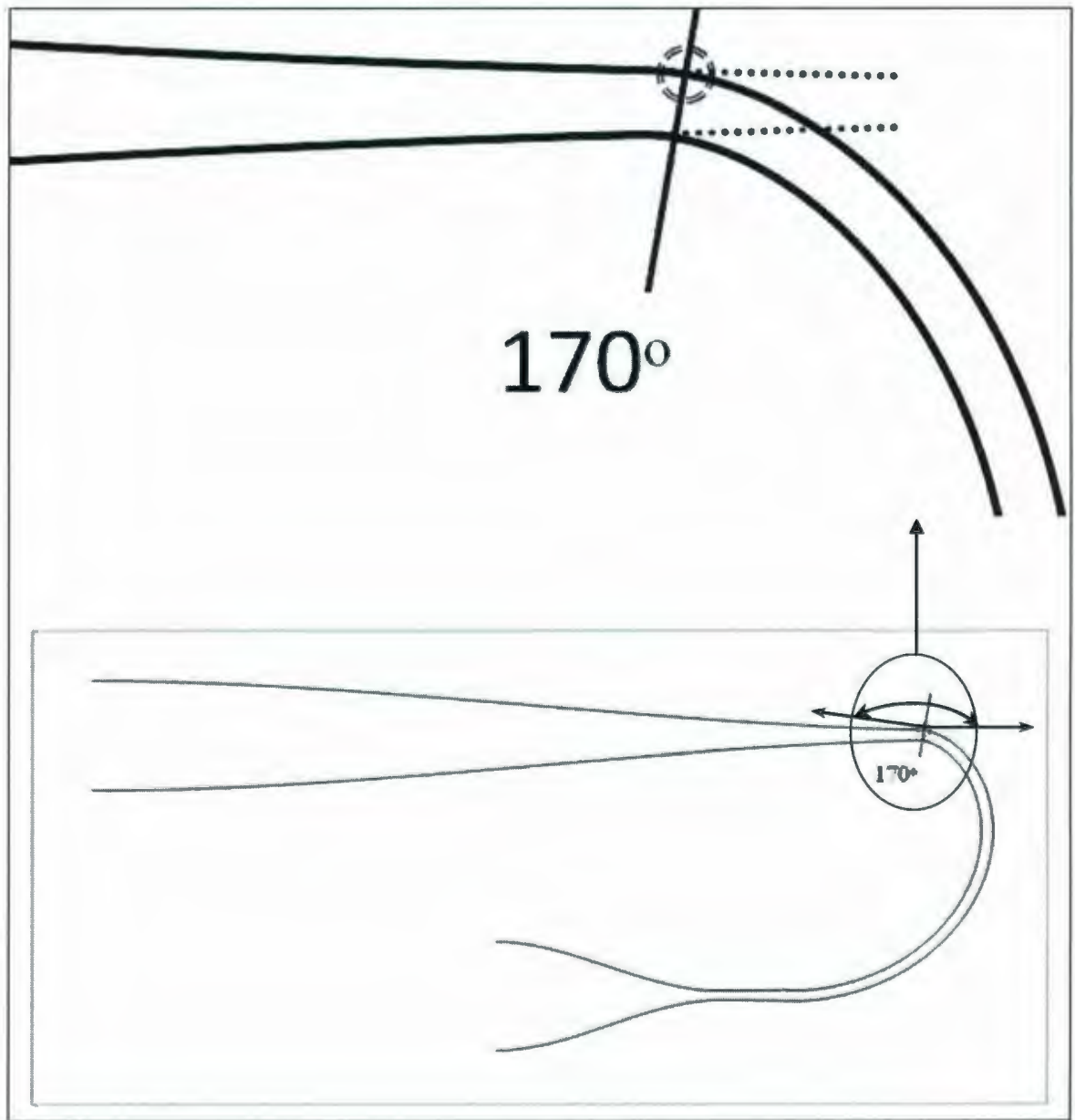


Figure 5.27 Extrapolation of the diffuser and its intersection with the U shaped section of the device.

### 5.2.2.2. Throat Diameter

Throat diameter is an important design parameter which along with gas inlet conditions, namely pressure and temperature, determines the flow capacity of the separator. It was shown in Section 4.1.2.1 that the mass flow rate of an ideal gas in a choked nozzle system can be calculated from Equation 5.6.

$$\dot{m} = A \left( \frac{2}{\gamma + 1} \right)^{\left( \frac{\gamma + 1}{2(\gamma - 1)} \right)} P_{in} \sqrt{\frac{\gamma M}{RT_{in}}} \quad (4.6)$$

The same principles apply to the flow of gas through a U-shaped extended nozzle. The throat diameter is therefore a design parameter that is used to determine the flow rate of the separator once inlet gas conditions are known. This is also in agreement with the results of the CFD simulations. It can be seen in Figure 5.28 that the flow rate of the separator is linearly proportional to the cross sectional area of the throat.

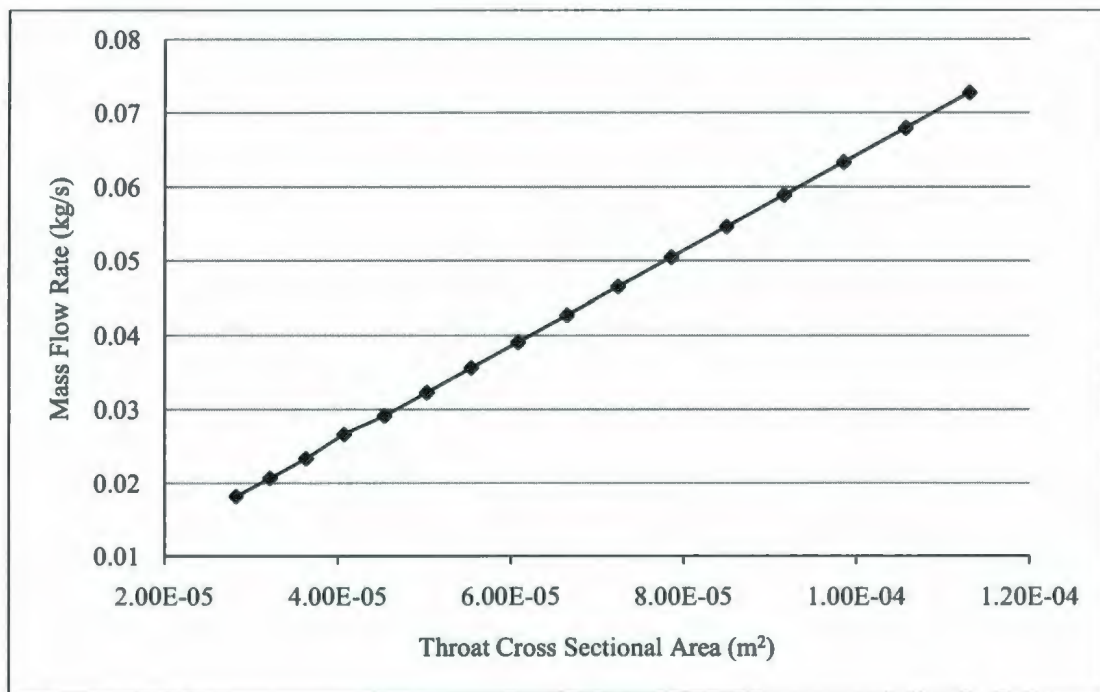


Figure 5.28 Results of CFD modeling indicating mass flow rate of a U-shaped nozzle with respect to the area of the throat. Note that the flow is choked at all times.

### 5.2.2.3. Curvature of the U-shaped Section

The curvature radius of the U-shaped section has two converse effects on the flow of the gas through the separator. Increasing the radius of the curvature allows the gas to pass through it with faster velocity and higher Mach number without triggering a shock wave, but at the same time reduces the centrifugal acceleration. This is easily shown by the kinematic expression of centrifugal acceleration:

$$a_c = \frac{V^2}{r} \quad 5.16$$

It may be concluded that since velocity is raised to the power of two in this equation, its value overweighs the negative value of increased radius. It should however be noted that an important feature of supersonic separators is their relatively small size, and a rather large radius of curvature will compromise this characteristic. After vigilant study of several designs with various curvature radii, it was determined that a U-shaped section with a decreasing radius profile would be the best configuration for this design. The proposed curvature profile shown in Figure 5.29 was therefore developed for the U-shaped section of the nozzle. The radius of this profile is 40 units in the beginning (lower left section) and decreases continuously until it reaches 5 units in the end (upper section). Figure 5.30 shows the linear decrease of the curvature radius with angular position along the U-shaped section.

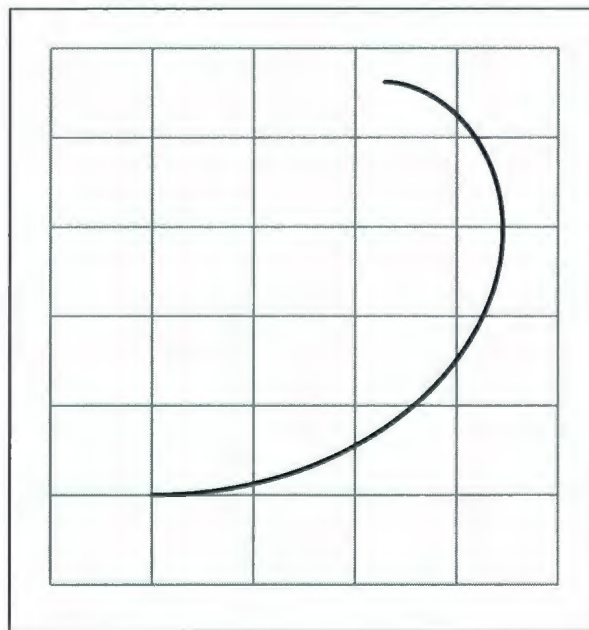


Figure 5.29 The decreasing radius profile developed for the U-shaped section of the nozzle.

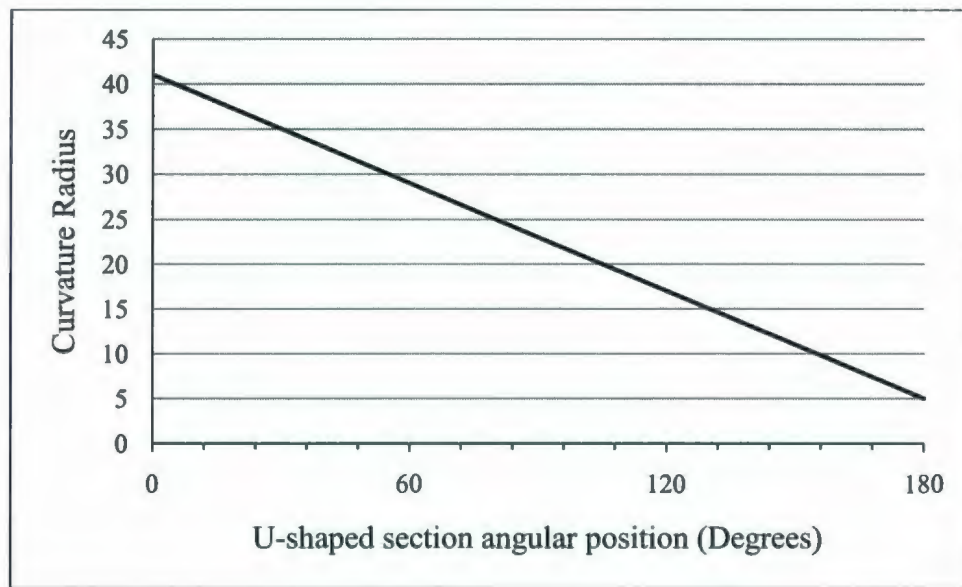


Figure 5.30 Linear decrease of the curvature radius with respect to the angular position of the curvature.

#### 5.2.2.4. Inside Diameter of the U-shaped section

It is a known fact that the flow always reaches sonic velocity at the throat (given a certain pressure driving force is available). The slight divergence after the throat and before the U-shaped section is to allow the flow to reach supersonic velocity. Assuming pressure drop across the nozzle is large enough, the value of the Mach number at the entrance to the U-shaped section depends solely on the ratio of the diameter at this point to that of the throat. Since the purpose of the U-shaped section is to take advantage of the supersonic flow in a circular path, it is important that the shock takes place in the diverging section. It must be noted that despite the constant diameter of the nozzle throughout the U-shaped

section, a shock wave may take place inside that section due to the loss of energy in the U-shaped section (see Figure 5.31).

The U-shaped section to throat diameter ratio of 1.2 was determined to be most effective in this study. This means that the constant cross-section area of the U-shaped section has a diameter of 1.2 times the diameter of the throat. It is important to realize that this ratio is not the only factor that determines the position of the shock. Other parameters involved are the U-shaped section curvature radius and outlet back pressure.

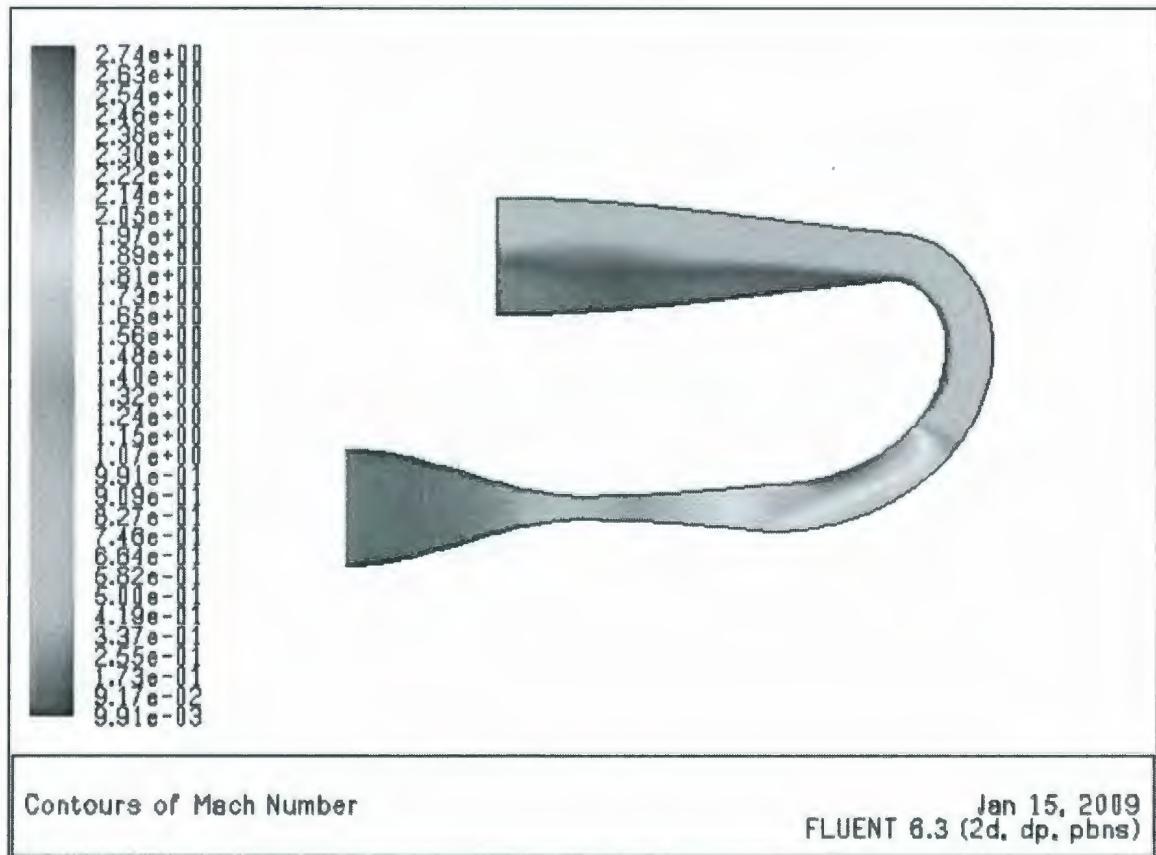


Figure 5.31 Occurrence of a shockwave inside the U-shaped section with constant cross-sectional area.

#### 5.2.2.5. Centrifugal Acceleration

Particle separation occurs due to the centrifugal force that is exerted on the flow as it passes through the U-shaped section with high velocity. The particles (e.g. micron size liquid droplets) are forced towards the outermost wall in the U-shaped section and may be extracted via a side channel that is installed in an appropriate position. Figure 5.32 shows the values of centrifugal acceleration along this section as it is experienced by the flow. The acceleration is calculated from Equation 5.16:

$$a_c = \frac{V^2}{r} \quad (4.16)$$

The graph is generated from the CFD simulation results for the geometry shown in Figure 5.19 when an inlet pressure of 345 kPa (50 psia) was imposed. It can be seen in the graph that the particles experience centrifugal accelerations of up to 33,000,000 m/s<sup>2</sup> in this particular configuration. That is the equivalent of approximately 3.4 million g.

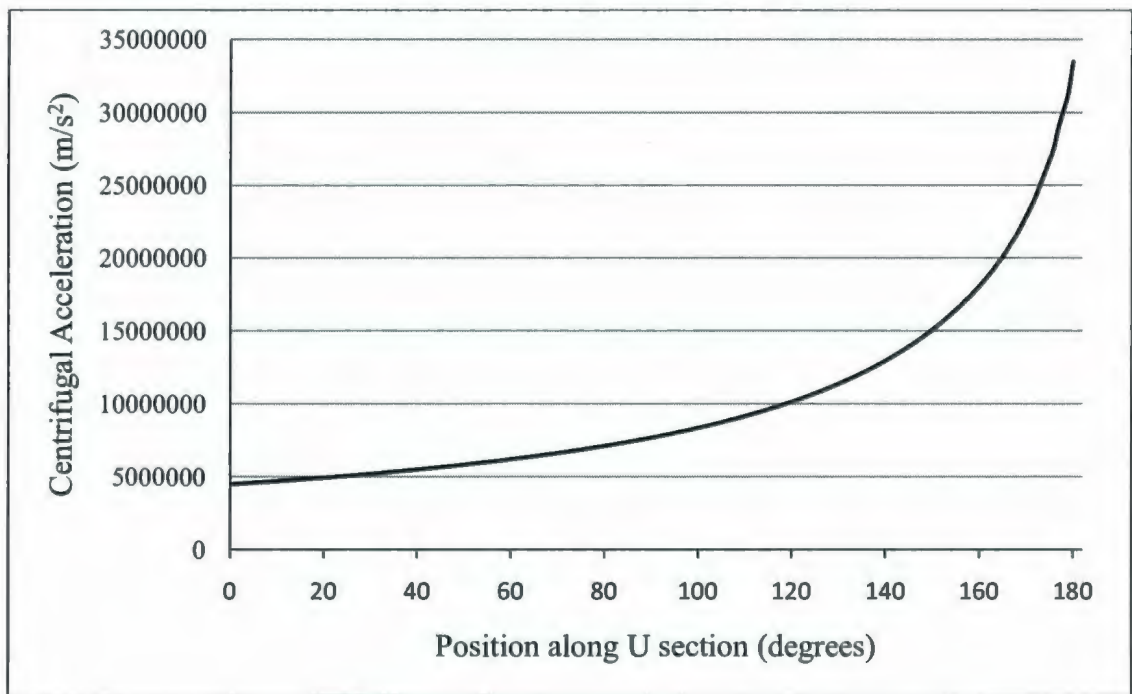


Figure 5.32 Centrifugal acceleration along the U-shaped section of the nozzle. Degrees represent the position along the U-shaped section where 0 degree is the beginning of the U and 180 is the end of it.

#### 5.2.2.6. Outlet Back Pressure

The influence of outlet back pressure on the flow characteristics of a straight nozzle was discussed in Section 4.1.2.4. It was shown that increasing the outlet back pressure reduces the maximum velocity of the gas and the position of the shock wave is pushed closer to the throat. The same principles and conclusions also apply to nozzles with extended U-shaped section. The effects of the outlet back pressure were briefly studied in this type of separators. It is evident that once the inlet conditions of the process gas are determined, the cross sectional area of the throat is solely responsible for the control of

flow rate. The outlet back pressure will therefore be the only parameter that governs the position of the shockwave as well as the pressure recovery ratio. One of the most desirable characteristics of these separators is their relatively high pressure recovery. In order to benefit from this feature, it is only logical that the shockwave takes place downstream but closest to the U-shaped section. It is also apparent that the shock should not take place in the U-shaped section where the actual separation is achieved via the supersonic flow of the gas. Hence, the outlet backpressure is always regulated to satisfy these two criteria.

### 5.2.3. Position of the Separation Channel

One important design parameter is to determine where the side channel that is to separate the flow of particles from the main gas flow should be placed. This can also be easily determined using the post processing features of the CFD package. A volume density contour will precisely show where most of the higher density particles are accumulated along the U-shaped section (see Figure 5.33).

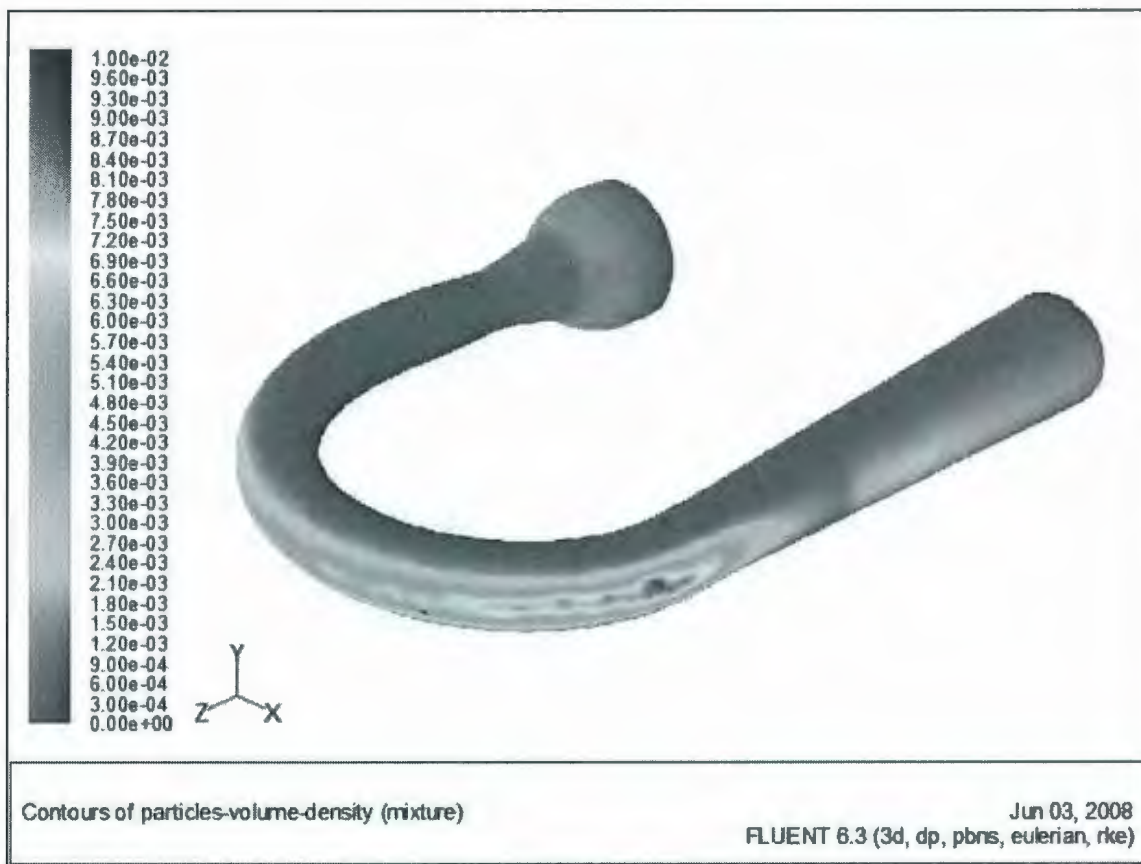


Figure 5.33 Contours of volume density of the particles that pinpoint the position of the separation side channel.

### 5.3. COMPARISON OF STRAIGHT AND U-SHAPED NOZZLES

It was established in the previous discussions that the general behavior of the two concepts is basically the same in response to changing pressures or throat diameter. In order to make a practical comparison between the two proposed concepts, a method of measuring the actual obtained separation is required that incorporates the significance of flow rates and pressure recovery ratios. In the absence of such experimental data, the comparison is based on the main property responsible for the separation that is readily available from the CFD simulation results, namely the centrifugal acceleration. The centrifugal acceleration exerted on the particles of the gaseous mixture was discussed in details for the swirling flow of gas inside a straight nozzle and the non-swirling flow of gas through a nozzle with extended U-shaped throat in Sections 4.1.2.2 and 4.2.2.5, respectively. The individual values of this property for the two concepts can now be compared for similar pressure recovery ratios and flow rates. An inlet pressure of 345 kPa (50 psia) and outlet back pressure of 138 kPa (20 psia) were used for this comparison.

Figure 5.34 is a graph of the centrifugal acceleration exerted on the gaseous mixture for both concepts. The swirling flow of gas through a straight nozzle is represented by the same geometry that was discussed in Section 4.1 with an initial swirl velocity ratio of 3.50. The mass flow rate associated with this configuration is determined to be 146.5 kg/hr. A U-shaped nozzle that accommodates this flow rate while operating with an inlet pressure of 345 kPa must have a throat diameter of about 8 mm (see Equation 5.6). The

curve representing the U-shaped nozzle is created using this analogy and by the linear enlargement of the geometry discussed in Section 4.2. The values of centrifugal acceleration are calculated using Equation 5.16 for both curves. Area-weighted average velocities are used to create more realistic results.

It can be seen from the resulting graph (Figure 5.34) that although centrifugal acceleration reaches significantly high values in the swirling flow in a straight nozzle, it peaks only at the throat and follows a decreasing pattern along the diffuser where the actual separation is expected. On the other hand, for the U-shaped nozzles, not only the centrifugal acceleration keeps rising through the U section, it reaches far greater values than obtained in a straight nozzle. It can be concluded here that a separator of the U-shaped nozzle concept will provide potentially better separation under the same operating conditions.

Table 5.4 Summary of the comparison between the two proposed configurations

	Straight nozzle with swirling flow	U-shaped nozzle
Inlet Pressure (kPa)	345	345
Outlet Back Pressure (kPa)	138	138
Mass Flow Rate (kg/hr)	146.5	146.5
Maximum Centrifugal Acceleration exerted on the gas ( $m/s^2$ )	~ 6,000,000	~ 7,000,000
Position of the maximum acceleration	At the throat, at the beginning of the separation length	At the end of the U-shaped section

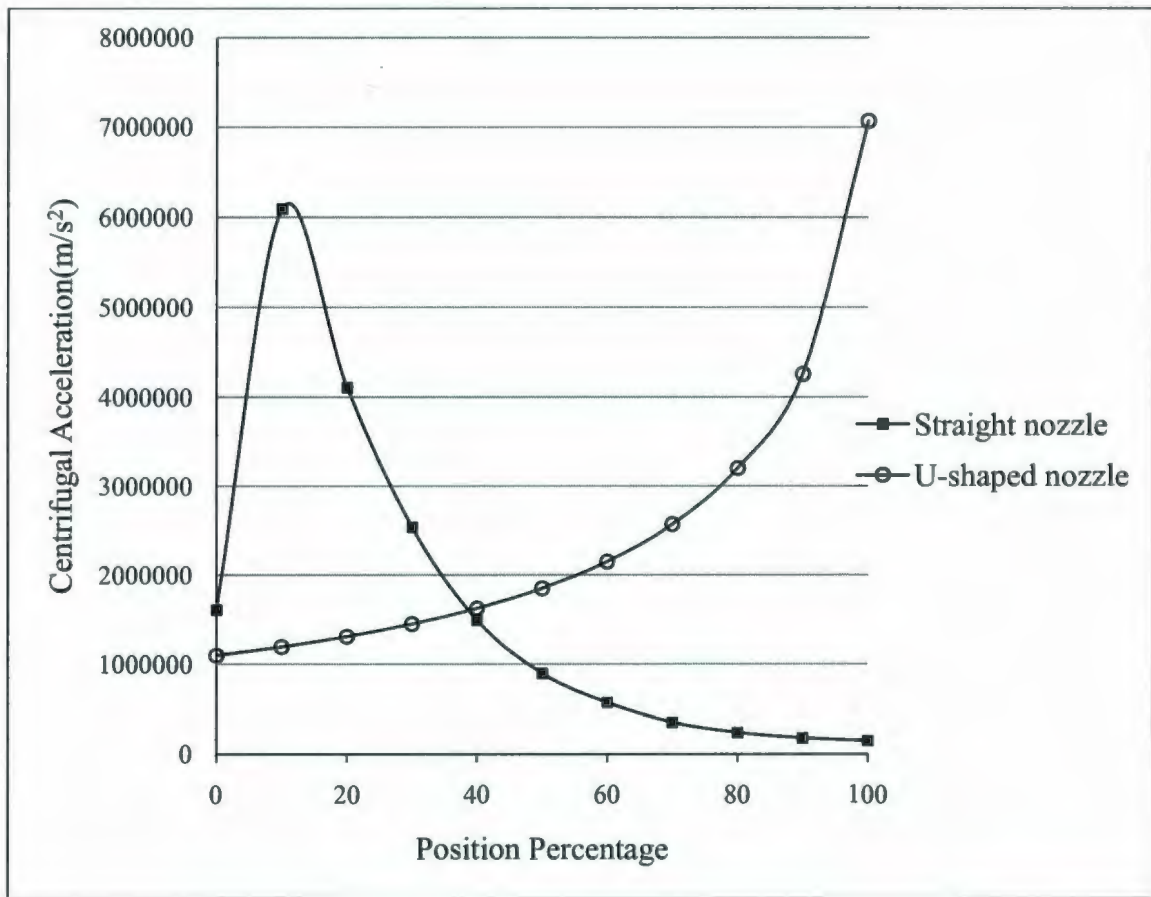


Figure 5.34 Comparison of centrifugal acceleration for the two proposed concepts: swirling flow of gas in a straight nozzle and U-shaped nozzle.

## **6. MODEL EVALUATION AND LABORATORY EXPERIMENTS**

The novel nature of this study and the lack of external data required laboratory pilot tests in order to evaluate the results of CFD simulations. The idea was to create a physical nozzle system similar to those that had been simulated through which high pressure gas would flow. Pressure, temperature, and flow rate measurements would be made and the results compared to those of the CFD simulations of the same system. The geometry chosen for the tests was the same as what is shown in Figure 5.19 and the process gas was compressed air. Two symmetrical halves of the proposed geometry was machined out of two blocks of aluminum and put together to form the desired pathways. Since it is significantly important that the flow is not disturbed by any bodily imperfection or hindrance, direct in-line pressure and temperature measurement was not an option. Small diameter channels were created at several points along the pathway to enable the placement of measurement probes outside the fluid's pathway. As seen in Figure 6.1, there are 12 pressure and 4 temperature measurement points. Figure 6.2 shows the schematics of the lab test setup.

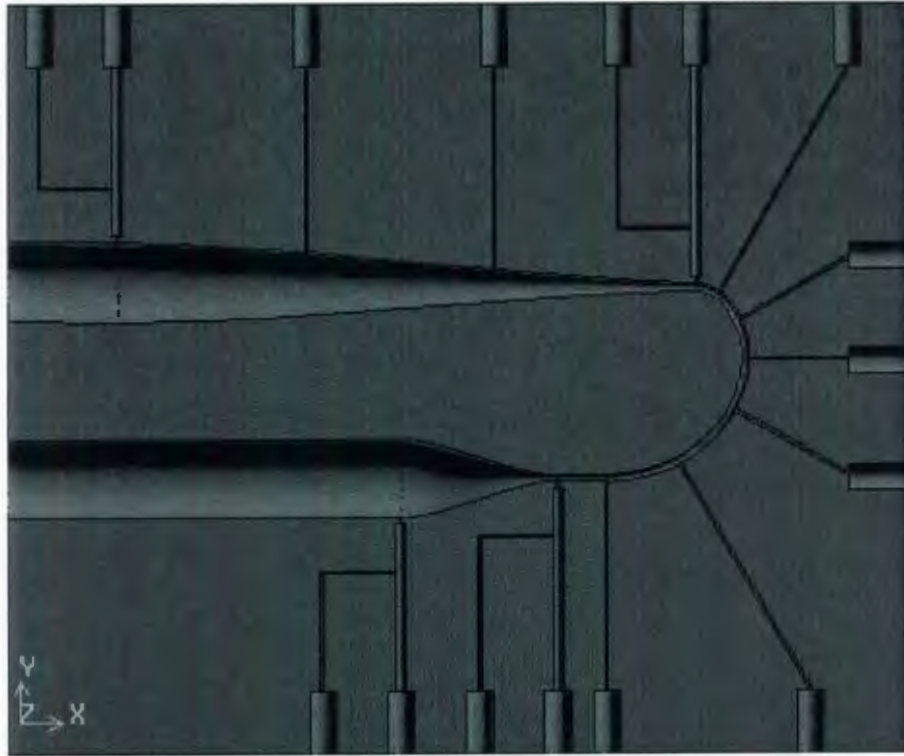


Figure 6.1 The bottom piece of the lab test nozzle system. The 4 thicker channels are designed to accommodate temperature probes. All other channels are for pressure measurements.

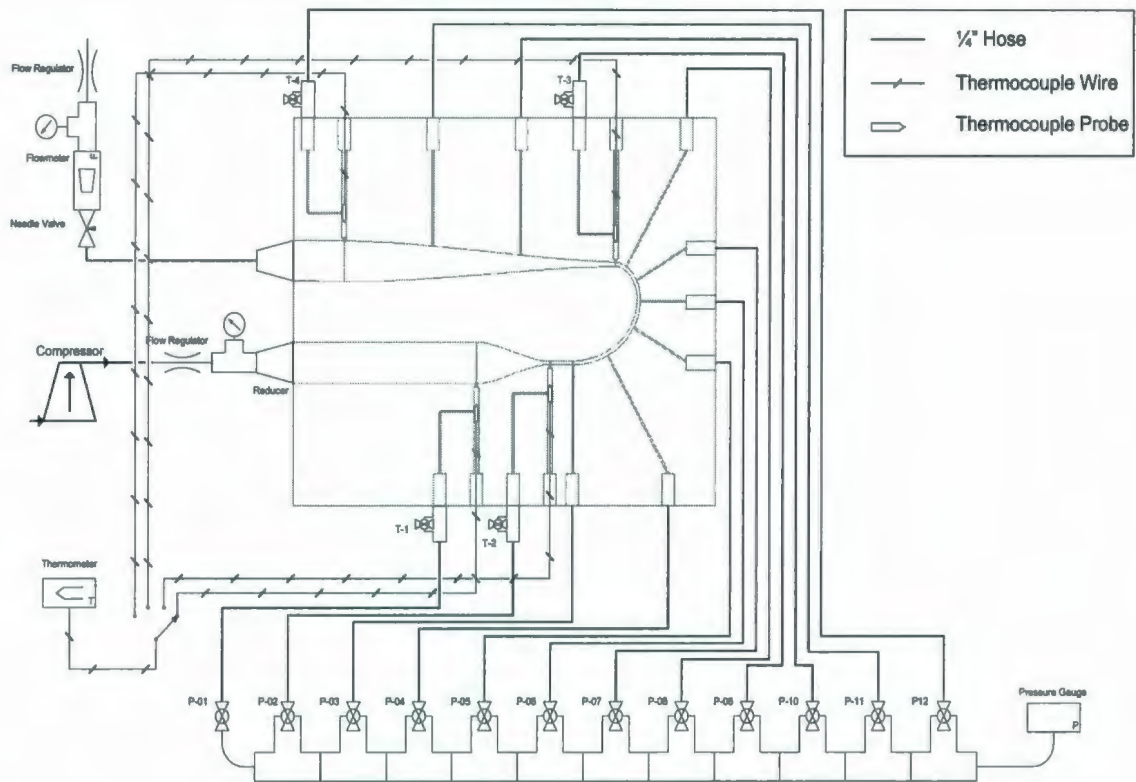


Figure 6.2 Process flow diagram describing the schematic setup of the pilot test.

## 6.1. TEST SET-UP

The equipment and materials used in this experiment are explained in the following sections.

### 6.1.1. Nozzle System

The nozzle geometry chosen for this study is shown in Figure 5.15. In order to build such a nozzle configuration with considerably smooth walls, the model was generated with

GAMBIT and then exported to the Haas VF3 machining centre (Figure 6.3) for production. The proposed design was split into two symmetrical halves, each of which machined out of a block of aluminum (Figures 6.4 and 6.5). The two blocks were then put together to form the desired flowlines (Figure 6.6). One of the main challenges in this procedure was the problem of sealing the two blocks in a way that the high pressure air does not leak out of the system. After several attempts with different sealants such as air gaskets and oil, silicon sealant was used to create the desired conditions. Although the seal was still not perfect and leaked at some points when the pressure was very high (above 500 kPa), it performed reasonably acceptable at lower pressures.

#### 6.1.2. Pressure Measurement

It was previously mentioned that it is imperative that the gas flow path is not disturbed with any bodily imperfection. The method devised was to create small diameter (about 1 mm) channels to connect a pressure gauge to predetermined measurement points along the device (see Figure 6.1). NPT/Push-on fittings were then attached to the aluminum block and hoses were used to connect each measurement channel to a specifically developed pressure manifold (Figure 6.7). This manifold was designed to incorporate a single pressure gauge to make measurements at all designated points; one at a time. The gauge used (shown in Figure 6.8) was a General Electric make with a range of 0 to 690kPa (0-100 psi) and an accuracy of  $\pm 0.05\%$  of the full scale.

### 6.1.3. Temperature Measurement

Temperature measurement was performed using a thermocouple thermometer. The probes were custom made type T gas probes with an NPT/compression fitting mounted on the handle (see Figure 6.8). There were four temperature measurement points as shown in Figure 6.1. The four probes were connected to a thermocouple signal switch box which was connected to an Oakton single input thermocouple thermometer (Figure 6.8). The temperature range for this setup was -250 to 400 °C with a resolution of 0.1 °C.

### 6.1.4. Flow Measurement

A Cole-Parmer variable area flow meter (Figure 6.8) was used at the outlet of the apparatus as indicated in the process flow diagram (Figure 6.2). Flow up to  $3.87 \times 10^{-3}$  m<sup>3</sup>/s (8.2 scfm) could be measured with this device with an accuracy of  $\pm 3\%$  of the full scale.

### 6.1.5. Air Supply

The compressed air was supplied with a mobile 0.08 m<sup>3</sup> (22 gallon) compressor (Figure 6.8) with a maximum pressure of 860 kPa (125 psi). The compressor used a 1268 w (1.7 Hp) motor that could deliver a nominal flow rate of  $2.64 \times 10^{-3}$  m<sup>3</sup>/s (5.6 scfm) at 276 kPa (40 psi) and  $1.79 \times 10^{-3}$  m<sup>3</sup>/s (3.8 scfm) at 620 kPa (90 psi). One major drawback of this choice was that the compressor needed to be working while the test was being done and the compressed air temperature would consequently rise as time elapsed. This in turn would affect the test results, specifically temperature readings.



Figure 6.3 The Haas VF-3 machining centre was used to machine the nozzle configuration and measurement channels out of the aluminum blocks (picture from [http://www.haascnc.com/prod/pi/VF-3\\_lg.jpg](http://www.haascnc.com/prod/pi/VF-3_lg.jpg)).

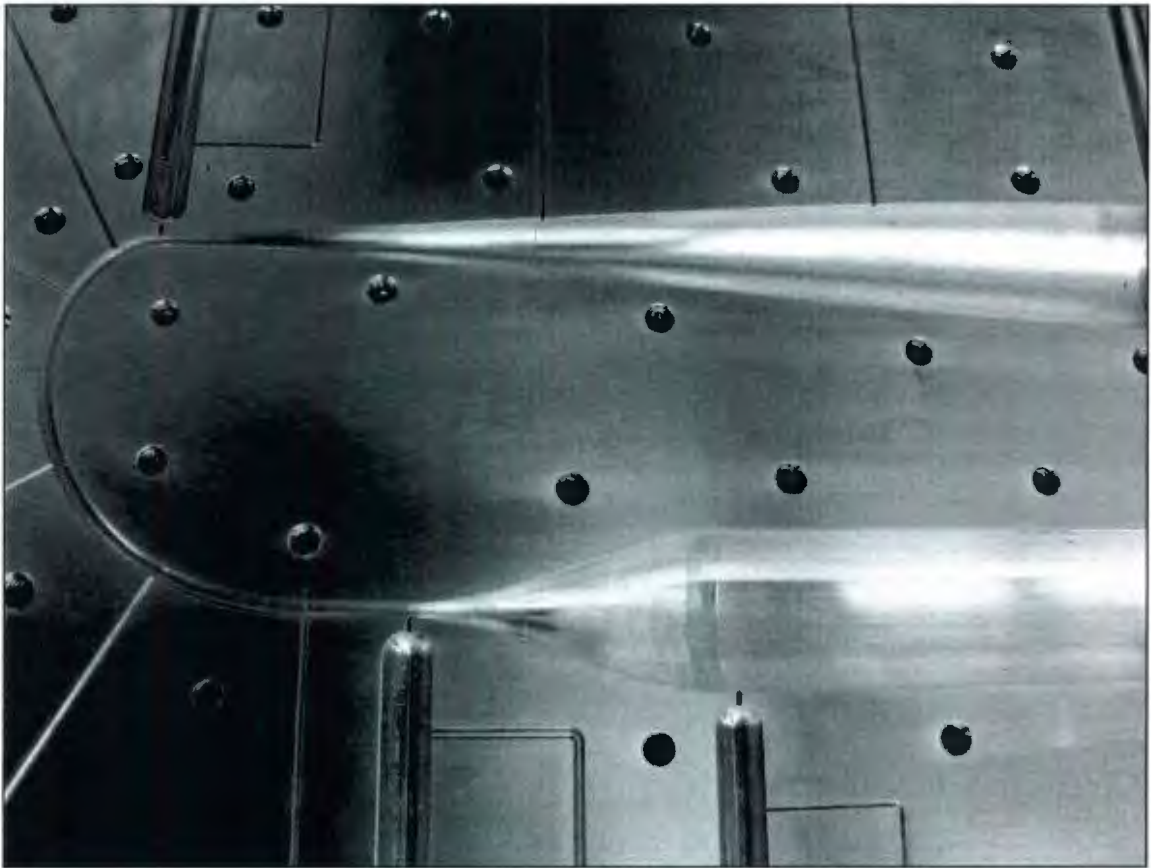


Figure 6.4 A shot of the machined aluminum block showing the nozzle configuration and measurement channels.



Figure 6.5 A shot of the machined aluminum block showing the measurement channels and NPT fitting threads.



Figure 6.6 A shot of the test apparatus showing the assembled nozzle and installed fittings and thermocouple probes.



Figure 6.7 Pressure measurement manifold. The elbow on the far left is to be connected to the pressure gauge.

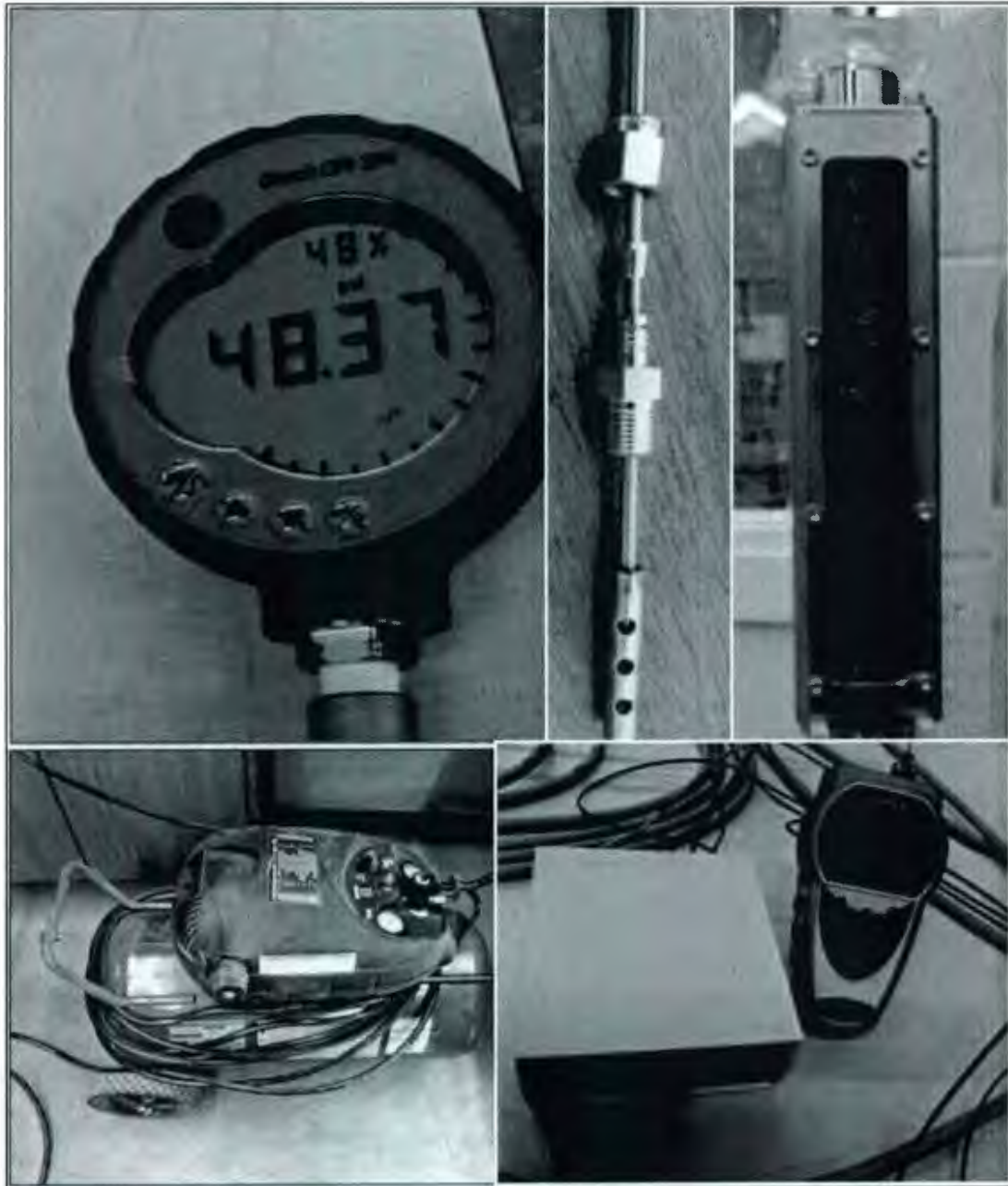


Figure 6.8 The equipment used for the experiment.

## 6.2. TEST OUTLINE

The test procedure is outlined in this section. The valve numbers used are in accordance with the process flow diagram in Figure 6.2.

Initial configuration:

All valves are closed (Needle valve, regulating valves, P-01 through P-12, and T1 through T4).

Test procedure:

1. The needle valve is opened slowly to allow the flow of compressed gas while watching not to cause the flow meter float to oscillate.
2. When the flow rate reaches its maximum, the flow rate is read from the flow meter.
3. Valves T-1 through T-4 are opened one at a time. The thermocouple switchbox is set to the corresponding position while each T valve is open to read the gas temperature. It is important to note that only one valve is opened at any time to minimize the loss of air from the device.
4. After all four temperature readings are complete, the T valves remain closed for the rest of the experiment.
5. Valves P-01 through P-12 are opened one after the other to perform pressure readings throughout the device. Only one valve is opened at any time.

6. After all 12 pressure readings are performed, the device is set to the initial configuration. Another pressure is selected for the compressor outlet and the procedure is repeated starting Step 1.

### 6.3. RESULTS

The results of the experiments were gathered and tabulated as pressure, temperature, and flow rate measurements for different inlet and outlet pressures. Figure 6.9 shows a sample plot of the pressure readings from the experiment that were collected on a test run with an inlet pressure of 172 kPa (25 psi) and an outlet back pressure of 138 kPa (20psi). The CFD generated results of the same configuration is also included for comparison. It can be seen from this figure that the CFD model has a very accurate prediction of the pressure profile. Figure 6.10 shows another graph of the same type for a test run with an inlet pressure of 414 kPa (60 psi) and an outlet back pressure of 276 kPa (40 psi) which also shows the accuracy of the CFD simulations. A maximum error of 13% can be observed in these two graphs. Figure 6.11 shows a graph of the mass flow rate through the nozzle as a function of the inlet pressure. It can be seen here that the CFD model has generated fairly accurate predictions of the mass flow rate. The increased error in the high pressure end of the experiment data may be attributed to the loss of air from the leaks mentioned before. This comparison shows an error of 3.6% to 10% for the CFD simulated results.

This experiment was not successful in measuring the temperature of the gas correctly. The thermometers appeared to register the room temperature at all times. This may be attributed to the fact that the flow of air through temperature measurement channels is very small. This in addition to the high heat conductance of aluminum may have created this failure. It is although theoretically valid to assume that since pressure and flow rate results from the CFD simulations are reliably accurate in comparison with the experimental values, the temperature predictions are also acceptable. This is due to the fact that temperature can be calculated as a function of pressure and density from thermodynamic equations.

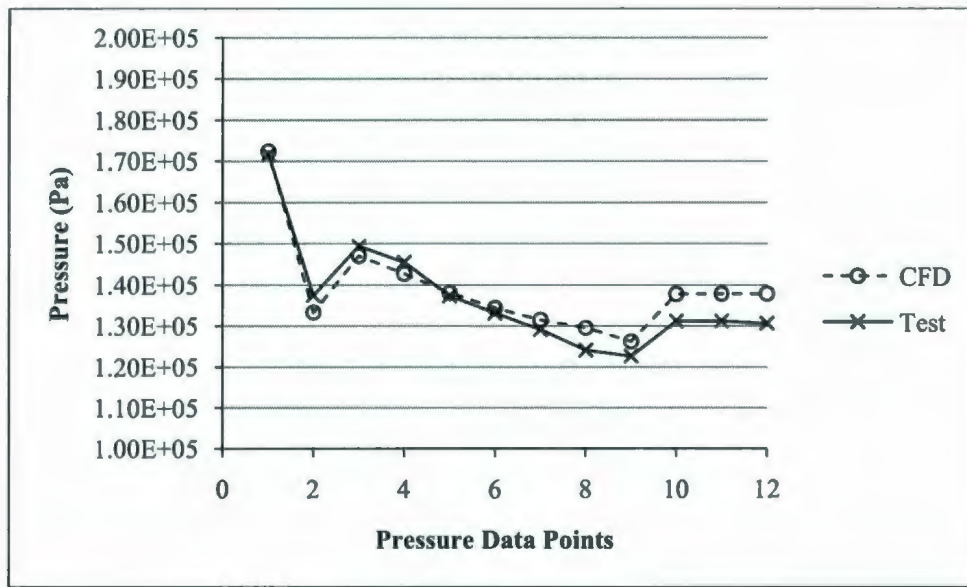


Figure 6.9 Comparison of the pressure measurements along the device with the CFD simulated pressure values. Inlet pressure is 172 kPa and the outlet back pressure is 138 kPa.

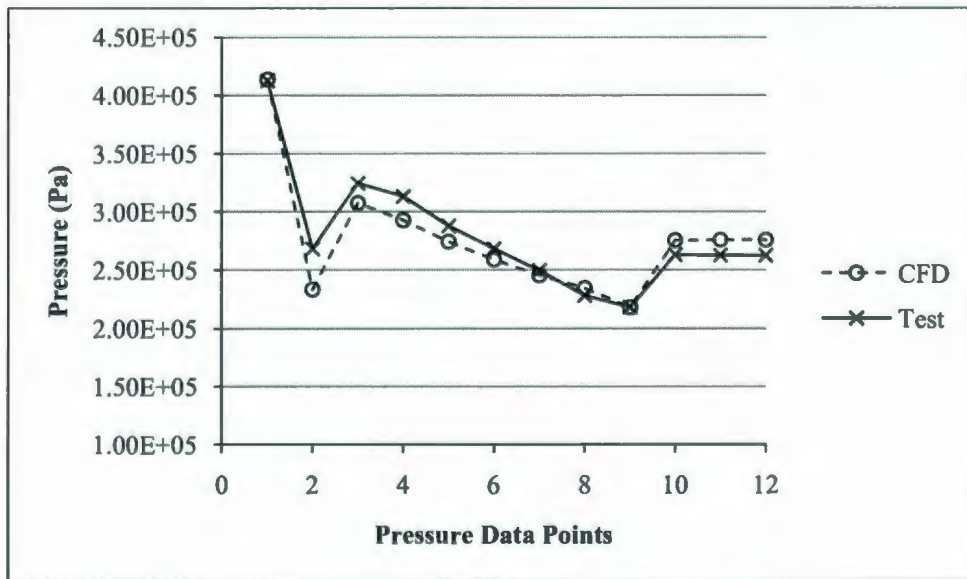


Figure 6.10 Comparison of the pressure measurements along the device with the CFD simulated pressure values. Inlet pressure is 414 kPa and the outlet back pressure is 276 kPa.

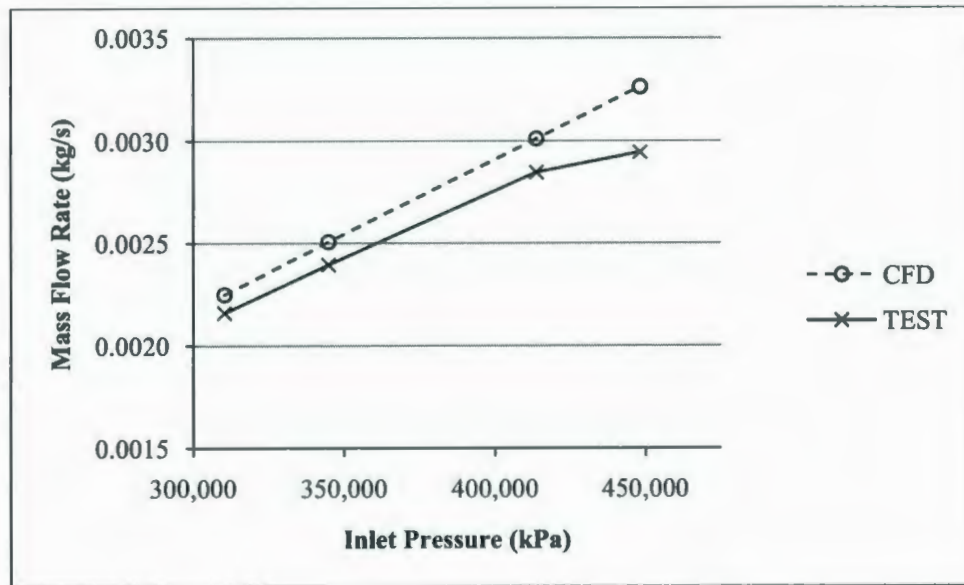


Figure 6.11 Mass flow rate measurements from the experiment compared to the CFD simulated results for different inlet pressures.

## 7. CONCLUSIONS AND RECOMMENDATIONS

The purpose of this study was to investigate the performance of supersonic separators with different designs and in different operating conditions. The method of computational fluid dynamics (CFD) analysis supported by some experimental tests was chosen for this objective. In this approach, several design parameters such as throat diameter and diffuser profiles were identified and different nozzle configurations were modeled using the geometry and mesh generation software of the commercial Fluent CFD package, namely GAMBIT. These models were then exposed to variations of several operating conditions including different inlet pressures and swirl intensities, and solved using the processing software of the CFD software package. An alternative configuration to the swirling flow of gas through the nozzle was also proposed and studied. The supersonic flow of gas in a U-shaped nozzle was investigated with the CFD method and results were compared with the original configuration. Finally, in the absence of external experimental data, a lab set-up was designed and experiments were conducted to validate the results of the CFD simulations. The following conclusions are drawn from this work:

1. Computational fluid dynamics is a robust and reliable method for the study of supersonic separators.
2. The position of the shockwave in both of the studied configurations (swirl-type and U-shaped nozzles) depends on the pressure driving force across the device. This pressure driving force is equivalent to the difference  $P_{in} - P_{out}$ . It is

technically an operational advantage if the shockwave takes place further away from the throat and closer to the exit. This condition increases the time for particle recovery and happens if the pressure driving force is increased. This in turn has the disadvantage of a lowered pressure recovery. The compromise between these two situations, namely a better separation and higher pressure recovery, remains a challenge unique for each design.

3. Increased inlet pressure will result in an increase in the flow capacity of the device in both configurations. If the outlet back pressure is unchanged, the pressure recovery will fall and the shockwave will be pushed further away from the throat. However, if the outlet backpressure is increased to maintain a constant pressure recovery ratio, the position of the shockwave will remain unchanged.
4. In the swirling flow of gas in a straight nozzle configuration, increasing the inlet swirl intensity will increase the centrifugal acceleration which in turn will increase separation ratio. However, the converse effect of this action may be observed in a flow capacity decrease.
5. The area of the throat is a design parameter that is directly proportional to the expected flow capacity. It is recommended that this area be calculated from Equation 5.6 as a function of the mass flow rate, once the inlet flow conditions are determined.
6. The cross-sectional area of the elongated throat section or that of the U-shaped section are key factors in determining the velocity of the gas in those sections. It

is therefore essential that great care is employed while determining this design feature.

7. The curvature radius of the U-shaped section has a strong effect on the velocity profile of the gas and more specifically, the possibility of a shockwave taking place in this section. This radius is also a key factor in determining the amount of centrifugal acceleration the gas is exposed to for particle separation purposes. Increasing this radius reduces the chance of shockwave taking place inside the U-shaped section, but also reduces the centrifugal acceleration. The variable radius profile proposed in this work presents a good compromise between these two effects.
8. The overall performance of the two proposed configurations is yet to be determined, but it can be concluded from this work that the amount of centrifugal acceleration exerted on the particles is much higher in the U-shaped nozzle configuration and it is therefore potentially more efficient in separation of contaminants like water from natural gas.

The following recommendations are proposed for future work in this area:

- The dependence of mass flow rate on inlet pressure and inlet swirl intensity was addressed separately in this work. It is recommended that these factors are combined and incorporated into a single mathematical relationship
- The presence of a boundary layer in the near axis region of the swirling flow was discussed. It would be beneficial to study this element more extensively and to

introduce designs in which an inner body is incorporated into the system to facilitate the swirling flow of gas inside the nozzle.

- The effects of gravitational force were neglected in this study. A further detailed study incorporating the effects of gravity on the liquid film is recommended.
- The study of the effects of the presence of nano-size particles in the gaseous mixture is also beneficial.
- The kinetic aspect of the nucleation process involved in this method of separation is another study that could benefit the understanding of these separators.
- A study could be conducted on the possibility of a controlled nucleation and growth mechanisms to produce particles of an optimum size.

## REFERENCES

- Alfyorov, V., (2005). "Supersonic nozzle efficiently separates natural gas components". *Oil and Gas Journal*, 103(20), 53-58.
- Brouwer, J. M., (2003). "Twister supersonic gas conditioning for unmanned platforms and subsea gas processing". *Offshore Europe Conference - Proceedings*, , 219-225.
- Brouwer, J. M., (2004). "Supersonic gas conditioning first commercial offshore experience". *GPA Annual Convention Proceedings*.
- Crook, J., (2006). "Twist and shout". *Chemical Engineer (London)*, (782), 54-56.
- Energy Information Administration (EIA), "International Energy Outlook 2007 (IEO2007)", May 2007, 39-48
- Feygin, V., (2006). "Supersonic gas technologies". *International Gas Union World Gas Conference Papers*, 1, 162-168.
- Fluent Inc., "Fluent 6.3 User's Guide" , 2006
- Fluent Inc., "Gambit 2.4.6 User,s Guide", 2007
- Hengwei, L., (2005). "Characteristics of a supersonic swirling dehydration system of natural gas". *Chinese Journal of Chemical Engineering*, 13(1), 9-12.
- Jassim, E. & Abdi, M. A. & Muzychka, Y. (2008). "Computational fluid dynamics study for flow of natural gas through high-pressure supersonic nozzles" *Petroleum Science and Technology*, 26(15), 1757-1785
- Karimi, A., (2006). "Selective removal of water from supercritical natural gas". *SPE Proceedings - Gas Technology Symposium, 2006*, 259-265.
- Karimi, A., & Abdi, M. A. (2009). "Selective dehydration of high-pressure natural gas using supersonic nozzles". *Chemical Engineering and Processing: Process Intensification*, 48(1), 560-568.
- Kundu, P. K., & Cohen, I. M. (2008). "*Fluid mechanics*" (4th ed.). Boston: Academic Press.
- Malyshkina, M. M., (2008). "The structure of gasdynamic flow in a supersonic separator of natural gas". *High Temperature*, 46(1), 69-76.

- Meyer, H. S., (2007). "An improved and energy efficient natural gas liquids (NGL) removal process". *AIChE Annual Meeting, Conference Proceedings*.
- Okimoto, F. T., (2003). "Twister supersonic gas conditioning - studies, applications and results". *GPA Annual Convention Proceedings*.
- Okimoto, F., (2002). "Supersonic gas conditioning". *World Oil*, 223(8), 89-91.
- Ostlund, J., (2005). "Supersonic flow separation with application to rocket engine nozzles". *Applied Mechanics Reviews*, 58(1), 143-176.
- Prast B., Lammers B., Betting M, (2006). "CFD for Supersonic Gas Processing", Fifth International Conference on CFD in the Process Industries, CSIRO, Melbourne, Australia, 13-15 December
- Qingfen, M., Dapeng, H., et al. (2009). "Performance of inner-core supersonic gas separation device with droplet enlargement method". *Chinese Journal of Chemical Engineering*, 17(6), 925-933.
- Schinkelshoek, P. and Epsom, H., Twister B.V. (2006). "Supersonic gas conditioning-low pressure drop TWISTER for NGL recovery". *Offshore Technology Conference*, Houston, Texas.
- Schinkelshoek, P., (2006). "Supersonic gas conditioning introduction of the low pressure drop twister". *GPA Annual Convention Proceedings*, 2, 830-853.





